UNIVERSITY OF Southampton

University of Southampton Research Repository
ePrints Soton

Copyright © and Moral Rights for this thesis are retained by the author and/or other copyright owners. A copy can be downloaded for personal non-commercial research or study, without prior permission or charge. This thesis cannot be reproduced or quoted extensively from without first obtaining permission in writing from the copyright holder/s. The content must not be changed in any way or sold commercially in any format or medium without the formal permission of the copyright holders.

When referring to this work, full bibliographic details including the author, title, awarding institution and date of the thesis must be given e.g.

AUTHOR (year of submission) "Full thesis title", University of Southampton, name of the University School or Department, PhD Thesis, pagination

http://eprints.soton.ac.uk

UNIVERSITY OF SOUTHAMPTON

FACULTY OF PHYSICAL SCIENCES AND ENGINEERING

Physics

Cryogenic Operation And Room Temperature Application Of An Optically-Pumped Surface-Emitting Semiconductor Laser

by

Oliver James Morris

Thesis for the degree of Doctor of Philosophy

June 2014

UNIVERSITY OF SOUTHAMPTON

ABSTRACT

FACULTY OF PHYSICAL SCIENCES AND ENGINEERING
Physics

Doctor of Philosophy

CRYOGENIC OPERATION AND ROOM TEMPERATURE APPLICATION OF AN OPTICALLY-PUMPED SURFACE-EMITTING SEMICONDUCTOR LASER

by Oliver James Morris

This thesis reports how the performance of a Vertical-External-Cavity Surface-Emitting Laser (VECSEL) can be significantly improved by cooling the active region to cryogenic temperatures. Also presented is the development of a room temperature, stable, high power, wavelength-tuneable, modelocked VECSEL and its subsequent implementation as a pump laser in a system designed to generate single photons.

The VECSEL is a type of semiconductor laser capable of producing high output power in near diffraction-limited beams. The semiconductor gain region is highly temperature sensitive and the output power of a VECSEL is limited by non-radiative Auger-recombination. Previous research has shown that by cooling the gain chip the gain per carrier is increased, the carrier density at the point of threshold lasing is reduced and the onset of Auger-recombination induced thermal rollover is delayed.

This thesis presents a VECSEL that uses a gain chip cooled to 83 K. The device exhibited a 53 % ± 10 % reduction in the incident pump power required to reach laser-threshold, a 4-fold increase in incident pump power tolerated prior to the onset of thermal rollover, and an increase in output power of more than an order of magnitude when its performance was compared to operation at 293 K. A modelocked VECSEL using a gain chip held at 143 K is also reported. Prior to this research the coldest temperature at which a VECSEL gain chip had been operated was 248 K. This work shows that cryogenic temperatures can significantly improve VECSEL performance and begins a new direction in VECSEL research.

The modelocked VECSEL has surpassed the performance of other types of modelocked semiconductor laser and is now approaching the performance of fibre and solid-state lasers. It has yet to be commercialised and so, to demonstrate that the modelocked VECSEL is now a mature, reliable technology, this thesis reports the development and implementation of a modelocked VECSEL as a pump laser in a single photon generation system. The system generates coincidental pairs of photons and, by detecting one photon in the pair, the presence of the companion will be *heralded*. The wavelength flexibility, excellent beam quality and high pulse repetition rate make the modelocked VECSEL ideal for both quantum state engineering and heralded single photon generation.

Contents

List of Figures

List of Tables

Declaration of Authorship

I, Oliver James Morris , declare that the thesis entitled *Cryogenic Operation And Room Temperature Application Of An Optically-Pumped Surface-Emitting Semiconductor Laser* and the work presented in the thesis are both my own, and have been generated by me as the result of my own original research. I confirm that:

- this work was done wholly or mainly while in candidature for a research degree at this University;
- where any part of this thesis has previously been submitted for a degree or any other qualification at this University or any other institution, this has been clearly stated;
- where I have consulted the published work of others, this is always clearly attributed;
- where I have quoted from the work of others, the source is always given. With the exception of such quotations, this thesis is entirely my own work;
- I have acknowledged all main sources of help;
- where the thesis is based on work done by myself jointly with others, I have made clear exactly what was done by others and what I have contributed myself;
- parts of this work have been previously published: see appendix B on page 111

Signed:.....

Date:.....

Acknowledgements

The work presented in this thesis is my own but it was only made possible by others...

Firstly I would like to thank my supervisor, Professor Anne Tropper, for giving me the opportunity to undertake this research. Her unwavering support and constant enthusiasm have been a continuous source of inspiration and she really does put the 'super' in supervisor. Thanks also to Dr Keith Wilcox and Dr Adrian Quarterman who between them have provided me with a wealth of experience: I could not have asked for more kind, patient, engaging and understanding post-docs.

I am indebted to the hard work and skill of the department's technical staff. In particular Damon Grimsey, Mark Scully, Mark Bampton, Paul Kinsey, Gareth Savage and Gary Taylor have together, not only given me the proverbial fish, but have also taught me how to catch the proverbial fish. No job was ever too small, too large or too complicated and this research could not have been completed without their valuable contributions.

One of the best things about scientific research is the opportunity to collaborate and I feel so lucky to have been able to collaborate with Dr Peter Mosley and Mr Jamie Francis-Jones at the University of Bath. The prospect of spending hours in a cramped, hot, pitch-black lab with a couple of strangers was quite daunting and my thanks go to Peter and Jamie for being such lovely, hard working and motivated people who made the experience much more pleasurable than it could have been.

I am also incredibly lucky that my friends are my colleagues. Without their help, support, kindness and good humour I honestly do not know if I would have been able to finish what I had started. John Spry, Robin Head, James Bateman, Andy Turnbull, Matt Proctor, Jo Carthy, Andrew Acreman, Paul Gow, Joe Spencer, Pearl John and the residents of 53 Shaftsbury Avenue are all invited to my birthday party.

To my friends outside of physics I don't expect you to ever read this document or understand what's in it but I promise you it's really good stuff and your encouragement and support was all worth while. To Bobbie Fordham thank you for all your love and assurance and I'm sorry I let everything get the better of me sometimes.

Lastly my thanks go to Mum, Dad, Toby, Granny, Grandad and Dair whose love, patience and support could always be relied upon.

Olly Morris - June 2014

Chapter 1

Introduction

The high output power of a semiconductor diode array is traditionally converted into a circular, low-divergence beam of good spatial coherence by using a diode-pumped, solid-state laser [1, 2]. Although this approach has demonstrated continuous wave (CW) output powers on the order of kilowatts [3, 4, 5], the dielectric gain medium of the solid-state laser results in a very restricted choice of emission wavelengths. In 1997 Kuznetsov et al demonstrated the first optically pumped Vertical-External-Cavity Surface-Emitting Laser (VECSEL) [6]. The VECSEL combines the high output power and excellent beam quality of the solid state laser, the diverse spectral coverage [7] and class-A laser dynamics [8] of the semiconductor diode laser and a compact, mechanically simple design that is relatively easy to mass produce [9]. Consequently the VECSEL has been rapidly developed into a succesful commercial laser technology [10, 11].

The VECSEL's semiconductor active region has allowed CW operation to be demonstrated at many wavelengths. The longest emission wavelengths, around 5 μm, are obtained using the PbTe material system [12]. The GaSb material system has been used to demonstrate up to 5 W of output power around 2 - 2.3 μm [13]. VECSELs emitting at 1.5 μm have been published using InP based materials [14, 15] and 1.3 - 1.2 μm emission can be obtained by using GaInNAs based materials [16] and highly strained InGaAs quantum wells [17]. The VECSELs presented in this work operate at a design wavelength of around 1000 nm and so use gain chips built from the InGaAs material system. The shortest direct VECSEL wavelengths are obtained using a GaInP-AlGaInPGaAs based gain chip and emit at 674 nm [18].

The external cavity design is realised through the incorporation of a free-standing spherical mirror that also acts as the cavity output coupler. It is this component that produces the excellent beam quality. The external cavity also facilitates the inclusion of intra-cavity elements. Wavelength tuning of a CW-VECSEL has been demonstrated through the use of an intra-cavity etalon and tuning ranges of 33 nm at 972 nm [19], 80 nm at 1980 nm [20] and 156 nm at 2000 nm [21] have been obtained. CW-VECSELs using intra-cavity second harmonic generation crystals have been demonstrated that emit around 338 nm [22] and 535 nm [23].

The semiconductor gain region is highly temperature sensitive relative to dielectric based solid-state lasers [24]. Poor thermal management of the gain chip can result in reduced gain per carrier, increased carrier density at the point of quantum well transparency and limited output power due to the advanced onset of Auger-recombination induced thermal rollover [25, 26]. All these effects can be mitigated by good thermal management of the gain chip.

There are two methods commonly used to passively manage the gain chip temperature. The 'heat spreader' approach extracts heat from the active region through the top of the chip. This is done by bonding a high thermal conductivity, transparent material to the top surface of the semiconductor structure [27, 28]. VECSELs using a diamond heat spreader have achieved output powers of 0.6 W at 1.32 μm [29], 10 W at 1.06 μm [30], 4 W at 1.05 μm [31] and 20 W at 588 nm [32]. A VECSEL using a silicon carbide heat spreader has achieved 0.5 W at 850 nm [33]. The second method, the 'thin chip' approach, replaces the substrate on which the gain structure is grown with a heat spreader. This technique is described in more detail in section 4.3.2. Using this method the highest output power for a single chip VECSEL has been obtained: 106 W at 1028 nm (multi-transverse mode operation) [34].

The gain chip can also be cooled actively. The first VECSEL, demonstrated by Kuznetsov et al in 1997, used a temperature controlled heat sink to thermally manage the gain chip: the VECSEL produced a 0.52 W CW-beam in a $TEM_{0,0}$ mode [6]. The highest reported VECSEL output power for fundamental transverse mode operation is 20 W using a heatsink cooled to 253 K [35]. The coldest temperature at which a VECSEL gain chip has previously been operated is 248 K [36]. This VECSEL used a liquid nitrogen cooled, thin gain chip and emitted a CW output power of 72 W (multi-transverse mode operation).

This thesis will report the operation of a CW-VECSEL using a gain chip cooled to 83 K. The work presented in this thesis therefore begins a completely new direction of research for the VECSEL community. The performance gains obtained by working at cryogenic temperatures will hopefully motivate further research in this area and the developement of gain structures designed specifically for cryogenic temperatures.

The VECSEL has been modelocked by incorporating quantum well [37], quantum dot [38] and graphene [39] saturable absorbers into the cavity. The first modelocked VECSEL was demonstrated in 2000 by Hoogland et al [40]. This VECSEL used a quantum well saturable absorber and emitted 21.6 mW average output power in 22 ps pulses at 1030 nm and at a repetition rate of 4 GHz.

To date the highest average output power achieved by a modelocked VECSEL is 5.1 W; 682 fs pulses at a repetition rate of 1.71 GHz [41]. The highest peak power demonstrated is 13.3 kW [42]. The shortest pulse duration is recorded to be 60 fs for pulse groups [43] and 106 fs for single pulses [44]: both results were at a laser wavelength around 1000 nm. Pulse durations of 384 fs at 2000 nm [45] and 5 ps at 675 nm [46] have also

been demonstrated. The highest recorded pulse repetition rate in fundamental operation is 92 GHz [44] and the lowest is 99.6 MHz [47]. A repetition rate of 175 GHz has been demonstrated using harmonic modelocking [48]. A modelocked VECSEL emitting high average power and sub-100 fs pulses has not yet been achieved.

The Modelocked Integrated External-Cavity Surface-Emitting Laser (MIXSEL) integrates the saturable absorber directly into the gain structure [49]. The highest reported average output power for a MIXSEL is 6.4 W [50]. A sub-picosecond pulse MIXSEL has also been reported [51].

Despite these results showing that the modelocked VECSEL is approaching the performance of fibre and solid-state lasers (and at a lower financial cost), the modelocked VECSEL is yet to be commercialised. Consequently there are few instances of the modelocked VECSEL being implemented as a source laser in some larger experiment or application.

This thesis will demonstrate that the modelocked VECSEL is now a mature technology that can be relied upon as a component in a larger experiment. The development of a modelocked VECSEL suitable for pumping a heralded single-photon system will be reported. The implementation of the VECSEL in the system and the experimental results achieved will also be presented. The wavelength flexibility, excellent beam quality and high pulse repetition rate make the modelocked VECSEL ideal for quantum state engineering when compared with traditionally used $\approx$ 80 MHz sources [52, 53, 54].

This chapter will continue by giving a brief overview of both the CW- and modelocked-VECSEL: CW-VECSEL operation will be presented in section 1.1 and modelocked VECSEL operation will be presented in section 1.2. The chapter will conclude with an overview of this thesis.

1.1 The CW-VECSEL

The VECSEL is not to be confused with the Vertical-Cavity Surface-Emitting Laser (VCSEL). The latter is an electrically pumped, surface emitting diode laser [55, 56]. Like the VECSEL, the VCSEL is able to emit a circular, transform limited beam however, due to the size of the emitting region (typically 10 μm), the output power of a VCSEL is typically constrained to tens of milliwatts [57, 58, 59]. Active regions larger than this result in a device that is prone to multimode operation and a uniform current density distributed across a large area is difficult to achieve. The VECSEL's external-cavity design allows the device to be optically pumped. Consequently a uniform carrier density can be achieved over a large area and the output power of the device can be

scaled by increasing the spot size of the pump laser [60]. Optical pumping also simplifies the device design as it eliminates both the need for electrical contacts and the use of doped semiconductors to transport carriers to the active regions. The use of undoped semiconductors has the added benefit of eliminating free carrier absorption and consequently the loss of the device is reduced.

The simplest CW-VECSEL comprises three components: the optical pump, the 'active mirror' gain structure and the output coupler. A schematic of this VECSEL is shown below in figure 1.1.

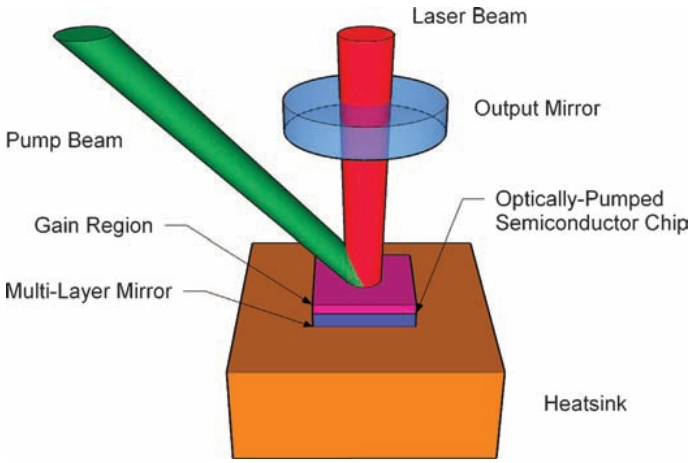

Figure 1.1: The constituent parts of an optically pumped CW-VECSEL. Figure reproduced from [7].

1.1.1 The Gain Chip

The VECSEL gain chip can be thought of as an 'active mirror': a structure that amplifies the light that it reflects. It is manufactured using either Molecular Beam Epitaxy (MBE) or Metalorganic Chemical Vapour Deposition (MOCVD).

The VECSELs presented in this thesis are at a design wavelength of around 1000 nm and therefore use gain chips built from direct band-gap group III-V semiconductors: semiconductors for which the minimum energy gap occurs where the valence band has a maximum and the conduction band has a minimum. A consequence of the direct band-gap is that the probability of a radiative transition occuring at the band-edge is high and this makes this type of material ideal for optical devices. Gallium-Arsenide (GaAs) is a III-V, direct band-gap alloy and an energy-band diagram of this material is presented on the following page in figure 1.2.

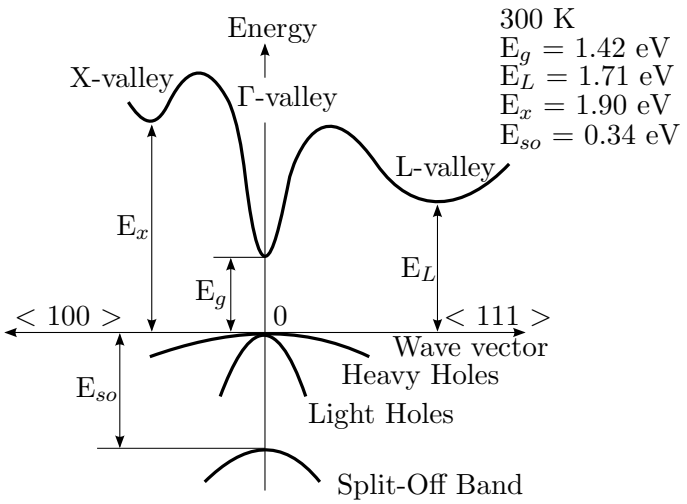

Figure 1.2: Band structure of Gallium Arsenide. The minimum energy gap occurs where the valence band has a maximum and the conduction band has a minimum. This makes Gallium Arsenide a direct band-gap semiconductor.

The band-gap of many III-V semiconductors can be tailored by adjusting the composition of the alloy. For example GaAs has a band-gap of 1.4 eV (887 nm), Indium-Arsenide (InAs) has a bandgap of 0.354 eV (3.5 μm) and the band-gap of $In_xGa_{1-x}As$ can be varied between these two values through adjusting the indium fraction. The band-gap and lattice spacing of several III-V semiconductors is shown below in figure 1.3.

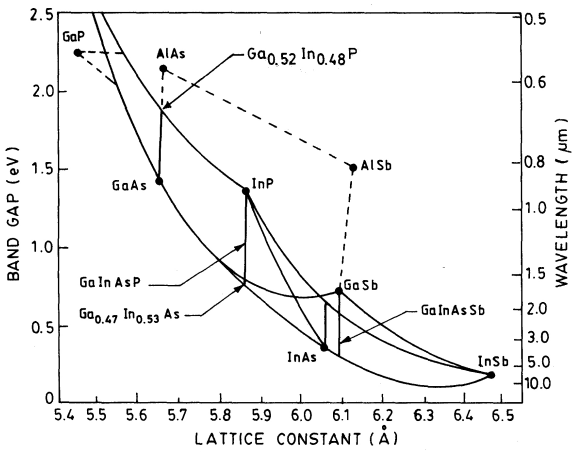

Figure 1.3: The band-gap and lattice constant of several common III-V semiconductors. Figure reproduced from [61].

The mirror used in the gain chip is a Distributed Bragg Reflector (DBR): a periodic structure that implements an alternating two-material, low / high refractive index profile in order to reflect the light [62]. Light passing from a low index material to a high index material is partially reflected at the interface and so, by using alternating quarter-wavelength thick layers of high and low index material, these reflections can be made

to add constructively. By varying the index contrast of the two materials the amount of light that is reflected at each interface can be controlled. By varying the number of high-low index repeats, the number of reflections occuring can be controlled. The DBR is incorporated into the gain structure as per the schematic shown below in figure 1.4.

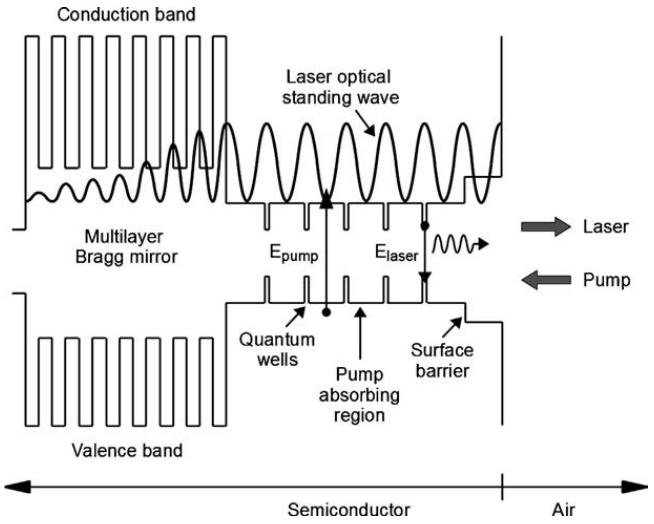

Figure 1.4: Schematic of a VECSEL gain chip showing the band structure of the gain chip and the laser E-field. Figure reproduced from [7].

The VECSELs reported in this thesis use a gain structure design that incorporates a 27.5 pair, AlAs/GaAs DBR. This provides a reflectivity of 99.9 % over a bandwidth of approximately 100 nm centred around 1000 nm. The position of the DBR reflectivity profile in wavelength is temperature dependent and will shift at a rate of 0.1 nm K^{-1} [8]: this is due to the temperature dependent refractive index of both GaAs and AlAs.

The active region of the gain chip is defined as the structure grown between the top of the DBR and the air interface. The region comprises some number of quantum wells, separated by GaAs barriers, and grown underneath an AlAs spacer layer and a GaAs capping layer. The capping layer protects the structure from oxidation. The active region is the part of the VECSEL that amplifies the light and a calculation of the gain, as a function of quantum well carrier density and temperature, for a single quantum well is given in section 2.2.1.

The VECSELs presented in this thesis use quantum wells constructed from the InGaAs semiconductor alloy. This produces an emission wavelength between 1000 and 1060 nm depending on the Indium concentration. The emission wavelength of the gain chip can also be altered post-growth by varying the temperature of the structure: an increase in thermal energy produces an increased interatomic spacing, a consequent decrease occurs in the potential as seen by the carriers, and this in turn reduces the size of the energy bandgap. In this work the gain structure emission wavelength was expected to exhibit a 0.3 nm K^{-1} temperature dependency [8].

The AlAs spacer layer controls the magnitude of the laser E-field at the front surface of the gain chip. A resonant gain chip design, characterised by a node in the laser E-field at the sample surface, is desirable for CW lasing as the E-field inside the structure will be as large as possible. Figure 1.5(a) below shows the calculated Group Delay Dispersion (GDD) and Longitudinal Confinement Factor (LCF), plotted against wavelength, for a gain chip designed to be resonant at 1035 nm. The longitudinal confinement factor is a measure of the overlap between the laser E-field and the quantum wells. It is defined as

$$\Gamma_z = \frac{\Sigma_n |E(z_n)|^2}{|E_0|^2} \tag{1.1}$$

where $|E(z_n)|^2$ are the squared moduli of the electric fields at the positions of the quantum wells and $|E_0|^2$ is the squared modulus of the electric field outside the sample. The group delay dispersion dictates how the constituent frequencies of a modelocked pulse will spread in phase relative to each other, and consequently how the duration of the pulse will broaden in time, as it propagates through a medium. A resonant microcavity design is unsuitable for modelocked operation as the dispersion profile and the gain filtering effect of the LCF conspire to produce a structure that is only able to operate over a small wavelength range.

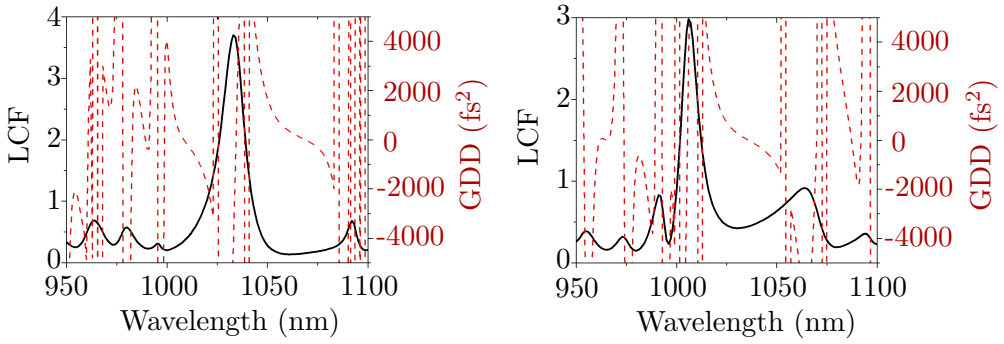

Figure 1.5: The longitudinal confinement factor (LCF - black line) and group delay dispersion (GDD - red line), calculated using the matrix formulation method given in [63], and plotted against wavelength for a resonant (a) and antiresonant (b) microcavity. The design wavelength is 1035 nm.

An antiresonant gain chip is characterised by an antinode in the laser E-field at the front surface of the gain chip. The GDD and LCF calculated for an ideal antiresonant structure operating at a design wavelength of 1035 nm are plotted against wavelength in figure 1.5(b). By situating the VECSEL emission in the LCF 'dip' the effect of the LCF filter on the laser mode is less pronounced. The curvature of the LCF is also opposite to the curvature of the gain profile at this wavelength. Consequently a broader bandwidth can be supported by the gain chip and therefore an antiresonant design is best suited to modelocked VECSEL operation.

The antiresonant design is also better suited to investigating the effect of temperature on VECSEL performance. A LCF exhibiting a flat response with respect to wavelength will ensure that, as the laser wavelength shifts with temperature, the mode will interact equally with the microcavity. Any temperature induced changes in VECSEL performance can therefore be attributed to the carrier dynamics in the gain chip and not the microcavity enhancement.

1.1.2 The Optical Pump

The VECSELs presented in this work are optically pumped with relatively cheap, and easily obtainable fibre-coupled diode lasers operating around 800 nm. The pump light is predominantly absorbed into the GaAs quantum well barriers and, because GaAs has a broad absorption profile, the wavelength of the pump light is not as critical in these lasers as it is in others. The spatial mode quality of the pump beam is also relaxed and this work assumes that the spatial profile of the optical pump is top-hat shaped.

1.1.3 The Output Coupler

In its simplest form the VECSEL's external cavity is created with a single free-standing spherical mirror. This mirror acts as the cavity output coupler and defines the transverse mode of the cavity. The shape of the mirror allows precise control of the laser mode and, by ensuring that the laser mode overlaps the pumped area perfectly, the VECSEL is able to emit in a $TEM_{0,0}$ mode with an M^2 value of approximately 1. The external cavity allows many different cavity geometries to be implemented and facilitates the inclusion of intracavity elements: for instance an etalon could be included to allow wavelength selection and stabilisation. The free-standing output coupler also allows the cavity length to be easily adjusted and consequently the pulse repetition rate of a modelocked VECSEL can be varied [64, 65].

1.1.4 The Principles Of VECSEL Operation

Lasing is achieved by first absorbing high energy pump photons into the GaAs quantum well barriers. The excited electrons and holes that are consequently generated then diffuse into the smaller bandgap quantum wells, become localised and create a population inversion. Spontaneous carrier recombination then occurs producing photons, with a lower energy, that are emitted from the chip. Those photons emitted in the direction of the output coupler will be reflected back onto the gain chip where they will stimulate the emission of more photons and lasing will occur. By placing the quantum wells at the antinodes of the laser E-field, maximum gain is ensured.

In addition to this radiative process there are two dominant non-radiative processes that affect laser operation: defect recombination and Auger recombination. In defect recombination a carrier can scatter off a defect in the crystal structure and thereby give up its energy to the lattice. The rate at which this process occurs will depend linearly on both the carrier density and the defect density. The impact of this mechanism can be minimised through high-quality growth. Auger recombination occurs when an electron transfers its energy by scattering off another carrier. Consequently this process requires three carriers to be present (an electron and a hole to recombine and a third carrier to conserve energy and momentum) and therefore scales with the cube of the carrier density and becomes a dominant source of device loss at high pump powers [8].

Auger recombination is also dependent on the carrier-carrier scattering time. This quantity decreases with temperature and therefore, because Auger recombination converts the energy of the electron into heat, as the temperature rises Auger recombination becomes increasingly probable. This in turn results in more heat being generated within the active region and the gain reduces. For large enough pump powers this feedback process will reduce the gain of the device to a level at which the VECSEL is unable to lase: this process is termed 'thermal rollover'. The onset of Auger-recombination induced thermal rollover can be delayed by cooling the gain chip. This allows higher carrier concentrations to be supported and consequently higher output powers can be obtained.

1.2 The Modelocked-VECSEL

Modelocking in VECSELs is traditionally achieved by incorporating a saturable absorber into the cavity as an additional, freestanding, cavity component [66, 67]. Termed the SESAM (Semiconductor Saturable Absorber Mirror) or SBR (Saturable Bragg Reflector) this component is a non-linear, passive element that comprises a saturable absorber grown epitaxially on to a DBR. Figure 1.6 shows how the SESAM can be incorporated into the VECSEL using a 'V-cavity' geometry.

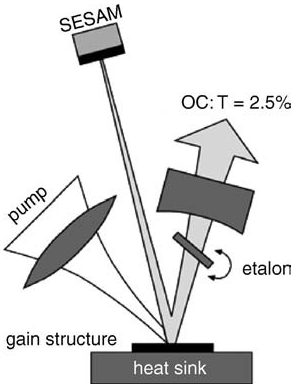

Figure 1.6: A cavity diagram for a modelocked VECSEL.

The SESAM modelocks the VECSEL by making it energetically favourable for the cavity to support a high intensity pulse of radiaton rather than low intensity CW radiation. A localised population of photons passing through the SESAM will promote electrons within the absorbing layer from the valence band into the conduction band. The consequent depletion in the number of absorbing carriers allows the remainder of the localised photon population to see the mirror behind the absorber. After the transmission of the high intensity pulse, the SESAM recovers due to electron-hole recombination and, with the SESAM now acting again as an absorber, the lasing operation is interrupted. By allowing this process to continually repeat, a train of pulses is emitted from the VECSEL.

In order to ensure that the cavity supports a single circulating pulse two experimental conditions must be met. Firstly due to the short upper-state lifetime of the active region ($\approx$ ns) a cavity length must be employed that results in a pulse repetition rate on the order of GHz. Secondly it is desirable to have the pulse saturate the gain as this closes the time-window of positive net gain. Diagrams of both the typical SESAM self-amplitude modulation and the typical cavity loss and gain for a modelocked VECSEL are given below in figure 1.7.

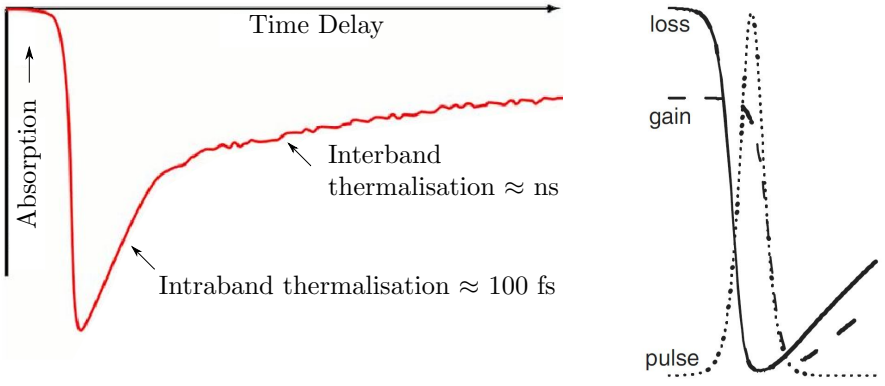

Figure 1.7: a) Typical self-amplitude modulation of a SESAM. b) Typical loss and gain in a modelocked VECSEL cavity. Figure amended from [37].

As the pulse passes through the saturable absorber the wings of the pulse experience more loss than the higher-intensity centre-region causing the duration of the circulating pulse to shorten. This mechanism is countered by the SESAM carrier recovery time, the finite gain bandwidth and, due to the dynamic saturation of the gain which causes a shift in the refractive index of the active region, self-phase modulation of the pulse.

Stable, near-transform-limited pulses can be achieved by balancing the negative, non-linear phase shift arising from the self-phase modulation with the correct amount of positive dispersion. Such pulses may be described as 'quasi-solitons' and the interested reader is directed to [68] for a more detailed analysis. An excellent review of passively modelocked VECSELs is provided by [37].

The modelocked-VECSELs presented in this work use quantum well saturable absorbers. Due to the gain structures also using quantum wells, it is expected that both the SESAMs and gain structures will have similar saturation fluences. In order to ensure stable modelocked operation, the saturable absorber is required to saturate more quickly than the gain. This is most easily achieved by implementing a cavity geometry with a tighter focus on the absorber than on the gain: for a given laser power this results in a higher pulse fluence on the absorber when compared to the gain and consequently the absorber will saturate first.

The saturable absorber can be integrated directly into the gain structure, as shown below in figure 1.8. This approach was first demonstrated in 2007 [49] and christened the Modelocked Integrated External-Cavity Surface-Emitting Laser (MIXSEL).

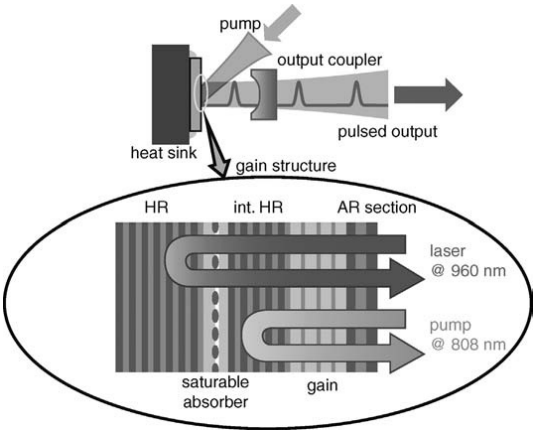

Figure 1.8: A schematic diagram of a MIXSEL. The pump and laser mode high-reflectors are labelled 'int. HR' and 'HR' respectively.

1.3 Thesis Overview

This chapter has given a brief overview of both the CW- and modelocked-VECSEL in addition to a summary of current VECSEL performance. Throughout the chapter particular care has been taken to highlight the known temperature dependencies of the VECSEL gain structure: the reflectivity profile of the DBR will shift with respect to wavelength at a rate of 0.1 nm K^{-1}, the emission wavelength of the gain chip is expected to exhibit a 0.3 nm K^{-1} shift and a reduction in temperature will also delay the onset of Auger-recombination induced thermal rollover allowing higher output powers to be obtained at colder temperatures.

As previously stated, the coldest published temperature at which a VECSEL gain chip has been operated is 248 K. The study of a VECSEL using a gain chip maintained at cryogenic temperatures is therefore both extremely interesting and a completely new

direction of research for the VECSEL community. Chapters 2 and 3 of this thesis will detail an investigation into cryogenic VECSEL operation.

Chapter 2 will present the preliminary work that was undertaken in order to establish if an investigation into cryogenic VECSEL operation would be feasible. The chapter begins by quantifying the benefits of operating a VECSEL gain chip at cryogenic temperatures: this is done through exploring two mathematical models. A method for remotely obtaining the active region temperature of a pumped VECSEL gain chip is then reported: this work is motivated by the need to verify the accuracy of the theoretical work and to allow the temperature of the VECSEL active region to be obtained when it is sealed inside a cryostat. Chapter 2 concludes with a preliminary attempt to demonstrate a cryogenically cooled VECSEL using a helium flow-cryostat.

Chapter 3 begins by presenting a liquid nitrogen, cold-finger cryostat, the design of which was informed by the preliminary experimentation reported in chapter 2. The application of the active region temperature sensing method to a cryogenically cooled gain chip is then reported. Investigations into the effect of temperature on both the incident pump power required to reach laser-threshold, and the amount of incident pump power tolerated prior to the onset of thermal rollover are then presented. The chapter concludes by reporting the demonstration of a modelocked VECSEL utilising a cryogenically cooled gain chip.

The introduction of this chapter also stated that the modelocked VECSEL is yet to be commercialised and that few implementations of this laser as a source laser in some larger application or experiment have been reported. One such proposed implementation is the use of a modelocked VECSEL as a pump source for generating coincidental photon pairs through four wave mixing in photonic crystal fibre. Chapter 4 reports on the development of a VECSEL source suitable to this application, the implementation of this source, and the experimental results achieved.

Chapter 5 concludes this thesis. In this chapter the work that has been undertaken is summarised and notable results are restated. The direction of future research is also discussed.

Chapter 2

A Cryogenic VECSEL Feasibility Study

2.1 Introduction

Liquid nitrogen cooling is used to achieve efficient high-power operation of ytterbium-doped solid-state lasers [69, 70, 71]: the gain of these quasi-3-level systems increases at low temperature, as does the thermal conductivity of the gain medium, while thermal lensing is reduced [72, 73, 74]. The VECSEL's semiconductor gain region is also highly temperature sensitive. By reducing the active region temperature improvements can therefore be made to the device performance: enhanced gain per carrier, reduced carrier density at the point of quantum well transparency and a delayed onset of Auger-recombination induced thermal rollover are all observed when the active region temperature is lowered [24].

This temperature dependent VECSEL performance is typically observed by cooling the VECSEL gain chip with a Peltier thermo-electric device. The cooling efficiency of these devices decreases strongly for temperatures below 288 K and therefore these observations have been restricted to temperatures greater than approximately 243 K. Chernikov et al have shown that by replacing the Peltier controlled heat-sink with a direct connection to a liquid nitrogen bath it is possible to increase the cooling efficiency of the system [36]. Using this method, and with the heat-sink temperature maintained at 248 K, they were able to dissipate more than 300 W of waste heat and demonstrate a processed VECSEL gain chip (similar to that described in section 4.3.2) operating at a maximum output power of 72 W.

The operation of a VECSEL gain chip at temperatures below 243 K presents many challenges. For example Chernikov et al report that any further temperature decrease below 248 K resulted in damage to their gain structure arising from severe mechanical stress due to differential thermal contraction [36]. If however these challenges can be overcome, the expected performance gains when coupled with the on-going development of micro cryogenic coolers [75] could make compact, cryogenically cooled VECSELs a very real and attractive prospect.

This chapter presents the work that was undertaken in order to determine whether a VECSEL could be operated using a cryogenically cooled gain chip, what improvements in laser performance might be expected by cooling the gain chip to cryogenic temperatures and if it is possible to remotely measure the temperature of the gain chip active region. Section 2.2 presents the quantified benefits of operating a VECSEL with a cryogenically cooled gain chip. A model based upon Fermi's Golden Rule is used to quantify the effect of quantum well temperature on the percentage gain per quantum well and the carrier density required to reach quantum well transparency. Section 2.2 also presents a steady-state thermal Finite Element Analysis (FEA) model that is used to calculate the effect of heat-sink temperature and pump power on the active region temperature. The development of a novel, remote method for obtaining the active region temperautre is described in section 2.3: this will ensure that the active region really is operating at cryogenic temperatures. The chapter concludes by reporting a preliminary experiment that was undertaken using a VECSEL gain chip in a helium flow-cryostat: this is done in section 2.4.

2.2 The Calculated Effect Of Temperature On The Performance Of A Cryogenically Cooled VECSEL

This section quantifies the qualitative statements that were made in the introduction regarding the enhanced VECSEL performance arising from cooling the active region of the gain chip. A mathematical model is presented in section 2.2.1 that allows the percentage gain per quantum well to be estimated as a function of both quantum well carrier density and operating temperature. This model is also used to estimate how both the quantum well carrier density and the operating temperature affect the quantum well transparency condition: this is done in subsection 2.2.2. The section concludes by presenting a Finite Element Analysis (FEA) model that calculates the temperature of the active region as a function of incident pump power and heat-sink temperature. The model is then investigated in order to study how the onset of thermal rollover can be delayed through reducing the heat-sink temperature.

2.2.1 Calculation Of The Percentage Gain Per Quantum Well

In this section a model is presented that calculates the percentage gain experienced by light passing through a single quantum well as a function of both quantum well carrier density and operating temperature. The model is based on an approach found in [76]. It assumes that the carriers do not interact with each other and that the conduction and valence bands can be approximated as parabolas near to the zero-momentum point.

By using Fermi's Golden Rule, the transition probability per second per unit volume for transitions occurring between a conduction and valence band can be calculated to be

$$R_\tau(E) = \frac{e^2\lambda_0}{2c\epsilon_0 m_0^2 n^2} N_p |M_T|^2 \rho_j(E), \tag{2.1}$$

where λ_0 is the transition wavelength, m_0 is the electron mass, n is the refractive index, N_p is the photon number density and $\rho_j(E)$ is the joint density of states. The value of the transition matrix element, $|M_T|^2$, is given in [76].

Momentum conservation rules restrict photon induced band-to-band transitions to only those transitions that are vertical with respect to k-space. Consequently the joint density of states is given by the density of states in either the conduction or valence band. By approximating both the conduction and valence bands as parabolas around the zero-momentum point, and taking into account the spin-degeneracy of the electron, the joint density of states, $\rho_j(E)$, is given by

$$\rho_j(E) = \frac{m_{\text{ef}}}{\pi\hbar^2 L} \sum_{i=1}^{N_l} \Theta(h\nu - (E_{c_i} - E_{v_i})) \tag{2.2}$$

where Θ is the Heaviside function, m_{ef} is the effective mass of the carriers in the band and L is the thickness of the quantum well. It is assumed that the laser transition only occurs between the $i = 1$ levels and so equation 2.2 can be simplified to

$$\rho_j = \frac{m_{\text{ef}}}{\pi\hbar^2 L} \quad \text{where} \quad \frac{1}{m_{\text{ef}}} = \frac{1}{m_{\text{effective electron mass}}} + \frac{1}{m_{\text{effective hole mass}}} \tag{2.3}$$

The transition rates from the conduction band to the valence band and from the valence band to the conduction band correspond to stimulated emission and absorption and are given by

$$R_{cv} = R_\tau f_c(1 - f_v), \tag{2.4}$$

and

$$R_{vc} = R_\tau f_v(1 - f_c), \tag{2.5}$$

where $f_{c,v}$ are the Fermi-Dirac functions that describe the filling of the states in each band. In the steady state the probability of a carrier in a band being found at energy E is given by the corresponding Fermi-Dirac distribution

$$f_{c,v}(E) = \frac{1}{1 + \mathrm{e}^{(E - E_{f_{c,v}})/k_b T}}. \tag{2.6}$$

The Fermi energy, $E_{f_{c,v}}$ is related to the band carrier density through the relation

$$N = \int_0^\infty f_{c,v}(E)\rho_{c,v}(E)dE \tag{2.7}$$

and, by substituting equations 2.3 and 2.6 into this expression, the integral can be solved to give expressions for the Fermi energy of the conduction and valence bands:

$$E_{f_c} = k_b T \ln\left(e^{\frac{N_c \pi \hbar^2 L}{m_e k_b T}} - 1\right) \tag{2.8}$$

and

$$E_{f_v} = k_b T \ln\left(e^{\frac{N_v \pi \hbar^2 L}{m_h k_b T}} - 1\right). \tag{2.9}$$

For a laser beam passing through a quantum well, the rate at which photons are added to the beam will be the difference between the rates of stimulated emission and absorption. An expression for the gain per unit length is therefore

$$g = \frac{n}{cN_p}(R_{cv} - R_{vc}) = \frac{e^2 \lambda_0 |M_T|^2}{2c^2 \epsilon_0 m_0^2 n}(f_c - f_v)\rho_j(E). \tag{2.10}$$

By substituting equations 2.8 and 2.9 into equation 2.6, and then substituting both this and equation 2.3 into equation 2.10, an expression can be obtained for the gain per unit length as a function of temperature and, by assuming that the quantum well is electrically neutral so that $N_c = N_v$, carrier density:

$$g = \frac{e^2 \lambda_0 |M_T|^2}{2c^2 \epsilon_0 m_0^2 n} \times \left(\frac{1}{1 + \mathrm{e}^{(E - k_b T \ln\left(e^{\frac{N_c \pi \hbar^2 L}{m_e k_b T}} - 1\right))/k_b T}} - \frac{1}{1 + \mathrm{e}^{(E - k_b T \ln\left(e^{\frac{N_v \pi \hbar^2 L}{m_h k_b T}} - 1\right))/k_b T}} \right) \frac{m_{\mathrm{ef}}}{2\pi \hbar^2 L}. \tag{2.11}$$

Inspection of equation 2.10 shows that the gain experienced by the passing laser beam will become positive when $f_c > f_v$. This is equivalent to requiring that $E_{f_c} > E_{f_v}$. A plot of the percentage gain as a function of carrier density and temperature for an 8 nm wide $In_{0.2}Ga_{0.8}As$ quantum well emitting at 1020 nm is given on the following page in figure 2.1. The plot was built by the author using a Python script.

The assumption that the emission wavelength of the quantum well does not change with temperature is incorrect however the inclusion of the 0.3 nm K^{-1} shift [8] would also demand the inclusion of other many-body effects and this level of complexity is deemed beyond the scope of this work.

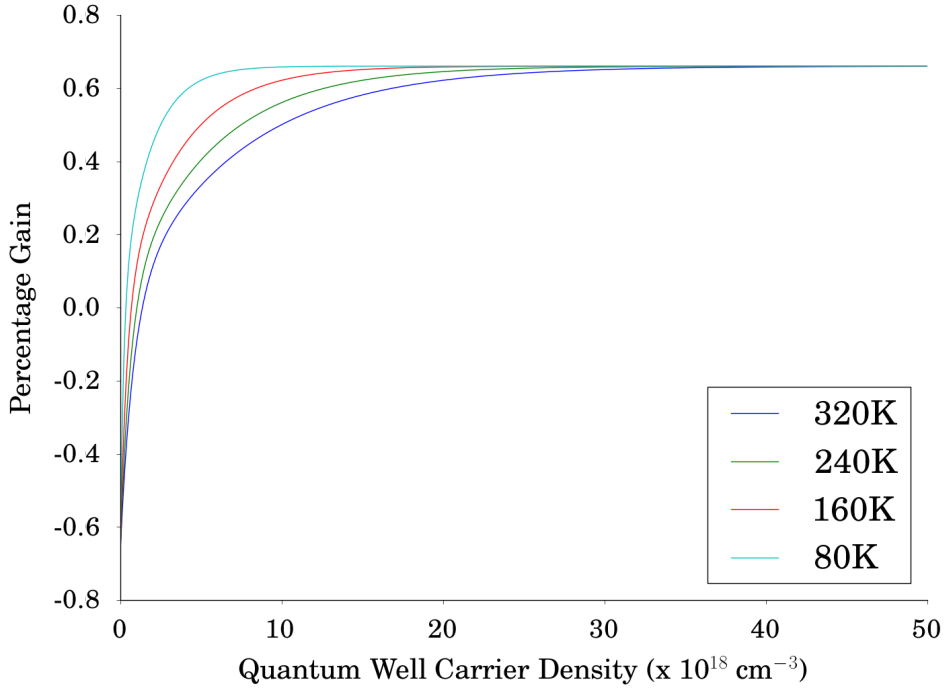

Figure 2.1: Gain per quantum well as a function of carrier density and temperature for a single 8 nm thick, $In_{0.2}Ga_{0.8}As$ quantum well emitting at 1020 nm.

Figure 2.1 shows that by reducing the temperature of the quantum well from 320 to 80 K an increase in the amount of gain available at low carrier densities should be observed. The largest increase in gain occuring at a fixed carrier density is from 0.344 % to 0.628 % at a carrier density of 0.5 x 10^{18} cm^{-3}. A VECSEL using a cryogenically cooled gain chip is therefore expected to exhibit a greater slope efficiency when compared to a VECSEL operating at room temperature.

2.2.2 Calculation Of The Point Of Quantum Well Transparency

Quantum well transparency is defined as the point at which the quantum well stops being an absorber and becomes an emitter. This point is characterised by the percentage gain equalling 0 and so, by setting equation 2.11 equal to 0, quantum well transparency can be evaluated as a function of both quantum well temperature and carrier density. This is done in figure 2.2 for an 8 nm wide $In_{0.2}Ga_{0.8}As$ quantum well emitting at 1020 nm.

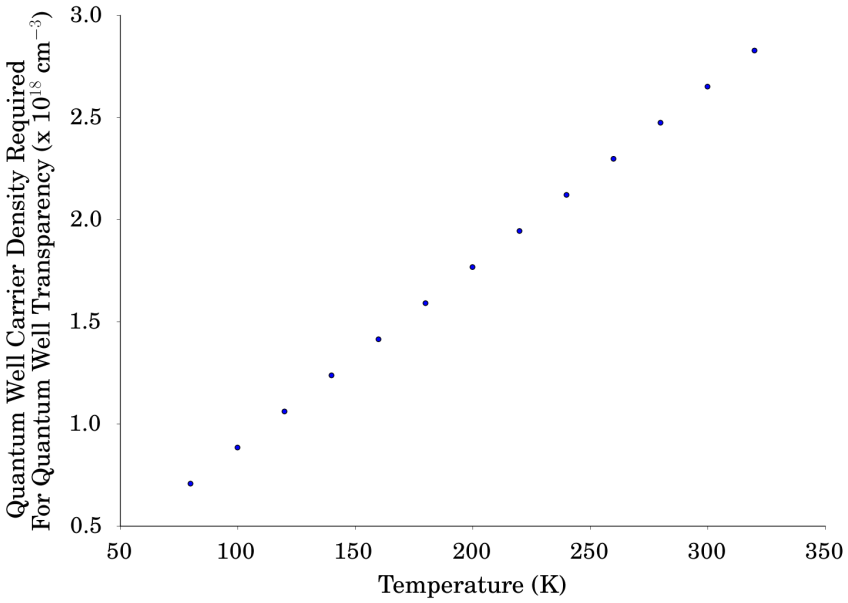

Figure 2.2: The calculated relationship between the carrier density and temperature required to operate a single, 8nm thick, $In_{0.2}Ga_{0.8}As$ quantum well at the point of transparency.

From figure 2.2 it can be seen that by reducing the temperature of the VECSEL active region from 300 to 80 K, a 70 % reduction in the carrier density required for quantum well transparency is predicted. A VECSEL using a cryogenically cooled gain chip is therefore expected to have a lower lasing threshold than its room temperature counterpart.

2.2.3 Calculation Of The Maximum Tolerated Incident Pump Power

For large carrier densities in the active region, non-radiative Auger recombination will become the dominant recombination channel and consequently the VECSEL will exhibit thermal rollover. This will occur for an active region temperature around 400 K [26]. In order to investigate the relationship between this critical temperature and both the incident optical pump power and the heat sink temperature, a study was undertaken using the Finite Element Analysis (FEA) software COMSOL.

This work was inspired by that undertaken by Alan Kemp at the University of Strathclyde [77] and the two models share a number of physical assumptions: a simplified chip geometry is assumed with a much reduced number of structural boundaries; structural degradation due to thermally induced mechanical stress is ignored; the active region heat-load is generated by the quantum defect alone and heating through non-radiative recombination is neglected.

Whilst this last assumption appears to contradict the aims of the model it was included for three reasons. Firstly Auger-recombination only becomes critical around thermal rollover and therefore any heating that occurs prior to this point of operation can be well approximated by quantum defect heating. Secondly by using this assumption Kemp was able to obtain reasonable agreement between the calculated and measured temperature rise [77]. Finally in order to properly incorporate a non-radiative recombination heat load, a full microscopic model of the gain chip would be required [24] and this level of complexity was deemed beyond the scope of this work.

In this study the gain chip was modelled as a four-domain multilayer stack: the GaAs substrate, the DBR, the gain region and a 'top' layer. This geometric simplification was made in order to reduce both the processing power required and the time taken to complete a simulation. The material properties of each domain were however modified in order to reflect this omitted structural detail. For example the GaAs/AlAs pairs within the DBR were ignored as structural boundaries but the value used for the DBR thermal conductivity contained the contribution from both the GaAs and AlAs.

The complete FEA model consisted of this simplified gain chip placed on top of (and therefore in thermal contact with) an 'infinitely' large copper heat sink. The simulation exhibited a symmetry around the centre of the gain chip and so only a vertical slice through the strucutre from the centre to the radius needed to be considered. This made it possible to initialise the simulation as a '2-D Axial Symmetry General Heat Transfer' model and further reduce the computational requirements. A schematic of the investigated structure is given below in figure 2.3.

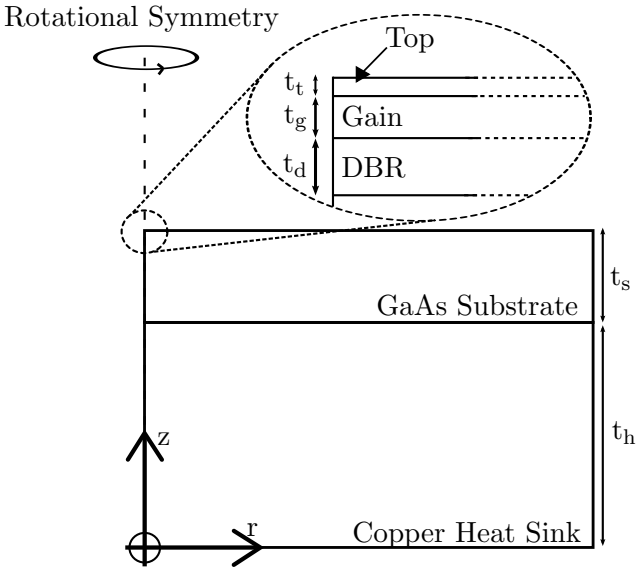

Figure 2.3: A schematic of the structure investigated using FEA. The structure comprises a four-domain stack (the GaAs substrate, the DBR, the active region and a 'top' layer) placed in thermal contact with an 'infinite' copper heat sink. A 808 nm, top-hat distributed source focussed to a 60 μm spot was assumed.

The pump beam was modelled as a $\lambda_{pump} = 808$ nm, top-hat profile source focussed to an $\omega_p = 60$ μm spot. The model assumed that absorption of the pump only occured in the gain region and DBR of the structure. The active region absorption coefficient, α_g, was approximated by using the absorption coefficient of GaAs, evaluated for 1.53 eV. A temperature dependence was incorporated into α_g using data given in [78]. Pump absorption in the DBR was assumed to only occur in the GaAs layers due to the absorption coeffecient of AlAs being small for photon energies < 2.17 eV. A typical DBR, with a design wavelength of 1000 nm, will have a 46 % GaAs, 54 % AlAs composition and consequently the absorption coefficient used in this model for the DBR region, α_d, equalled $0.46\times\alpha_g$.

As previously stated the heat loading fraction in the active region, η_g, is calculated from the quantum defect. Due to the quantum well emission exhibiting a 0.3 nm K^{-1} thermal dependency the quantum defect is itself temperature dependent. The value used for η_g is therefore calculated using equation 2.12 below. The heat loading fraction in the DBR, η_d, was assumed to be 1.

$$\eta_g = 1 - \frac{\lambda_{pump}}{\lambda_{design} - 0.3(T_{room} - T)} \tag{2.12}$$

The total heat load in the active region and DBR for $r \leq \omega_p$ is therefore given by

$$Q_{active\ region}(r,z) = \frac{\eta_g \eta_T P_p}{\pi \omega_p^2} e^{-\alpha_g(z_{0_g} - z)} \tag{2.13a}$$

$$Q_{DBR}(r,z) = \frac{\eta_d \eta_T P_p}{\pi \omega_p^2} e^{-\alpha_d(z_{0_d} - z)} e^{-\alpha_g t_g} \tag{2.13b}$$

and

$$Q_{gain}(r,z) = Q_{DBR}(r,z) = 0 \qquad \text{for} \qquad r > \omega_p. \tag{2.14}$$

The quantities and values used in equation 2.13 are summarised in the table on the following page.

By neglecting the non-radiative recombination contribution to the active region heat-load it was accepted, despite Kemp's observations, that the calculated active region temperature would diverge from the measured active region temperature for increasing pump power. It was also expected that the model would over-estimate the amount of pump power tolerated by the gain chip prior to thermal rollover occuring.

The scale of this disparity was unknown when constructing the model and, whilst it was hoped that this model would be able to provide a rough estimate of the active region temperature, a quantitative measurement of the model's accuracy was also needed. In order to provide this measurement a novel method for determining the absolute temperature of the active region was developed. This work is presented in section 2.3.

Symbol	Quantity	Value
t_t	Thickness of 'top' domain	0.44 μm
t_g	Thickness of 4.5λ/2 gain region	0.6 μm
t_g	Thickness of 27.5 pair GaAs/AlAs DBR	4.56 μm
t_s	Thickness of GaAs substrate	500 μm
z_{0_g}	Z-coordinate of the interface between the window layer and the active region	0 μm
z_{0_d}	Z-coordinate of the interface between the active region and the DBR	-0.6 μm
λ_{design}	Design wavelength of gain chip	1020 nm
η_T	Fresnel transmission of pump beam at 20° from normal incidence	0.7
λ_{pump}	Wavelength of pump beam	808 nm
P_p	Pump Power	
ω_p	$1/e^2$ radius of the pump	60 μm
T_{room}	Room temperature	293 K
α_g	Effective pump absorption in the active region	[78]
α_d	Effective pump absorption in the DBR	0.46×α_g
η_g	Fraction of pump power absorbed and converted into heat in the active region	Eq 2.12
η_d	Fraction of pump power absorbed and converted into heat in the DBR	1

Table 2.1: The quantities used to model the heat load in the gain chip

The boundary conditions of the simulation are that the bottom edge of the copper heat sink is set to the investigated heat-sink temperature, symmetric boundary conditions are used at the axis of rotation and thermal insulation is assumed elsewhere as cooling through convection is negligible.

An example simulation is shown on the following page in figure 2.4. The largest sub-domain depicted is the GaAs substrate and the sub-domain above is the DBR: on this scale the active region and top layers are too small to be seen. The figure shows the temperature distribution within the gain chip when the substrate is placed in thermal contact with a copper heat-sink held at 300 K and the active region is pumped with 2.5 W of 808 nm light focussed into a 60 μm radius spot.

Under these conditions the maximum active region temperature is calculated to be approximately 418 K. The maximum active region temperature is the value of interest as the laser mode does not have to roll-over with spatial uniformity. Instead, for example, the laser could first roll-over at the centre of the mode followed by the radius at a later point in time.

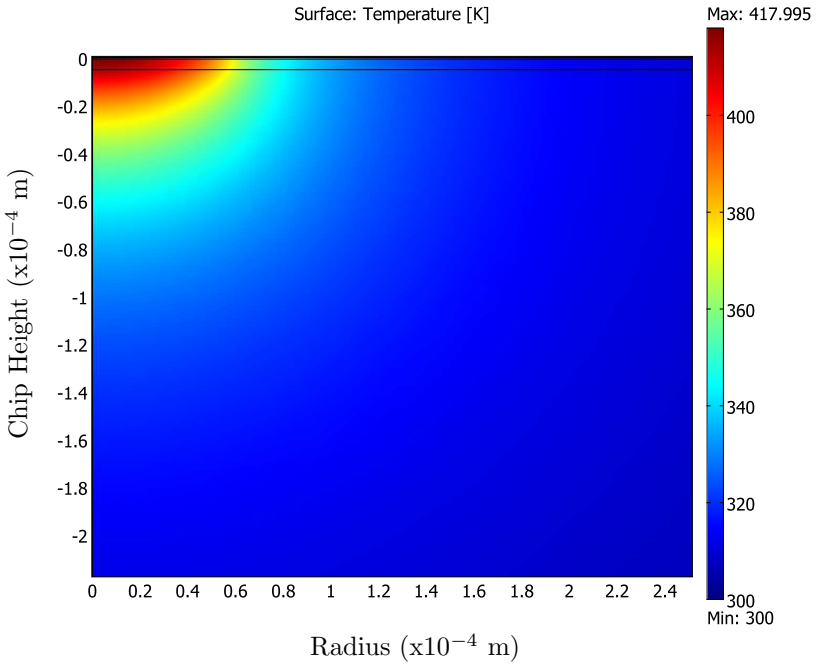

Figure 2.4: The calculated heat map of a VECSEL gain chip pumped with 2.5 W of 808 nm light focussed into a 60 μm radius spot. For a heat-sink temperature of 300 K, the active region temperature is calculated to be 418 K.

The model was investigated for heat-sink temperatures between 300 and 80 K and for incident pump powers between 0 and 8 W. Figure 2.5 below plots the calculated temperature rise in the active region against pump power and for varying heat-sink temperatures.

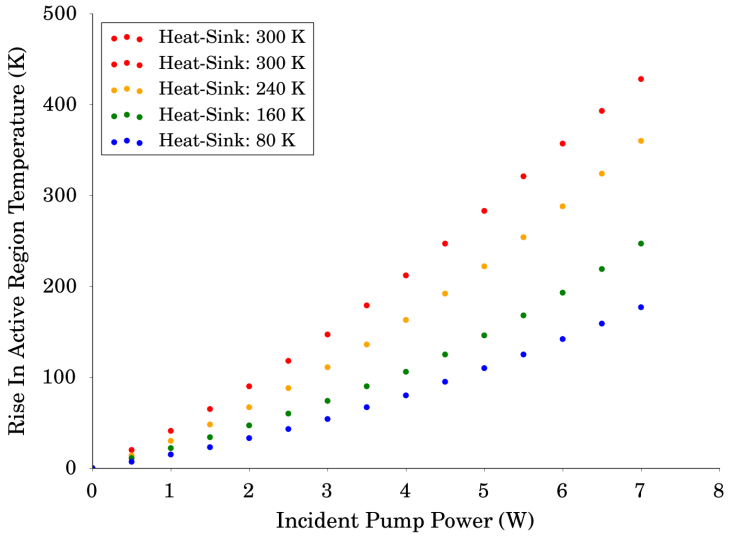

Figure 2.5: The calculated rise in active region temperature plotted against pump power for different heat-sink temperatures: a pump wavelength of 808 nm and a pump-spot radius of 60 μm is assumed.

A plot of the active region temperature against heat-sink temperature is given below in figure 2.6. This plot assumes a constant pump power of 2.5 W focussed into a 60 μm radius spot and at a wavelength 808 nm. Under these pump conditions, the model predicts that a 220 K reduction in heat-sink temperature will cause a 295 K reduction in the temperature of the active region.

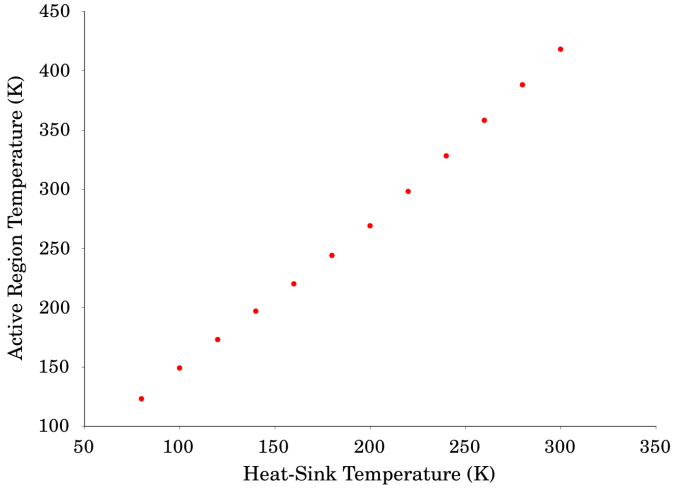

Figure 2.6: The calculated active region temperature plotted against heat sink temperature assuming a constant pump power of 2.5 W focussed into a 60 μm radius spot and at a wavelength 808 nm. An active region temperature reduction of 295 K is calculated for a 220 K reduction in the heat sink temperature.

The calculated active region temperature is plotted against pump power for different heat-sink temperatures in figure 2.7. Again a pump wavelength of 808 nm and a pump-spot radius of 60 μm is assumed.

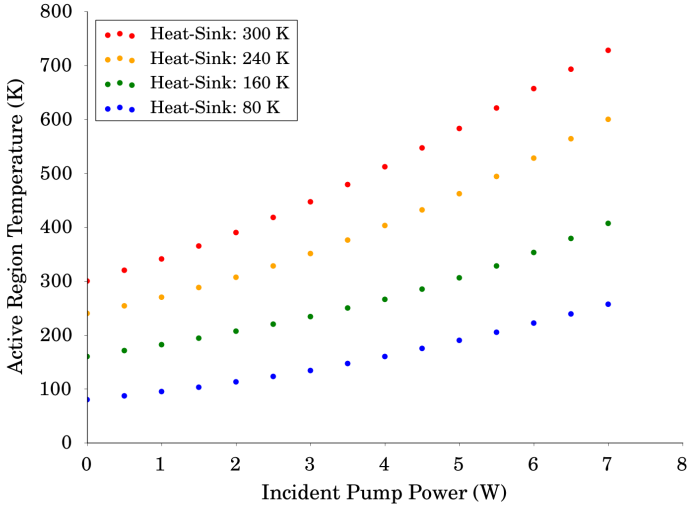

Figure 2.7: The calculated active region temperature plotted against pump power for different heat-sink temperatures: a pump wavelength of 808 nm and a pump-spot radius of 60 μm is assumed.

Previous research conducted by the group has shown that a VECSEL gain chip, with an active region length of $4.5\lambda/2$ at $\lambda = 1020$ nm, placed in contact with a copper heat-sink maintained at 300 K will exhibit thermal rollover at approximately 1.5 W of pump power. The FEA model predicts, as shown in figure 2.7, that these operating conditions correspond to an active region temperature of approximately 365 K.

The model goes on to predict that if this gain chip were instead placed in thermal contact with a heat-sink maintained at 80 K, and the effects of thermally-induced mechanical stress were neglected, the gain chip would be able to tolerate approximately 9.25 W of pump power prior to the onset of thermal rollover. Consequently this model predicts that much higher output powers should be obtained for a VECSEL utilising a cryogenically cooled gain chip.

2.3 The 'DBR-Shift Method': A Method For Remotely Determining The Active Region Temperature

In this section a so far unpublished method for remotely obtaining the active region temperature of a pumped VECSEL gain chip is reported. The motivation for this work was twofold: to provide experimental verification of the FEA model detailed in the previous section and to allow the local temperature of the VECSEL gain chip to be determined whilst it operated within a cryostat. Initially a number of techniques were proposed: this method was chosen as it was cost-effective and quick to implement.

2.3.1 The Method

The solution proposed uses a fixed wavelength probe beam, approximately coincident in wavelength with the long-wavelength edge of the DBR stop-band, to illuminate an unpumped gain chip. The incident and reflected intensity of the probe beam are monitored and a reflectivity ratio is calculated. The heat-sink temperature is then varied and this shifts the DBR reflectivity spectrum in wavelength by 0.1 nm K^{-1}. A corresponding change will occur in the reflectivity ratio of the fixed wavelength probe beam. By assuming that the unpumped gain chip is in thermal equilibrium with the heat-sink, a calibration curve of reflectivity at a fixed wavelength and against absolute temperature is obtained. Additional heat loads can then be placed on the chip (optically pumping the chip for example) and, by monitoring the change in the probe beam reflectivity and cross-referencing this with the calibration curve, an absolute active region temperature can be deduced. A schematic of the experiment is given below on the following page in figure 2.8.

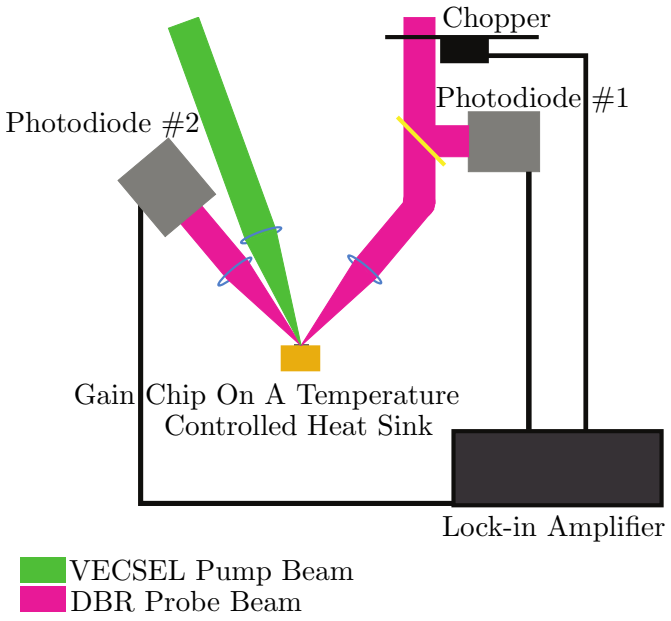

Figure 2.8: Schematic of the 'DBR Shift Method' apparatus. See text for details.

The gain chip investigated had a 27.5 pair AlAs/GaAs DBR typical of that used in 1 μm VECSELs. A spectrophotometer was used to obtain the reflectivity profile of the DBR at 300 K and at an angle of approximately 20° from the surface normal. This angle was chosen because this is the angle at which the probe beam, constrained by the experimental geometry, would be illuminating the sample surface. The long-wavelength half of this reflectivity curve is given below in figure 2.9.

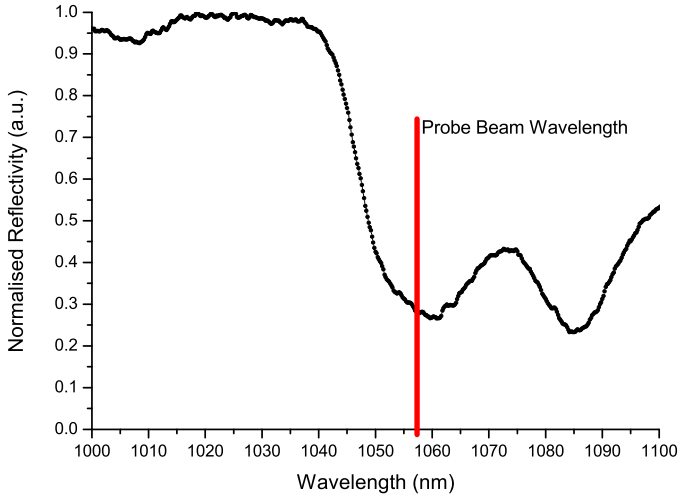

Figure 2.9: The reflectivity profile of a gain chip using a 27.5 pair AlAs/GaAs DBR, held at 300 K, and illuminated at an angle of approximately 20° from the surface normal. From this measurement a probe beam wavelength of 1058 nm was chosen in order to amplify changes in the probe beam reflectivity.

From this plot a probe beam wavelength of 1058 nm was chosen as the steep edge of the DBR stop-band would make clear any changes in the reflectivity of the probe beam. In addition to the wavelength criteria the probe beam also needed to have an excellent beam quality in order to evenly illuminate the pumped area on the gain chip, be readily available and cost relatively little to implement. An obvious choice was to use a secondary VECSEL.

The probe VECSEL was constructed using a gain chip with a design wavelength of 1060 nm. The cavity used a 100 mm, linear cavity geometry and a 0.3 % output coupler to produce a diffraction-limited, $TEM_{0,0}$, CW beam. The probe wavelength was set at 1058 nm by actively cooling the gain chip to 0 °C. This temperature control also stabilised the wavelength to within 0.5 nm of 1058 nm for the duration of the experiment. An optical spectrum of the probe beam, taken using an Ocean Optics HR4000 spectrometer, is shown below in figure 2.10.

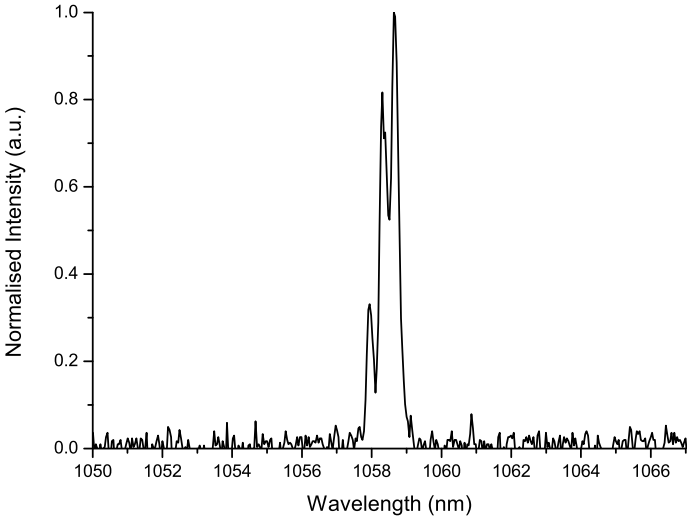

Figure 2.10: Optical spectrum of the VECSEL probe beam taken using an Ocean Optics HR4000 spectrometer.

The probe beam was collimated and then guided through a set of neutral density filters: this attenuated the power of the probe beam to <1 mW and ensured that it would not contribute to the heat load placed on the investigated gain chip.

The probe beam was directed through a chopper and a 50:50 pellicle beam splitter: one beam was focussed directly onto an InGaAs photodiode whilst the other was used to illuminate the front surface of the gain chip with a 60 μm radius spot. The reflected probe beam was then used to illuminate a second InGaAs photodiode. The signal from the two photodiodes and the reference signal from the chopper were fed to a lock-in amplifier (Bentham 223), the output of which was displayed on an oscilloscope. The two photodiodes were not calibrated relative to each other as the absolute reflectivity was not being investigated.

The gain chip was placed in thermal contact with a temperature controlled copper heat-sink. A Labview programme was written to interface the pump-diode, the oscilloscope and an optical spectrum analyser used to monitor the probe beam. For a given heat-sink temperature the Labview programme recorded the optical spectrum of the probe beam (to ensure that the reflectivities were in fact comparable) and 10 readings from each oscilloscope channel. It then increased the power of the pump-diode by a specified amount and the process was repeated. After the specified range of pump-diode powers had been investigated the temperature of the heat-sink was altered manually and the computer programme restarted. The data collection procedure was undertaken for heat-sink temperatures between 258 and 373 K in steps of 5 K and for pump powers between 0 and 1 W in steps of approximately 45 mW.

2.3.2 A Proof Of Concept Implementation

For a given pump power and heat sink temperature, each photodiode level was read 10 times. The average level and standard deviation for each photodiode was then calculated. A reflectivity ratio was subsequently obtained by dividing the average signal from the photodiode measuring the reflected intensity, by the average signal from the photodiode measuring the incident intensity. A confidence interval, shown as error bars in figures 2.11 and 2.12, was calculated for this reflectivity ratio by using the mean photodiode levels and the calculated standard deviations, as per equation 2.15.

$$\text{Confidence Interval} = \sqrt{\left(\frac{\sigma_{\text{photodiode 1}}}{\text{Mean}_{\text{Photodiode 1}}}\right)^2 + \left(\frac{\sigma_{\text{photodiode 2}}}{\text{Mean}_{\text{Photodiode 2}}}\right)^2}. \tag{2.15}$$

A plot of reflectivity against heat-sink temperature for no applied pump power is shown on the following page in figure 2.11. Under these conditions thermal equilibrium could be assumed between the active region of the gain chip and the copper heat-sink. The reflectivity values in figure 2.11 therefore correspond directly to an absolute and known active region temperature. The data points are connected by straight lines and this data-set can be thought of as a rudimentary calibration curve.

Figure 2.12 displays both the data-set obtained for no applied pump power and the reflectivities measured for an applied pump power of 1 W. Each 'pumped chip' data point can then be mapped onto the 'un-pumped' data-set (most likely onto one of the interpolated straight lines) through an x-axis translation. Doing this yields an increase in temperature from a known baseline temperature and consequently the new absolute temperature of the active region can be obtained.

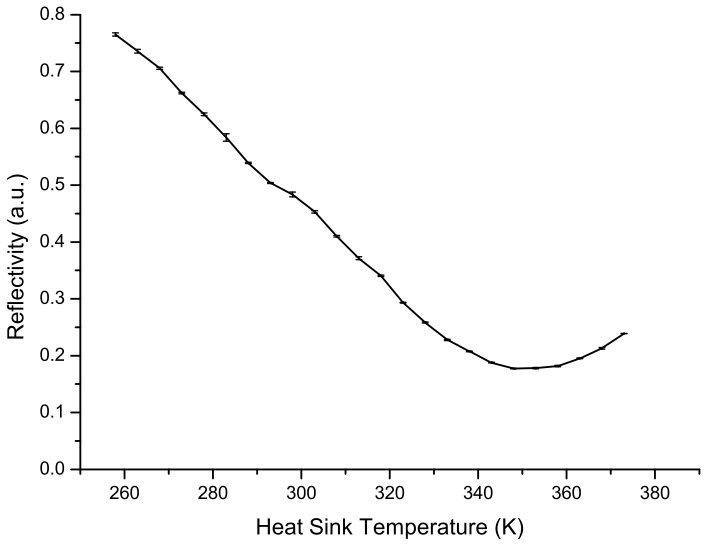

Figure 2.11: The measured reflectivity plotted against heat-sink temperature for no applied pump power. Under these conditions thermal equilibrium could be assumed between the active region of the gain chip and the copper heat-sink.

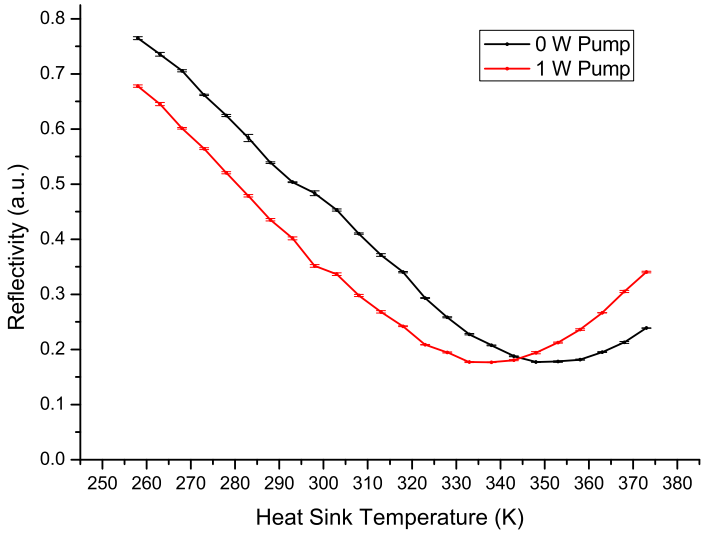

Figure 2.12: The measured reflectivity plotted against heat-sink temperature for 0 and 1 W of pump power. By mapping the '1 W' data points onto the 0 W calibration curve, an increase in temperature from a known baseline is obtained.

By applying this extraction method to all recorded reflectivities it is possible to generate a plot of absolute active region temperature against incident pump power for varying heat-sink temperature. This plot is shown on the following page in figure 2.13. The active region temperature is determined to within an accuracy of ± 2 K for this data set.

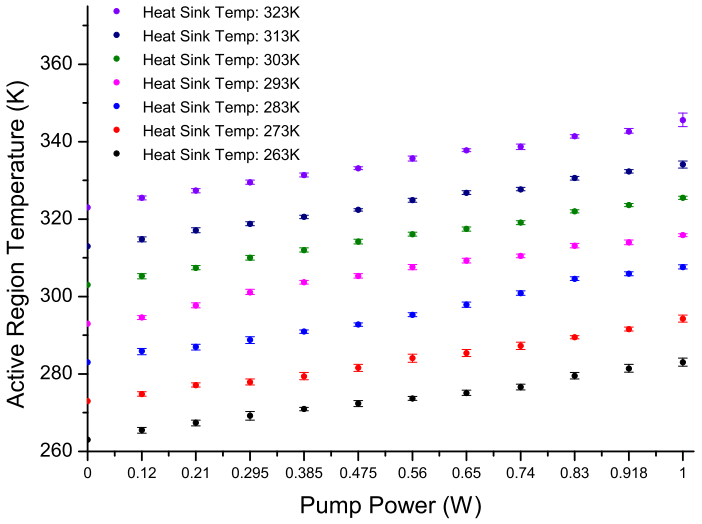

Figure 2.13: The extracted absolute active region temperature plotted against incident pump power for varying heat-sink temperatures.

By comparing the data presented in figure 2.13 with the results obtained using the FEA model in section 2.2.3 it is possible to test the accuracy of the FEA model. An example comparison, shown below in figure 2.14, plots both the calculated and experimentally measured active region temperature against the incident pump power for a heat sink temperature of 303 K.

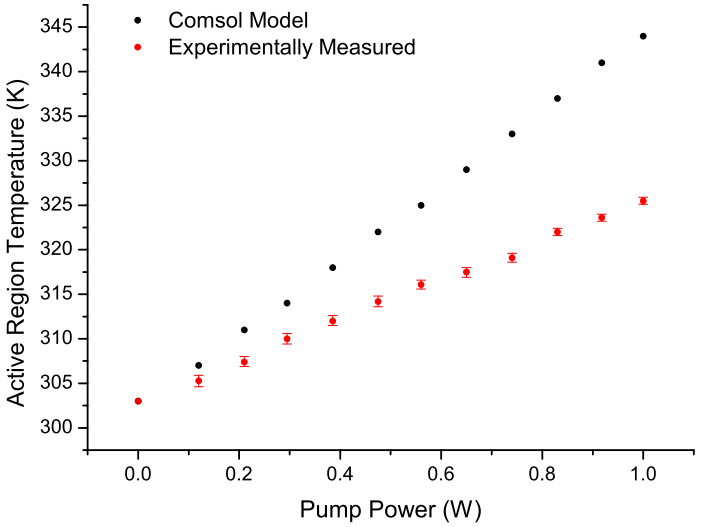

Figure 2.14: A comparison of the experimentally measured and FEA calculated active region temperature for a heat-sink temperature of 303 K and an incident pump power of up to 1 W. The FEA model is accurate to within 18 K (6 %) of the experimentally measured value.

Figure 2.14 shows that over the incident pump power range investigated, the active region temperature calculated by the FEA model is accurate to within 18 K (6 %) of the experimentally measured value.

2.4 A Helium Flow-Cryostat Cooled Gain Chip

This section reports the design and operation of a VECSEL using a gain chip cooled to 20 K. This work was undertaken using a helium flow-cryostat. The primary objective of this work was to determine whether it was possible to operate a VECSEL gain chip at cryogenic temperatures. A secondary objective was to determine whether any of the expected improvements in VECSEL performance could be realised.

2.4.1 Laser Design And Room Temperature Performance

An anti-resonant, 6 quantum well gain chip was bonded, using silver paint, to the cold-finger of a helium flow-cryostat. The gain chip chip was pumped with a 100-micron-core fibre-coupled 808 nm diode-laser focussed to a 100 μm diameter spot. With the cryostat open, a CW-VECSEL using a linear cavity geometry was aligned. Optimal output efficiency at room temperature was achieved by using a 0.7 % output coupler.

In this configuration lasing was achieved for 150 mW of incident pump power and a maximum lasing output power of 620 mW was achieved for an incident pump power of 1.86 W. This corresponds to a slope efficiency of 35 %. Assuming internal cavity losses of $\approx$ 0.5 % a total loss of $\approx$ 1.2 % is expected. The total gain of the laser is therefore $\approx$ 1.2 % and this corresponds to a gain of $\approx$ 0.2 % per quantum well. By using the gain model set out in section 2.2.1, this gain per quantum well corresponds to an estimated carrier density of 2.26×10^{18} cm^{-3}.

2.4.2 Cryogenic Laser Performance

The gain chip was bonded to the cold-finger of the helium flow-cryostat using silver paint. The size of the vacuum space meant that it was not possible to house the entire VECSEL inside the cryostat and so, when the gain chip was sealed into the cryostat, the cryostat window acted as an intracavity element. A schematic of the experiment is given in figure 2.15 (the extent of the vacuum space is not shown and, in order to simplify the schematic, the experiment is drawn having been rotated by 90 °).

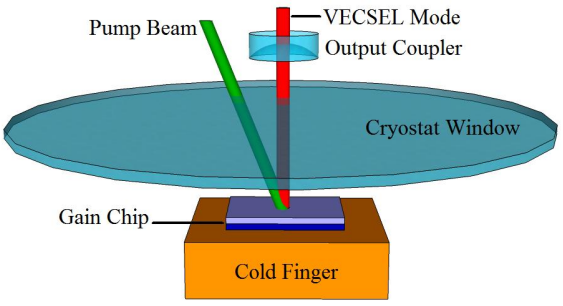

Figure 2.15: Schematic of the experimental setup used for the preliminary cryogenic VECSEL. It can be seen that the helium flow-cryostat window will act as an unwanted intracavity element

It was not possible to operate the gain chip at room temperature with the cryostat window in place: the loss imposed by the cryostat window was too great. Due to time constraints it was not possible to accurately characterise the loss of the window however literature suggests that a loss of ≈ 8 % is expected.

The cryostat was then evacuated and the gain chip was both cooled to 20 K and illuminated with up to 3.1 W of pump light. At this temperature the gain chip was able to lase. A 0.7 % and a 1.5 % transmission output coupler were used to construct two linear cavities. The output power as a function of pump power for these two lasers is shown in figure 2.16. Also included in this figure is the performance of the VECSEL operating at 293 K and without the cryostat window in place. The input pump power has been scaled accordingly in order to allow a comparison to be made between the three lasers.

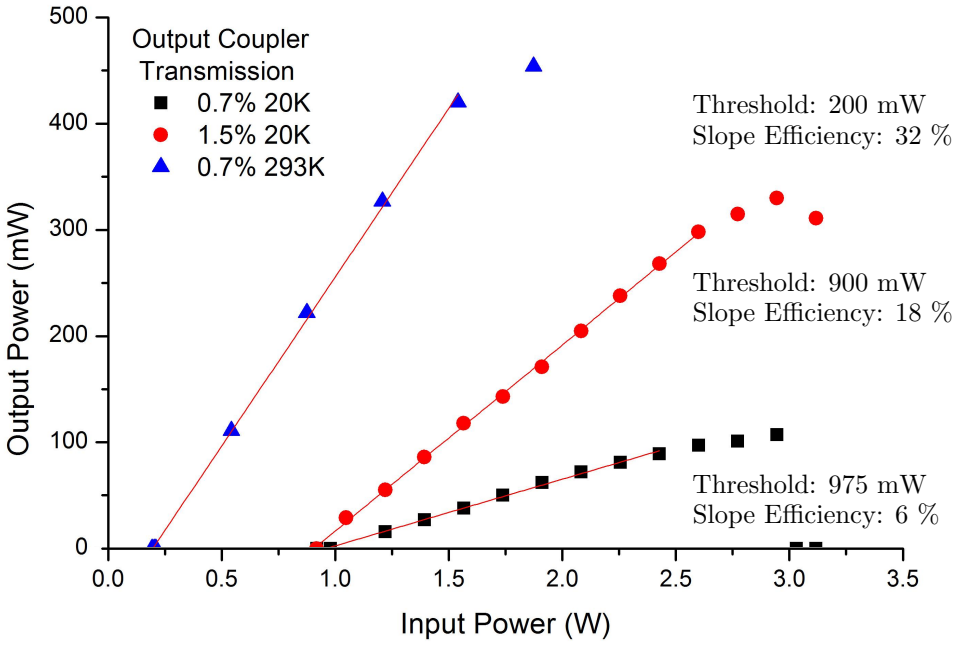

Figure 2.16: Output power as a function of input power and output coupling for an antiresonant, 6 quantum well VECSEL gain chip held by silver paint to a coldinger and operated at both 293 K with the cryostat open and at 20 K with the cryostat sealed. The input pump power has been adjusted accordingly to allow the comparison.

The gain model set out in section 2.2.1 calculates that the carrier density at lasing threshold should undergo a 90 % reduction when the gain chip is cooled from 293 to 20 K and a 0.7 % output coupler is used. With the gain chip sealed into the cryostat the measured lasing threshold, as shown in figure 2.16, was observed to increase 4.5-fold over this temperature range. This discrepancy is likely to be due to the cryostat window acting as a high-loss intracavity element and obscuring the expected reduction in threshold pump power.

By comparing the output power of the VECSELs operating at 20 K to that of the VECSEL operating in the open cryostat and at room temperature, a reduction in the output power for cold operation is observed. The VECSEL using the 0.7 % output coupler exhibited an 80 % decrease in maximum output power when cooled from 293 to 20 K. Again this contradicts the expected performance and is attributed to the cryostat window acting as a high-loss, intracavity element.

Figure 2.16 also shows that the VECSEL using the 0.7 % output coupler tolerated approximately 1.7-times more pump power prior to the onset of thermal rollover when operated at 20 K and compared with 293 K operation. This suggests that higher carrier densities can be supported at cryogenic temperatures and correspondingly that there should be an increase in the maximum gain available. This statement is supported by the observation that, when sealed in the cryostat and held at 293 K, the VECSEL was unable to lase due to the intracavity loss imposed on the device by the cryostat window. At 20 K the VECSEL was able to overcome this loss and lase.

Because the cryostat window was not characterised properly it is impossible to experimentally quantify the exact increase in gain occuring for 20 K operation. The gain model does however predict that a VECSEL gain chip operated at 20 K and at a quantum well carrier density equivalent to the 293 K laser threshold carrier density should exhibit 0.66 % gain per quantum well: this corresponds to a 3.3-fold increase in the gain per quantum well when compared with 293 K operation.

This preliminary work showed that it was indeed possible to operate a VECSEL gain chip at cryogenic temperatures. The expected improvements in VECSEL performance were hinted at however, due to the cryostat window acting as a high-loss, intracaviy element, it was not possible to fully realise this improved behaviour. A suitable method to eradicate this loss will be discussed in the next chapter.

2.5 Chapter Conclusions

This chapter began with a theoretical investigation into the performance of a VECSEL utilising a cryogenically cooled gain chip. Section 2.2 used a model based upon Fermi's Golden Rule to quantify the effect of quantum well temperature on the percentage gain per quantum well and the carrier density required to reach quantum well transparency. A steady-state thermal FEA model was also used to calculate the effect of heat-sink temperature and pump power on the active region temperature. These models calculated that by cooling a gain chip from 300 to 80 K a 140 % increase in percentage gain for a carrier density of 0.5 x 10^{18} cm^{-3}, a 70 % reduction in the carrier density required for quantum well transparency and a 6.2-fold increase in pump power prior to the onset of thermal rollover should be observed. Consequently a VECSEL utilising a cryogenically cooled gain chip should exhibit a reduced laser threshold, an increased slope efficiency

and a tolerance to greater pump powers when compared to a VECSEL operating at room temperature. To quantify this performance further would require a full microscopic model and this is deemed beyond the scope of this work.

Section 2.3 reported a method for remotely obtaining the active region temperature of a pumped VECSEL gain chip. This work was motivated by the need to verify the accuracy of the FEA model and to allow the active region temperature of the VECSEL gain chip to be obtained when sealed inside a cryostat. The method used a fixed wavelength VECSEL to probe the reflectivity profile of a DBR as it shifted in wavelength due to changes in the temperature of the gain chip. The method was tested at room temperature and for an incident pump power of up to 1 W. Under these conditions the temperature of the active region was determined to within an accuracy of ± 2 K. By comparing the results of this method to the the FEA model it was possible to show that, for these operating conditions, the FEA model is accurate to within 18 K (6 %) of the experimentally measured value. The method is applied to a cryogenically cooled VECSEL chip in the following chapter.

Section 2.4 reported a preliminary attempt to demonstrate a cryogenically cooled VECSEL. A helium flow-cryostat was used to cool a VECSEL gain chip from 293 to 20 K. This resulted in a 4.5-fold increase in the pump power required to achieve lasing, an 80 % decrease in maximum output power and a delayed onset of thermal rollover. This last observation suggests that a higher carrier density, and therefore an increase in the maximum gain available, can be supported at cryogenic temperatures. This statement is further supported by observing that the VECSEL was unable to lase at 293 K due to the loss imposed by the intracavity cryostat window however, when cooled 20 K, the VECSEL overcame this additional loss and lased. The observed increase in gain per quantum well at cryogenic temperatures is predicted by the model set out in section 2.2.1 however the observed increase in threshold carrier density for 20 K operation is not. This disagreement is most likely to be due to the performance of this cryogenically cooled VECSEL being dominated by the cryostat window acting as an unwanted, high-loss, intracavity element. A suitable method to eradicate this loss will be discussed in the next chapter.

Chapter 3

Cryogenic VECSEL Operation

3.1 Introduction

In the previous chapter a VECSEL was reported that used a cryogenically cooled gain chip. This VECSEL exhibited a 4.5-fold increase in the pump power required to achieve lasing and an 80 % decrease in maximum output power when cooled with a helium flow-cryostat from 293 to 20 K. The gain chip was able to tolerate higher pump powers prior to the onset of thermal rollover when operated at 20 K confirming that at cryogenic temperatures the maximum gain available increases. This statement is supported by observing that, when sealed in the cryostat and held at 293 K, the VECSEL was unable to lase however, when cooled 20 K, the VECSEL was able to overcome the loss imposed by the cryostat window and lase. The loss imposed on the device by the intracavity cryostat window dominated the laser performance and meant that a complete characterisation of VECSEL performance was not possible.

To better investigate the performance of a VECSEL using a cryogenically cooled gain chip, a cryostat with a vacuum space large enough to encompass the entire VECSEL cavity was commissioned. This cryostat was built in the mechanical workshop by Mr Damon Grimsey and I am indebted to his skill and hard work. This cryostat implemented a liquid-nitrogen cold-finger design allowing the gain chip to be cooled to 80 K.

In this chapter the effect of cryogenic temperatures on a VECSEL gain chip is studied using the liquid-nitrogen, cold-finger cryostat. The chapter begins by discussing the design of the cryostat: this is done in section 3.2. Section 3.3 then reports how the 'DBR-shift method' presented in section 2.3 was used to confirm both that the cryostat operated as expected and to further study the accuracy of the FEA model presented in section 2.2.1. The chapter concludes by reporting the development and characterisation of two VECSELs: a CW-VECSEL is reported in section 3.4 and a modelocked VECSEL is reported in section 3.5. Both these VECSELs use a liquid nitrogen cooled gain chip.

3.2 The Liquid Nitrogen, Cold-Finger Cryostat

In this section the design of the liquid nitrogen cold-finger cryostat is discussed. The design process was a collaborative effort between the author and Mr Damon Grimsey: a member of the mechanical workshop technical staff. The design process was informed by both the preliminary work that was reported in section 2.4 and some unreported work that was conducted using a small liquid nitrogen, cold-finger cryostat.

3.2.1 The Vacuum Chamber

To avoid the output window of the cryostat acting as an unwanted intracavity element the liquid nitrogen cold-finger cryostat was designed to have a vacuum space large enough to house the entire VECSEL cavity. In order to ensure that every conceivable cavity geometry could be employed the vacuum space was designed to measure 60 mm in height, 320 mm in width and 420 mm in length. In order to maximise the strength and stability of the vacuum, the chamber was designed with a minimal number of structural joins. The tray and walls of the chamber comprised one continuous piece of aluminium and the lid of the chamber was constructed from a second piece. A sacrificial base plate sat in the tray to which the optical mounts were fixed. An air-tight seal between the lid and the base of the chamber was ensured by placing a rubber seal, coated in Dow Corning High Vacuum Grease, between the two and bolting the lid to the base using an incremental, cross-wise method.

Six windows were incorporated into the side-walls of the vacuum chamber. Four of these windows were uncoated and were predominantly used to monitor the items placed into the chamber. The other two windows were anti-reflection coated and used to couple the optical pump into, and the VECSEL beam out of, the vacuum chamber. A seventh window was incorporated into the lid of the vacuum chamber in order to monitor the alignment of the VECSEL components.

The chamber was evacuated using a Pfeiffer turbo-molecular pump. The lid of the cryostat was drilled to accept a T-section of 1/2" pipe to which both the turbo-molecular pump and a vacuum gauge were connected. The vacuum gauge was used to monitor the strength of the vacuum within the chamber. A butterfly valve was installed between the T-section and the vacuum pump in order to isolate the vacuum chamber. The size of the vacuum chamber meant that it was not possible to bake it out prior to use and therefore, when isolated from the pump, a static vacuum of only 1 x 10^{-3} mB was achieved due to components out-gassing. Consequently the work reported in this chapter was conducted without disconnecting the vacuum pump and the chamber was held under a dynamic vacuum of approximately 8.5 x 10^{-6} mB.

A schematic of the vacuum chamber (without the lid) is shown in figure 3.1.

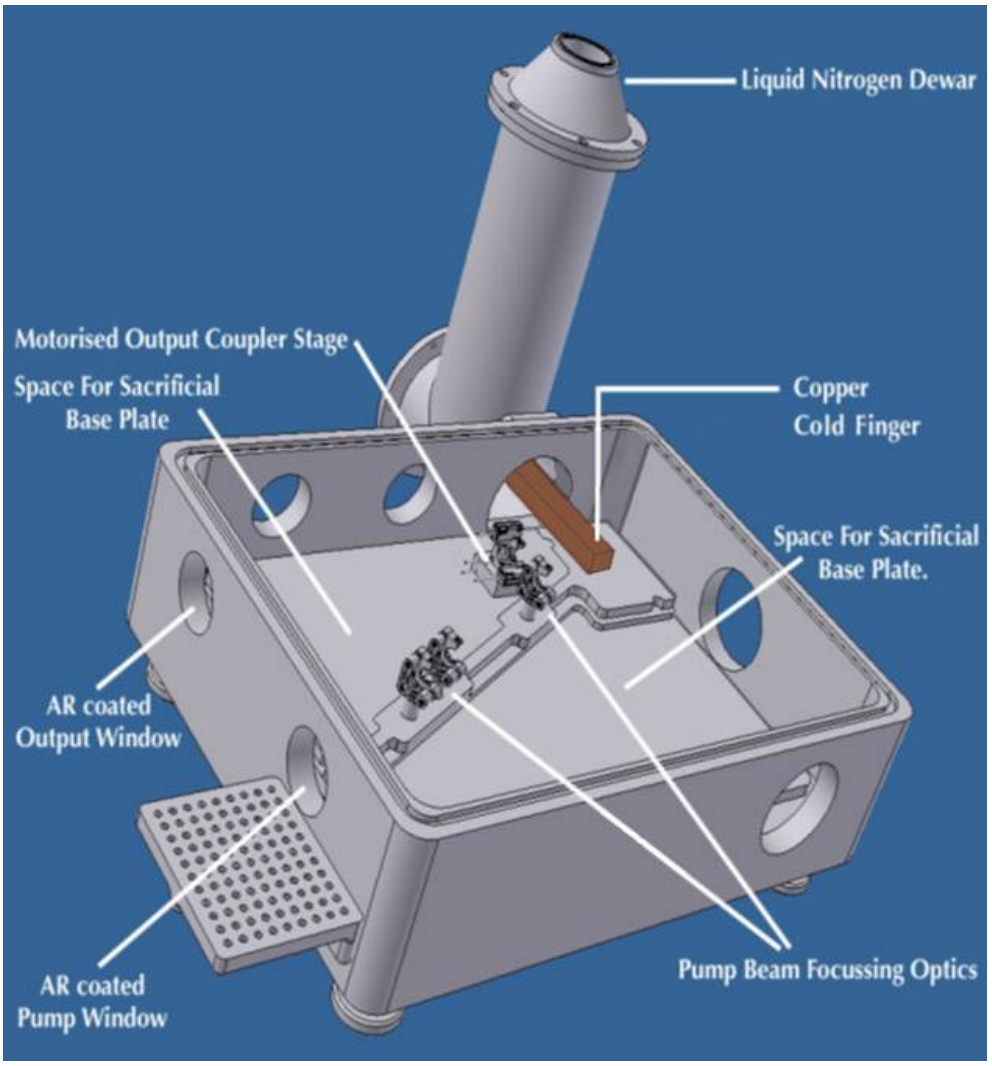

Figure 3.1: The liquid nitrogen, cold-finger cryostat. The cryostat is shown without lid and feedthrough ports. The vacuum chamber is large enough to house an entire VECSEL cavity

3.2.2 The Cold-Finger

A 1 L liquid nitrogen dewar was incorporated on to the side of the vacuum chamber. A copper cold-finger was bolted to the base of this dewar and a hole was machined into the side wall of the cryostat in order to allow the cold-finger to extend into the vacuum space. A thin layer of cryogenic, high vacuum Apiezon N-Grease was used between the dewar and finger in order to maximise thermal conductivity. The cold finger was supplied in two geometries to allow both linear and folded cavities to be built (figure 3.2). Both fingers were designed to maintain a maximum local temperature of 125 K whilst directly absorbing 30 W of pump power in a 60 μm radius spot. The CAD designs were verified through FEA and an example simulation is shown on the following page in figure 3.3.

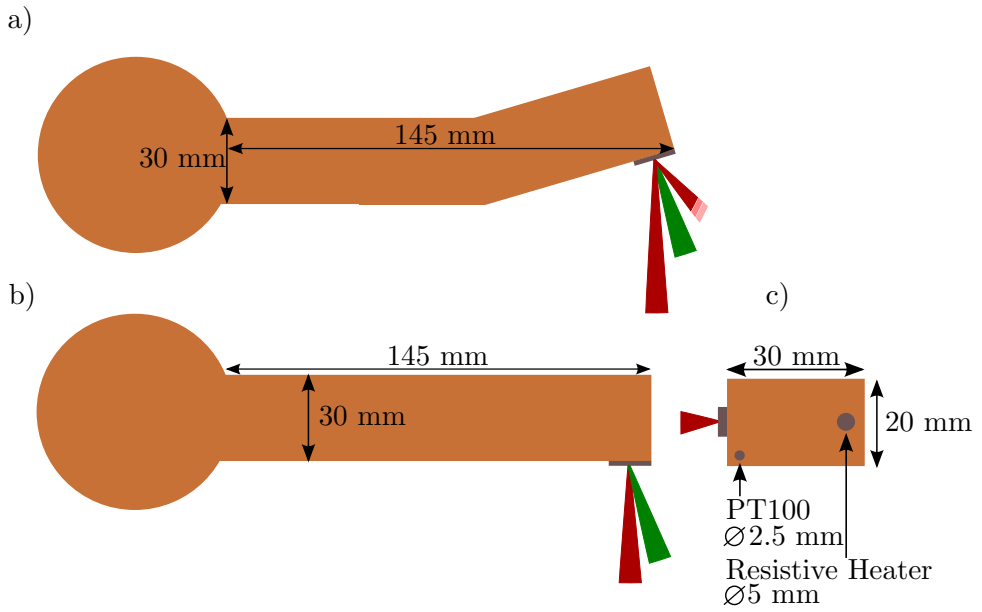

Figure 3.2: Schematic showing the two copper cold fingers used in the cryostat: a) Top view of the angled design that facilitates the construction of multiple mirror cavities b) Top view of the straight design used for linear cavity VECSELs c) End view of the cold finger showing the PT100 temperature sensor and resistive heat. The centre of the PT100 is located 3mm in from and 1 mm above the bottom left corner. The centre of the heater is located 5 mm in from and 7.5 mm above the right bottom right corner.

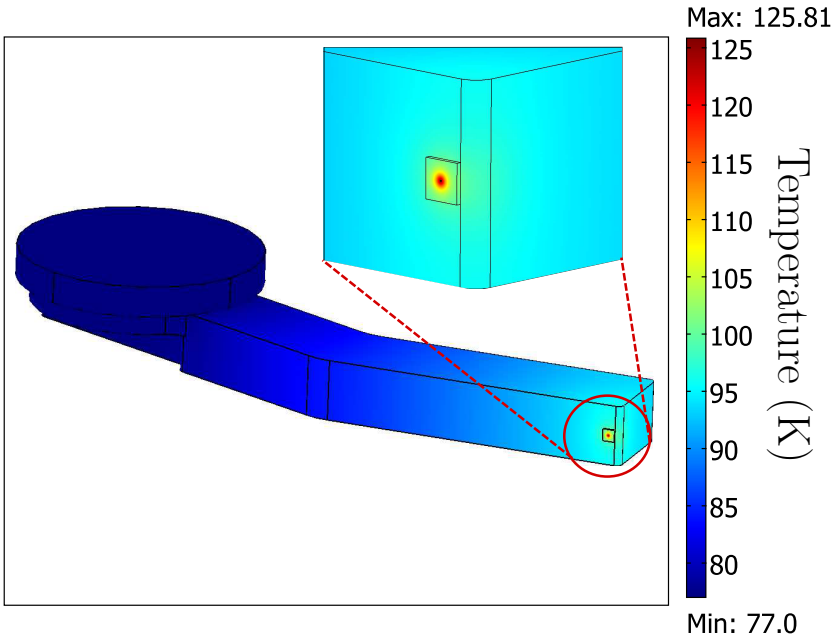

Figure 3.3: An FEA simulation of one of the two copper cold-fingers. In this model the cold-finger is pumped with 30 W of 808 nm light focussed into a 60 μm radius spot. Under these conditions the local chip temperature is calculated to be 125 K.

The cold-finger could be cooled to 80 K by filling the dewar with liquid nitrogen. To operate the cold-finger at temperatures between 293 and 80 K, the liquid nitrogen cooling was balanced with a resistive heater buried into the end of the cold-finger. This heater formed part of a feedback loop that also comprised a Eurotherm 3216 temperature controller and a PT-100 sensor. The sensing and control signals were passed out of and into the vacuum chamber using a vacuum compatible electrical feed-through manufactured by Positronic Industries (France).

A COMSOL model was used to investigate the difference between the surface temperature of the cold-finger directly behind the gain chip and the temperature of the cold-finger at the position of the PT-100. In this model a gain chip, represented as a slab of GaAs with a thickness of 500 μm, was placed in thermal contact with the cold-finger as shown in figure 3.3. The optical pump was modelled as a uniform circular heat-source, with a radius of 60 μm, at the centre of the top-surface of the GaAs slab. It was not possible to include finer detail than this as the range of mesh sizes required by the FEA model would become too great and the calculation would fail.

The model was first investigated for 0 W incident pump power and for heat source values at the position of the resistive heater corresponding to a temperature at the PT-100 sensor of between 77 and 257 K in steps of 40 K. At 77 K thermal equilibrium was assumed between all locations on the cold-finger as in order to reach this temperature the resistive heater would be switched off. This investigation was then repeated for pump powers up to 6 W in 1 W steps. The data obtained from this investigation is plotted in figure 3.4

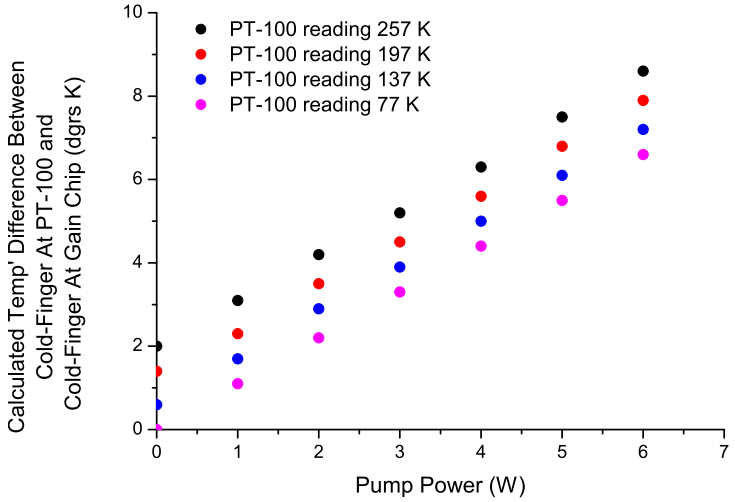

Figure 3.4: The calculated temperature difference between the surface temperature of the cold-finger directly behind the gain chip and the temperature of the cold-finger at the position of the PT-100 plotted against incident pump power.

Figure 3.4 shows that the temperature as recorded by the PT-100 is approximately the same as the temperature of the cold-finger directly behind the gain chip: a pump power of 6 W generates a 6 K difference between the two locations when the cold-finger is held at 77 K. Due to this agreement the cold-finger temperature will from now on be defined as that recorded at the position of the PT-100 sensor. The plot also shows that whilst the calculated temperature difference does increase with pump power this increase is unaffected by the heat being emitted from the resistive heater: the gradient of the 77 K plot for which the resistive heater heat-load is 0 W/m^3 is the same as those gradients obtained where the resistive heater heat-load is non-zero.

Initial experimental investigations undertaken using the cryostat resulted in condensation forming on the front surface of the gain chip. This unwanted phenomenon was minimised by using the resistive heater to keep the 'gain chip' end of the cold-finger at 300 K whilst a small amount of liquid nitrogen was simultaneously added into the dewar. This set the local temperature at the base of the dewar to < 273 K and ensured that any moisture in the vacuum chamber would to be drawn to, and condense on, the base of the dewar rather than the front surface of the gain chip. This process was repeated a number of times before any experimental work was undertaken.

3.2.3 The Optical Pump

Initially an 830 nm fibre-coupled diode laser was used to optically pump the cryogenically cooled gain structures. This wavelength was suitable for cold-finger temperatures above 150 K however it became apparent that below this temperature the VECSEL would underperform. An example of this lasing performance can be seen in figure 3.5 which plots the slope efficiency of a typical 830 nm pumped CW-VECSEL as a function of cold-finger temperature: a corresponding plot of threshold pump power against temperature is provided in figure 3.6

This reduction in performance with decreasing temperature was expected to be due to the rapid decrease in the absorption coefficient of GaAs with temperature when evaluated at 1.50 eV (830 nm). This problem was overcome, as evidenced in section 3.4, by changing the pump wavelength to 808 nm. Initially a 4 W, 808 nm source (Lumics LU0808T040-ED05N12A) driven by a 2.5 W diode driver was employed due to equipment availability. Later work then used a 40 W, 808 nm source (Limo LIMO40-L165x3-DL808-EX1634) driven by a 40 W diode driver.

Both sources are fibre-coupled diode lasers. They were collimated in free-space before being coupled into the vacuum chamber through the antireflection coated window. Once inside the cryostat, the pump beam was focussed onto the cold-finger using a lens held in a vacuum-compatible, manually positionable mount.

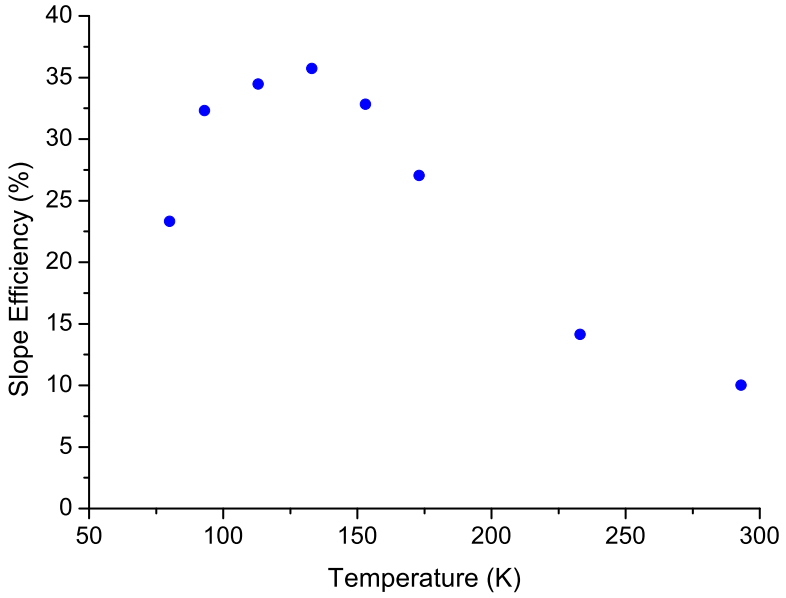

Figure 3.5: The slope efficiency of a typical 830 nm pumped CW-VECSEL as a function of cold-finger temperature. The slope efficiency rapidly reduces for temperatures below 150 K. See text for details.

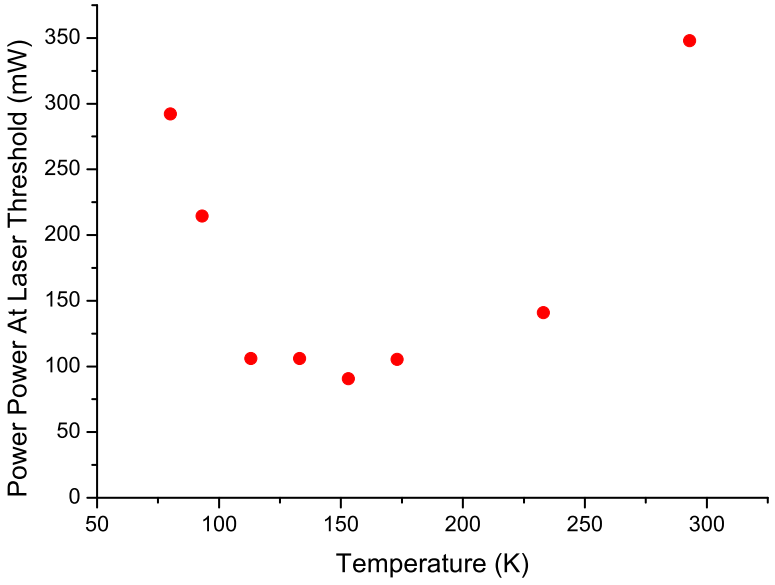

Figure 3.6: The pump power required for a typical 830-nm pumped, CW-VECSEL to reach laser threshold plotted against cold-finger temperature. The laser threshold rapidly increases for temperatures below 125 K. See text for details.

3.2.4 Cavity Alignment In Vacuum

A consequence of sealing the VECSEL within a vacuum chamber is the need for motorised stages and mounts to both position the VECSEL components into a lasing configuration and optimise the cavity geometry. This work used a selection of piezo driven stages and mirror mounts from Newport's Agilis range to position the output coupler and, when used, the SESAM. The position of the gain chip and, when used, the fold mirror was not adjustable. A Python script was written to interface and control these motorised components with a standard QWERTY keyboard.

The linear stages used had a travel range of 12 mm, a minimum incremental motion of 0.05 μm and an absolute positioning accuracy of 100 μm. By combining these stages using brackets, the VECSEL component could by positioned with respect to all three dimensions. The mirror mounts provided angular control over the VECSEL components and had a tip and tilt angular range of $\pm 2°$, an adjustment sensitivity of 2 μrad and an absolute positioning accuracy of 0.05°. Technical drawings of these components are provided below in figure 3.7.

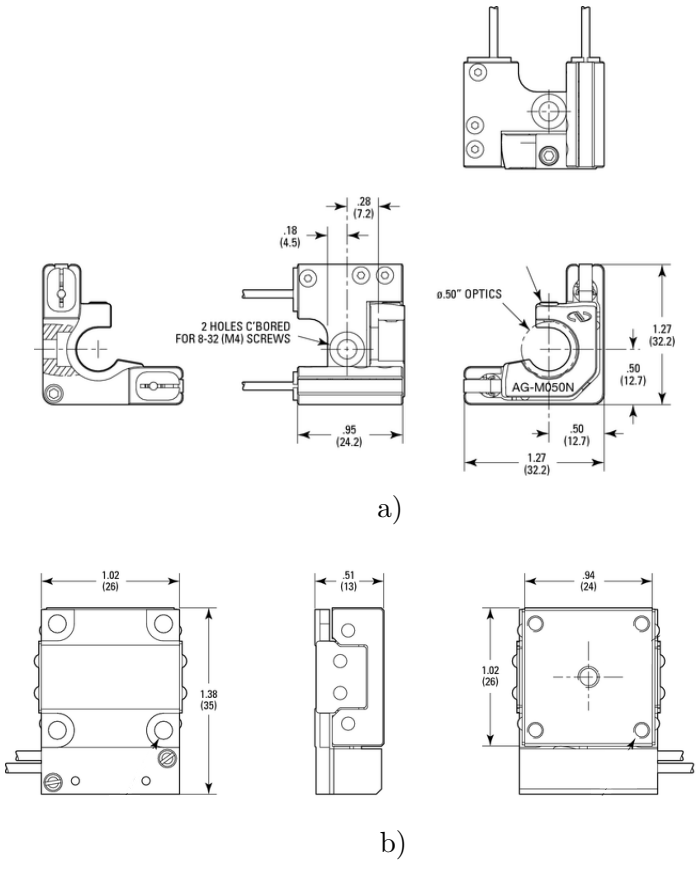

Figure 3.7: Technical drawings of a) the motorised linear stage and b) the optical mount used in the cryostat.

3.3 Application Of The DBR-Shift Method To A Cryogenically Cooled VECSEL Gain Chip

This section reports how the DBR-shift method for determining the absolute temperature of the active region was applied to a gain chip cooled to cryogenic temperatures. This work was undertaken for two reasons. The first reason was to further determine the accuracy of the FEA model presented in section 2.2.1. The second reason was to ensure that the thermal conductance of the bonded gain chip did not undergo a rapid change at cryogenic temperatures. A rapid decrease in the thermal conductance of the gain chip at cryogenic temperatures could lead to a warmer than expected active region and a masking of the expected performance improvements.

3.3.1 The Method

A schematic of the experiment used to determine the temperature of the gain chip when sealed inside the liquid nitrogen cold-finger cryostat is given below in figure 3.8.

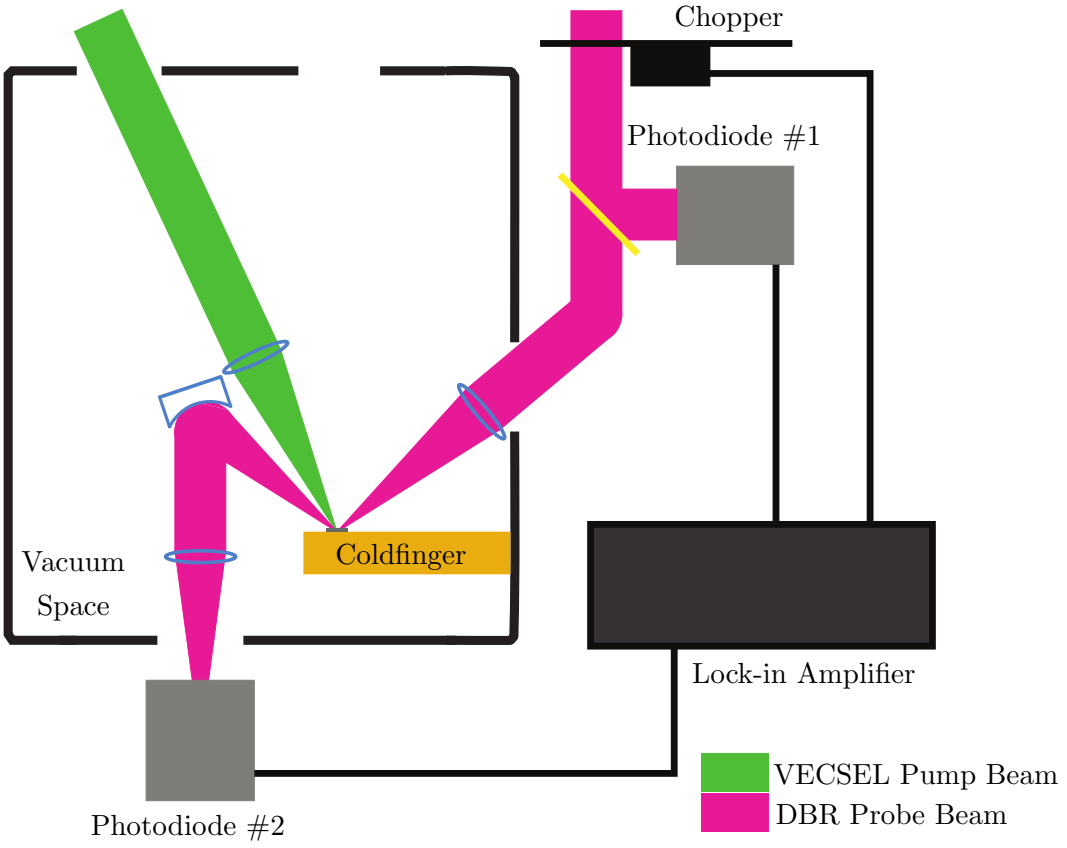

Figure 3.8: Schematic of the 'DBR-shift method' apparatus used to measure the local temperature of a cryogenically cooled VECSEL gain chip.

The gain chip used in this investigation was the same as that used previously in section 2.3. The geometry of the vacuum chamber meant that the gain chip would be illuminated by the probe beam at an angle of 40° from the surface normal. The reflectivity profile of the 27.5 pair AlAs/GaAs DBR was therefore obtained at this new angle of incidence using a spectrophotometer. The long-wavelength half of this plot is shown below in figure 3.9. The measurement was taken at room temperature. From this plot a probe beam wavelength of 1035 nm was chosen.

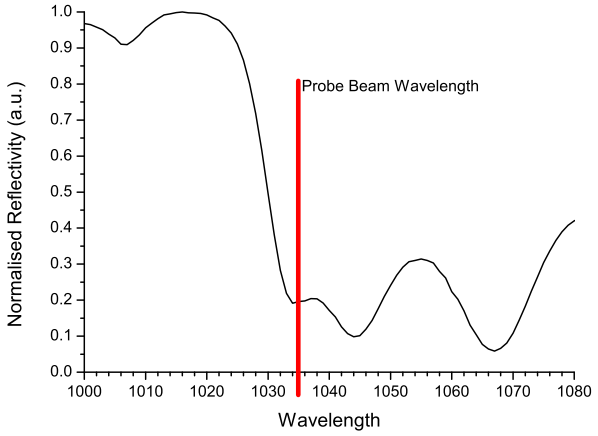

Figure 3.9: The reflectivity profile of a gain chip using a 27.5 pair AlAs/GaAs DBR, held at 300 K, and illuminated at an angle of approximately 40° from the surface normal. From this measurement a probe beam wavelength of 1035 nm was chosen.

The probe VECSEL used in the investigation was constructed using a gain chip with a design wavelength of 1040 nm. The VECSEL produced a diffraction-limited, $TEM_{0,0}$, CW beam and the wavelength was set precisely at 1035 nm and stabilised through the use of an uncoated, fused-silica, intracavity etalon. An optical spectrum of the probe beam is given below in figure 3.10.

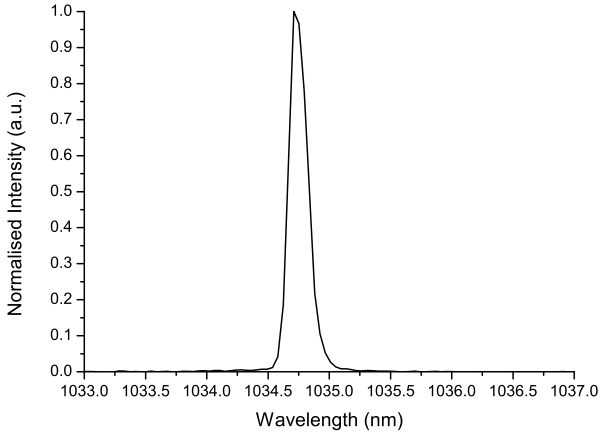

Figure 3.10: Optical spectrum of the VECSEL probe beam.

The VECSEL gain chip was bonded using silver paint to the copper cold-finger of the cryostat. As before the probe beam was directed through a collimating lens and a set of neutral density filters in order to attenuate the power to < 1 mW. The probe beam was then routed through a chopper and split in two with a 50:50 pellicle beam splitter. One arm of the split beam was used to illuminate an InGaAs photodiode and the other was passed through a window in the vacuum chamber and focussed to a 60 μm radius spot on the surface of the gain chip. The reflection of this probe beam was then recollimated, routed out of the vacuum chamber and focussed onto a second InGaAs photodiode. The signal from the two photodiodes and the reference signal from the chopper were fed to a lock-in amplifier, the output of which was displayed on an oscilloscope. Again it is important to note that the two photodiodes were not calibrated relative to each other as the absolute reflectivity was not being investigated.

The reflectivity parameter space was explored for cold-finger temperatures between 83 and 313 K in steps of 10 K and for pump powers between 0 and 2.5 W in steps of approximately 150 mW. Although it would have been desirable to investigate pump powers greater than 2.5 W this was not possible as, at the time, no higher power laser-diode driver was available. The data collection procedure implemented was the same as that described in section 2.3.1 and the data was analysed using the method previously described in section 2.3.2.

3.3.2 Experimental Results

The gain chip is assumed, for the reasons given on page 40, to be in thermal equilibrium with the cold-finger when no pump power is applied. A measurement of the gain chip reflectivity, for no applied pump power, and as a function of cold-finger temperature was made using the method detailed in section 2.3.1. The reflectivity of the gain chip was then measured as a function of both cold-finger temperature and incident pump power and comparative plots of reflectivity against cold-finger temperature for a given applied pump power were obtained.

An example of such a plot is given on the following page in figure 3.11: this plot shows the calibration curve obtained for no applied pump power and the reflectivity curve obtained for an incident pump power of 2.25 W. As stated in the previous chapter the reflectivity recorded for some known combination of incident pump power and cold-finger temperature can be mapped on to the reflectivity curve obtained for no applied pump power through an x-axis translation (a translation in temperature). This procedure yields the absolute active region temperature for a given incident pump power and cold-finger temperature.

By applying this method to the entire data-set a plot of active region temperature against incident pump power for various cold-finger temperatures was obtained: this is shown in figure 3.12. This plot shows that for a cold-finger temperature of 83 K, an incident pump power of 2.25 W raises the active region temperature by ≈ 55 K.

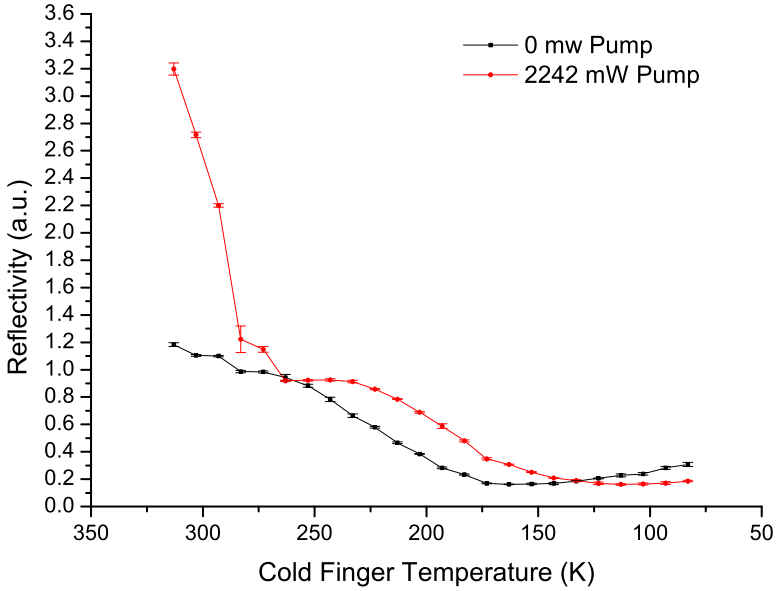

Figure 3.11: The measured gain chip reflectivity (not normalised) plotted against heat-sink temperature for 0 and 2.25 W of pump power. By mapping the data points obtained for 2.25 W of pump power onto the 0 W calibration curve, an increase in temperature from a known baseline is obtained.

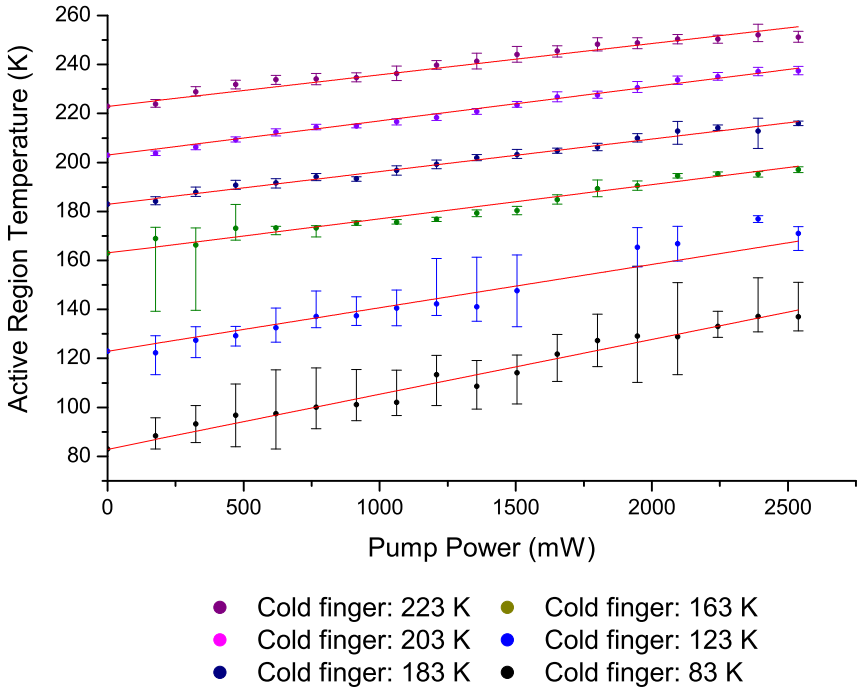

Figure 3.12: The extracted absolute active region temperature plotted against incident pump power for varying cold-finger temperatures. For 0 mW pump power thermal equilibrium is assumed between the cold finger and the active region. Consequently the lines of best fit must pass through the y-axis at the cold-finger temperature.

By fitting a straight line to the data obtained for a cold-finger temperature of 83 K a gradient of 22.6 x 10^{-3} ± 0.2 x 10^{-3} K/mW is measured: figure 2.13 showed this value to be 22.36 x 10^{-3} ± 0.4 x 10^{-3} K/mW for a cold-finger temperature of 303 K. This shows that the thermal conductance of the bonded gain chip does not significantly change when cooled to cryogenic temperatures. It also allows an upper limit to be placed on the maximum incident pump power tolerated by the chip prior to thermal rollover: assuming an active region rollover temperature of 400 K and a cold-finger temperature of 83 K the gain chip should be able to tolerate approximately no more than 12 W of incident pump power.

A thermal impedence of 12.78 x 10^{-3} ± 0.3 x 10^{-3} K/mW is measured for a cold-finger temperature of 223 K. This value is approximately valid for cold-finger temperatures between 223 and 163 K and is ≈ 1.75 x smaller than the value obtained for a cold-finger temperature of 303 K. This reduction in thermal impedence is in qualitative agreement with both the behaviour predicted by the FEA model set out in section 2.2.3 and the known temperature-dependent thermal conductivity of GaAs [79].

For cold-finger temperatures below 163 K the thermal impedence of the gain chip increases. Whilst this observation contradicts the known thermal conductivities of the gain chip materials and the FEA model presented in section 2.2.3, a number of phenomena could contribute to this unexpected behaviour.

Firstly it is not clear what effect the cryogenic temperatures had on the silver-paint used to bond the gain chip to the cold-finger. A reduction in the thermal conductivity of the silver paint could cause a thermal bottleneck to occur between the gain chip and cold-finger thus leading to an apparent increase in the thermal impedence of the gain chip. Despite an extensive literature search the technical data needed to explore this idea could not be found and therefore, in order to quantify this phenomena properly, a dedicated study would need to be undertaken. Due to time constraints it was not possible for the author to undertake this study and therefore it is left to the interested reader to further explore this possibility.

Secondly the FEA simulation uses both a classical approach when computing the movement of heat within the gain chip and a simplified gain chip geometry. The phonon occupation probability is therefore neglected as is the impact of material interfaces on phonon transport within the structure and the contribution to the thermal impedence resulting from the omitted material interfaces. The effect of material interfaces on phonon transport in a semiconductor stack has been well documented [80, 81] and the model's failure to include this physics is likely to result in a calculated thermal impedence that is smaller than the value measured experimentally. Whilst it is conceivable that this physics could be incorporated into the heat transport simulation, to do so would require microscopic modelling of the gain chip. This is deemed beyond the scope of this research and instead it is left to the interested reader to develop this model further.

A third explanation is that as the gain structure cools the reflectivity profile of the DBR will shift in wavelength and this could alter the proportion of pump light that is reflected back through the active region of the gain chip. For an 80 K change in temperature, the corresponding 8 nm wavelength shift in the DBR reflectivity profile could cause a variation of up to 60 % in the amount of pump light reflected. This will have the effect of reproportioning the heat load between the DBR and the active region as well as reducing the amount of pump light absorbed by the gain structure. It is therefore conceivable that a gain chip held at 83 K could absorb more pump light into the DBR than the same structure held at 163 K and, because the conversion of pump power to heat in the DBR is, to a good approximation, 1 the gain chip held at 83 K will warm more quickly.

In order to further explore this third explanation a modified version of the FEA model detailed in section 2.2.3 was created. In this model a new variable, η_{ref}, was introduced that accounted for the temperature dependent DBR reflectivity at the pump wavelength. This was achieved by approximating the reflectivity profile of the DBR around 808 nm as a sine-function with an x-axis variable that corresponded to wavelength. This approximation is plotted alongside the measured reflectivity in figure 3.13 below. The rate at which the reflectivity profile of the DBR shifts in respect to wavelength is known to be 0.1 nmK^{-1} and this is equivalent to evaluating the newly created sine-function for a wavelength that shifts by the same amount but in the opposite direction. The incorporation of this new variable is shown explicitly in equation 3.1.

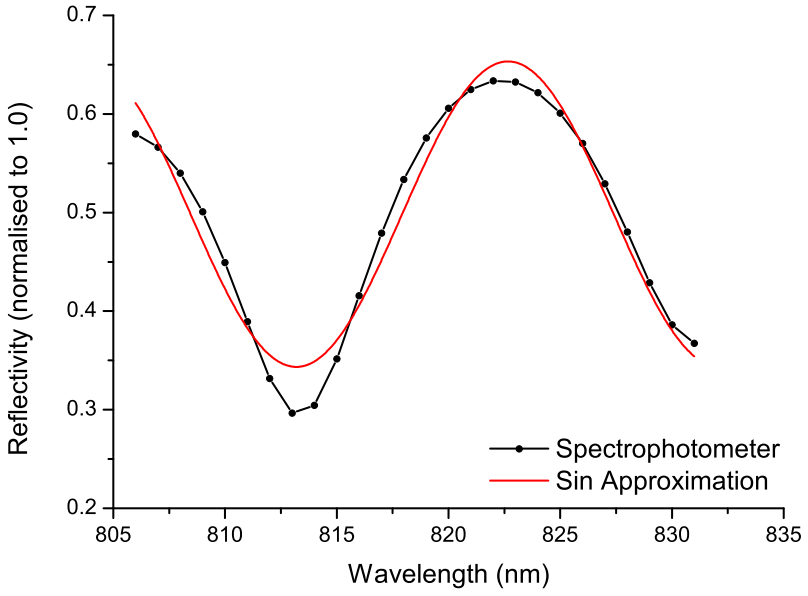

Figure 3.13: The measured and approximated DBR reflectivity. The approximated DBR reflectivity is used to incorporate a temperature dependency into the quantity used to represent the percentage of pump light reflected back through the active region by the DBR.

$$Q_{DBR}(r,z) = \frac{(1-\eta_{ref})\eta_d\eta_T P_p \alpha_d}{\pi\omega_p^2} e^{-\alpha_d(z_{0_d}-z)} e^{-\alpha_g t_g} \tag{3.1a}$$

$$\text{for } r \leq \omega_p$$

where

$$\eta_{ref} = y_0 + A\sin\left(\frac{\pi(\lambda_{pump-apparent} - x_c)}{x_d}\right), \tag{3.1b}$$

and

$$\lambda_{pump-apparent} = \lambda_{pump} + 0.1(T_{room} - T). \tag{3.1c}$$

The values used in equation 3.1b are given below in table 3.1:

Symbol	Value
y_0	0.4984
A	0.1549
x_c	2.073x10^{-7} m
x_d	9.467x10^{-9} m

Table 3.1: Values used in the sine-function approximation of the DBR side-band.

The expression for the heat load in the active region was also modified to include the absorption of the light passing back through the active region as a consequence of being reflected by the DBR:

$$Q_{activeregion}(r,z) = \frac{\eta_g\eta_T P_p \alpha_g}{\pi\omega_p^2}\left(e^{-\alpha_g(z_{0_g}-z)} + \eta_{ref} e^{-\alpha_g(t_g-(z_{0_d}-z))}\right). \tag{3.2}$$

As before

$$Q_{gain}(r,z) = Q_{DBR}(r,z) = 0 \qquad \text{for} \qquad r > \omega_p. \tag{3.3}$$

The quantities used in these equations can be found in table 2.1 in section 2.2.3. By making these alterations to the model a temperature dependency has now been incorporated into the pump absorption fraction, the quantum defect and the fraction of light reflected by the DBR.

In order to show that this modified FEA model can approximately reproduce the form of the experimental data, the model is used to calculate the rise in active region temperature for an incident pump power of 2.5 W and for cold-finger temperatures between 83 and 183 K in steps of 20 K. The resultant graph is given on the following page in figure 3.14. Included in this plot is the corresponding experimentally obtained data. It can be seen that the modified FEA model is able to approximately reproduce the form of the experimental data.

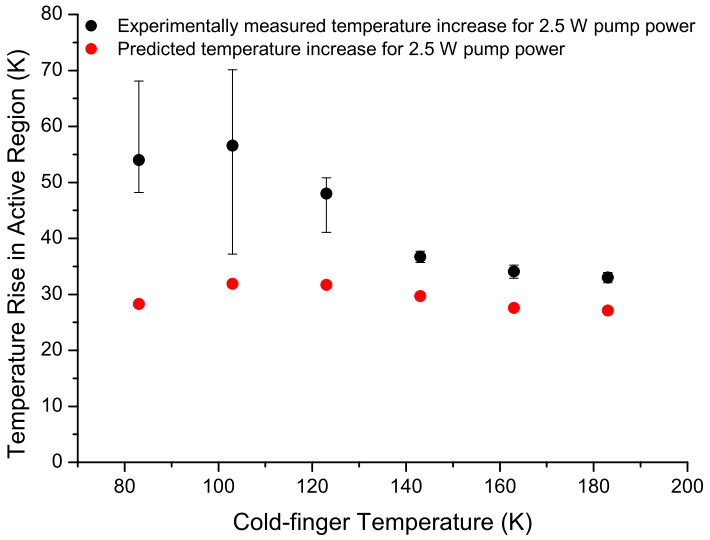

Figure 3.14: The experimentally measured rise in active region temperature compared to the rise calculated using the modified FEA model and plotted against cold-finger temperature. Both the experimental data and the FEA-model were evaluated for an incident pump power of 2.5 W.

A quantitative comparison between the FEA model and the experimentally obtained data clearly shows that the model is not able to reproduce the magnitude of the effect. It is expected that better agreement between the calculated and measured data could be achieved by replacing the sine-function used to approximate the reflectivity profile of the DBR sideband with a high-order polynomial curve.

Other factors affecting this discrepancy could include the reasons given previously on page 47 and those discussed in section 2.2.3. The model's assumption that heating in the active region is caused only by the quantum defect is not thought to be significant as the rate of non-radiative Auger recombination is expected to decrease with decreasing temperature and this in turn should reduce the thermal impedence of the gain chip. The suggestion that the measured thermal impedence may be influenced by the action of the resistive heater is discounted due the work undertaken in section 3.2.2.

Both the experimentally measured active region temperature and the active region temperature calculated using the modified FEA model are plotted against incident pump power in figure 3.15. This comparison is made for a cold-finger temperature of 83 K and an incident pump power of between 0 and 2.5 W. The FEA model agrees with the experimentally measured data to within a calculated mean error of 19 K: the standard deviation on the error is calculated to be 13 K.

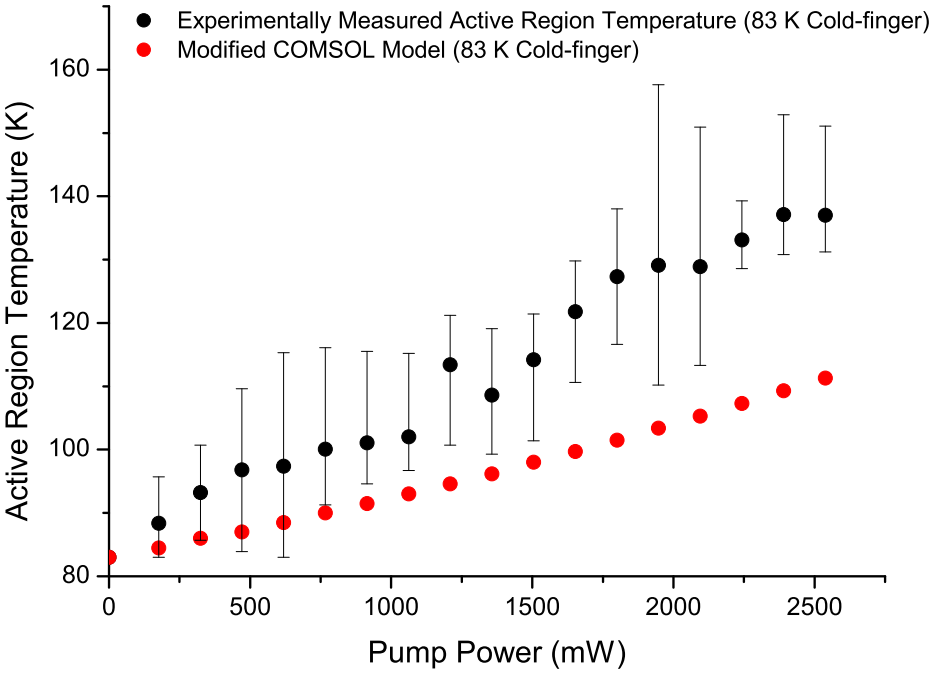

Figure 3.15: A comparison between the experimentally measured active region temperature and the active region temperature calculated using the modified FEA model. This comparison is made for a cold-finger temperature of 83 K and an incident pump power of between 0 and 2.5 W.

Assuming an active region rollover temperature of 400 K and a cold-finger temperature of 83 K, the FEA model therefore predicts that the gain chip will tolerate at least 10 W of incident pump power prior to thermal rollover. By combining this result with the 'heat rise per mW incident pump power' obtained using the DBR-shift method, an upper limit of between 10 and 12 W is placed on the maximum tolerated incident pump power prior to thermal rollover for a gain chip held in thermal contact with a cold-finger at 83 K.

This calculated maximum incident pump power is likely to be an over-estimate as it does not take into account the heat-load produced by non-radiative Auger recombination: the run-away thermal mechanism that generates the rollover behaviour. It is however a useful quantity to obtain as it helps to inform what power pump laser should be used in order to ensure that a VECSEL using a cryogenically cooled gain chip will not be pump power limited. For this reason the 4 W, 808 nm source (Lumics LU0808T040-ED05N12A) driven by a 2.5 W diode driver was replaced with a 40 W, 808 nm source (Limo LIMO40-L165x3-DL808-EX1634) driven by a 40 W diode driver.

3.4 A Cryogenic CW-VECSEL

In this section a CW-VECSEL using a cryogenically cooled gain chip is reported. The gain chip was cooled using the liquid nitrogen cold-finger cryostat presented in section 3.2. This section begins by discussing why the gain chip used in this work was selected: this is done in section 3.4.1. The top-surface photoluminescence, measured for cold-finger temperatures in the range 293 to 83 K, is then presented and discussed. Section 3.4.3 describes the cryogenic CW-VECSEL design and the measured lasing performance, obtained at different cold-finger temperatures, is then reported: a measurement of the incident pump power required at the laser threshold is presented and discussed in section 3.4.4 and a measurement of the output power as a function of incident pump power is presented and discussed in section 3.4.5.

3.4.1 Gain Chip Selection

The emission wavelength of a quantum well is expected to shift at 0.3 nmK^{-1} [8]. To ensure that a fair comparison of VECSEL performance could be made at each investigated cold-finger temperature, it was desirable to choose a gain chip that would interact equally with the laser mode at any wavelength over the expected 64 nm range.

The longitudinal confinement factor (LCF) of a gain chip exhibits an inherent temperature dependence of 0.1 nmK^{-1} arising from the temperature dependent refractive index of the microcavity. It also exhibits a wavelength dependence and, as the emission wavelength of the quantum well is itself temperature dependent, this wavelength dependence can also be thought of as a second temperature dependence.

The variation of the LCF, calculated for a $7\lambda/2$, antiresonant gain chip and evaluated at the temperature-dependent quantum well emission wavelength, is plotted as a function of cold-finger temperature in figure 3.16. It can be seen that over the investigated temperature range the LCF response is far from the flat: the value at 80 K is 2.4 times the value at 293 K. If this gain chip were used then a temperature dependent variation in lasing performance could be obscured by the change in magnitude of the LCF.

By shortening the length of the gain chip micro-cavity the LCF response can be flattened. This is shown in figure 3.17 on the following page. This figure plots the LCF against wavelength for a $4.5\lambda/2$ antiresonant gain chip operating both at 293 K and 80 K. The quantum well emission of this gain structure is designed to be $\approx$ 1015 nm at room temperature corresponding to $\approx$ 952 nm at 80 K. This is marked on to figure 3.17 using blue annotation.

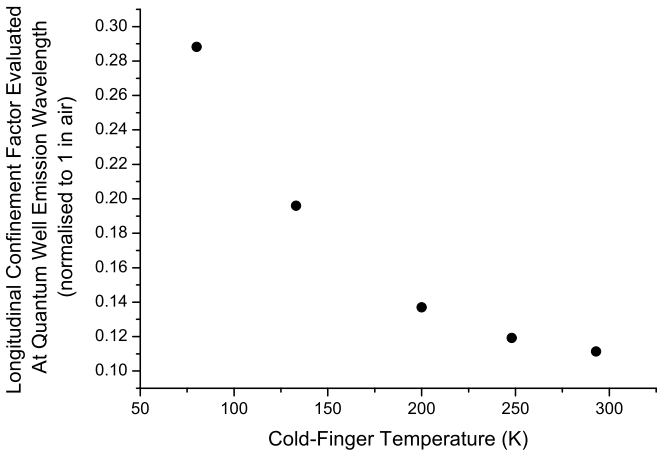

Figure 3.16: The calculated LCF of a $7\lambda/2$, antiresonant gain chip, evaluated at the temperature dependent quantum well emission wavelength, and plotted against cold-finger temperature.

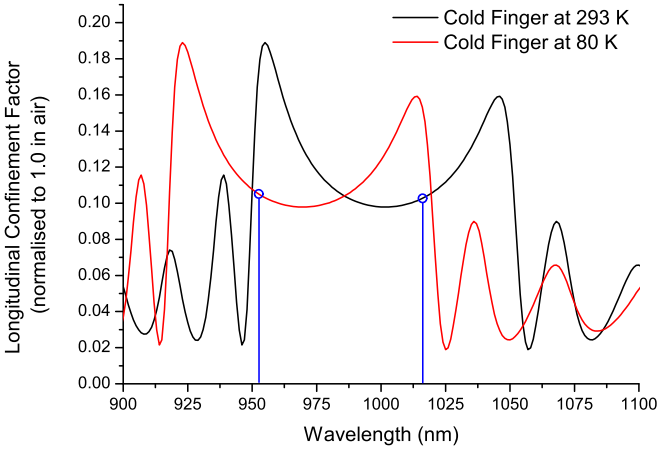

Figure 3.17: The calculated longitudinal confinement factor of a $4.5\lambda/2$, antiresonant gain chip, evaluated at both 293 and 80 K, and plotted against wavelength. Plot was calculated using the matrix formulation method given in [63]. The blue annotation marks the emission wavelength of the quantum wells at 293 and 80 K.

The LCF, evaluated at the temperature-dependent quantum well emission wavelength and calculated for a $4.5\lambda/2$ antiresonant gain chip is plotted against cold-finger temperature in figure 3.18. This plot shows that, as the structure is cooled from 293 to 80 K, the LCF will experience a maximum variation of 0.94-times the value at 293 K and the value of the LCF at 80 K will be 0.999-times the room temperature value. This flat response allows a much fairer comparison to be made between lasing performance and cold-finger temperature and therefore it was this gain chip design that was chosen for the cryogenically cooled CW-VECSEL.

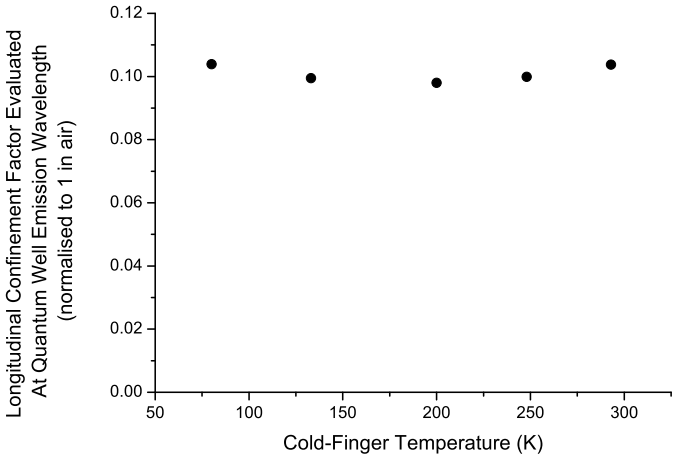

Figure 3.18: The calculated longitudinal confinement factor of a $4.5\lambda/2$, antiresonant gain chip, evaluated at the temperature dependent quantum well emission wavelength, and plotted against cold-finger temperature.

A schematic of the gain chip used in the cryogenically cooled CW-VECSEL is provided below in figure 3.19. The structure was grown using MBE by Dr Ian Farrer at the University of Cambridge and assigned the sample number W0728.

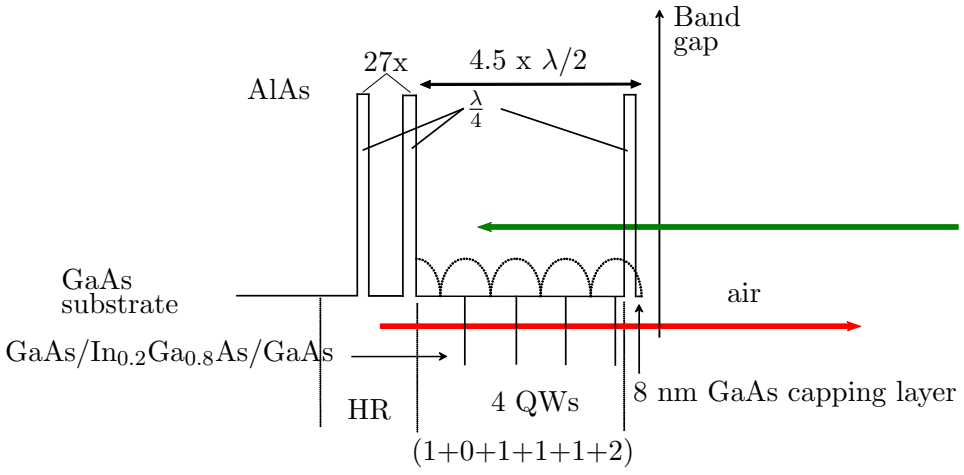

Figure 3.19: Schematic of the $4.5\lambda/2$, antiresonant gain chip used in the cryogenic, CW-VECSEL work.

3.4.2 A Top-Surface Photoluminescence Measurement Undertaken At Cryogenic Temperatures

A top-surface photoluminescence (PL) measurement of the gain chip W0728 was undertaken for temperatures between 293 and 83 K. A square of W0728 measuring 4 mm by 4 mm was cleaved from the wafer and bonded using silver paint to the cold-finger of the

liquid nitrogen cryostat. The cryostat was then evacuated and the chip illuminated with up to 2.5 W of pump power focussed into a 60 μm radius spot. The PL emitted from the top surface of the gain chip was collimated and then directed through the anti-reflection coated cryostat window and into a 0.275 m grating spectrometer. A schematic of the experiment is given below in figure 3.20.

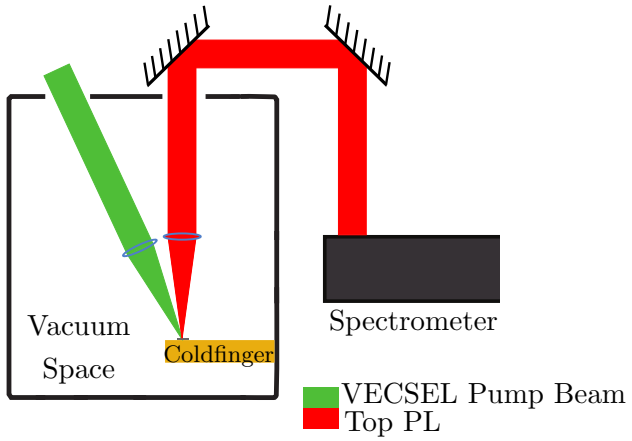

Figure 3.20: Schematic of the experimental set-up used to record the top-surface PL as a function of incident pump power and cold-finger temperature.

The cold-finger was cooled in steps from 293 K to 83 K. At each step the gain chip was illuminated with up to 2.25 W of pump power and the emission spectrum recorded. Figure 3.21 shows a slice through the recorded spectra for 1.2 W of incident pump power.

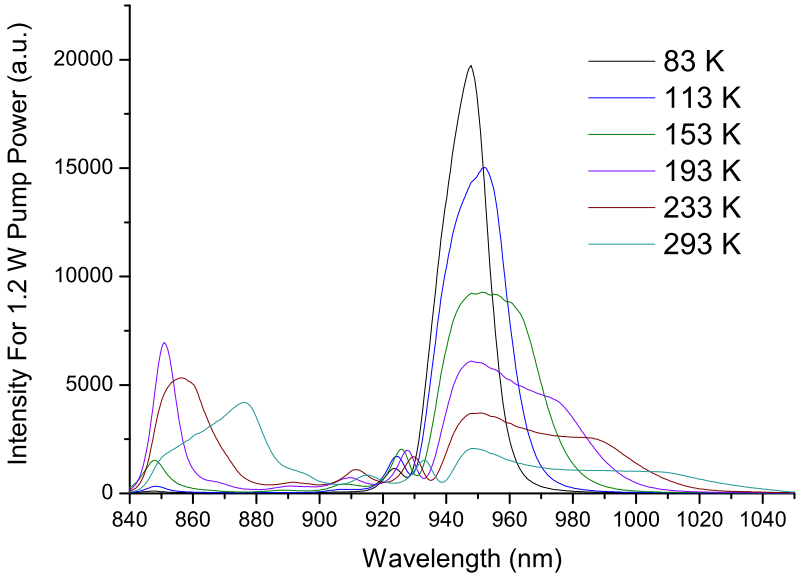

Figure 3.21: The recorded top-surface PL for various cold-finger temperatures between 293 and 83 K. The incident pump power was 1.2 W. For wavelengths longer than 930 nm the optical spectrum of the PL narrows with decreasing cold-finger temperature whilst both the peak height and the integrated area of the curve increase.

Figure 3.21 shows that in the wavelength range dominated by the quantum well emission ($\lambda > 930$ nm) the optical spectrum of the PL narrows with decreasing temperature: at room temperature a width of approximately 110 nm is measured reducing to 56 nm, approximately half the room temperature value, at 83 K. This phenomenon is expected to be caused, at least in part, by the Fermi-Dirac distributions describing the conduction and valence bands steepening with temperature and moving towards a step function. To illustrate this, the Fermi-Dirac expression describing the conduction band (given in equation 2.6) is plotted against quantum well temperature assuming a quantum well carrier density of 1 x 10^{19} cm^{-3}: this plot is given on the following page in figure 3.22.

As the spectral width of the emission narrows both the peak height and the integrated area of the curve increase: the peak height increases by an order of magnitude and the integrated area at 83 K is approximately 4.4 times the room temperature value. Although it is acknowledged that this comparison is not ideal as the temperature dependent refractive index of the gain chip will alter the solid angle over which the PL is collected, the increase in the amount of collected PL is so great that an increase in the available gain at low temperatures is almost certain. This observation is in agreement with the model set out in section 2.2.1.

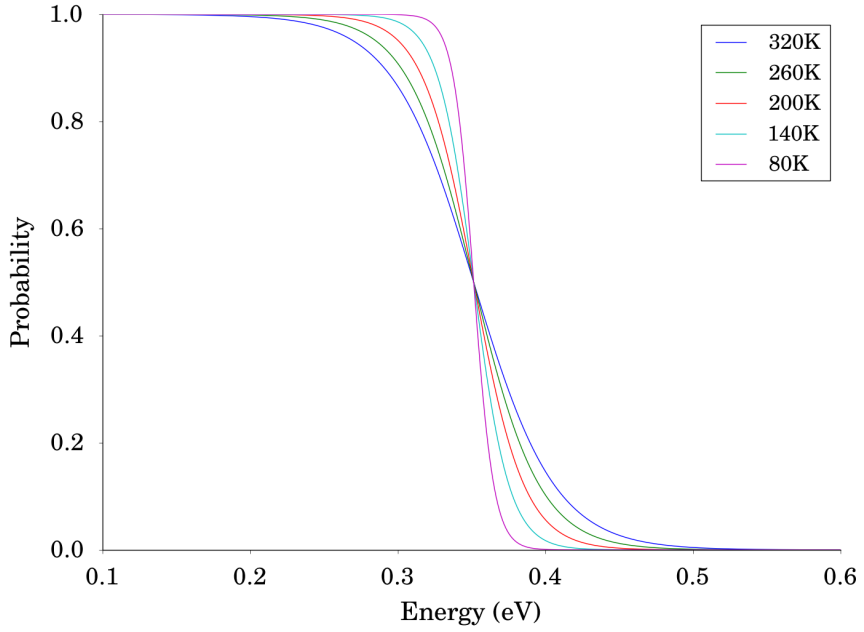

Figure 3.22: The Fermi-Dirac probability plotted against energy and calculated for a quantum well carrier density of 1 x 10^{19} cm^{-3} and various heat-sink temperatures. As the temperature decreases the probability tends to a step function: this will correspond to a narrowing in the emitted PL.

3.4.3 Experimental Method Used To Characterise The Cryogenically Cooled CW-VECSEL

A VECSEL was constructed within the vacuum chamber using a piece of W0728 and a 0.3 % transmission, 75 mm radius of curvature output coupler. The gain structure was pumped by a 40 W, 808 nm source focussed to a 60 μm radius spot on the chip surface. The cavity was aligned and optimised at room temperature. By using a video-camera to image the laser mode incident on the output coupler, a value for the pump power required in order to reach lasing theshold was recorded. Also measured was the output power of the VECSEL as a function of incident pump power (an I/O curve).

The vacuum chamber was then evacuated, the remaining moisture drawn onto the dewar and the cold-finger cooled. During the cooling process the output coupler was imaged continuously and the cavity was constantly reoptimised in order to ensure that the VECSEL continued to operate with a minimised threshold. As the gain chip cooled the threshold pump power value was recorded for various cold-finger temperatures. Upon the cold-finger reaching the destination temperature, an I/O curve was undertaken starting from the minimised threshold value. As the pump power was increased, the cavity was continuously reoptimised to ensure the maximum possible output power was recorded.

The cold-finger was then warmed to room temperature and a third I/O curve recorded. By comparing this I/O curve to that measured prior to the cryogenic cooling, crude information about the structural degradation of the chip could be obtained: if, having been temperature cycled, the laser performance was degraded then it was assumed that the structure of the gain chip had also degraded. The I/O curves recorded after the temperature cycle could only ever be obtained once the front surface of the gain chip had been wiped clean with isopropanol. This suggests that condensation had formed on the surface of the gain chip at some point during the temperature cycle.

An example of this I/O curve comparison is given in figure 3.23. This plot shows the room temperature I/O curves obtained before and after the gain chip was cooled to 83 K and pumped with up to 5.9 W of incident pump power (the I/O curve obtained at 83 K is given later in figure 3.27). Figure 3.23 clearly shows that the temperature cycle causes a deterioration in the the performance of the VECSEL and this observation informed the decision to replace the gain chip after each temperature cycle. It is acknowledged that replacing the gain chip in this way could cause a variation in the VECSEL performance due to variations in the material quality however by using small, neighbouring pieces of W0728 any variation in the lasing performance was minimised.

Measurements of the laser threshold were made for cold-finger temperatures between 293 and 83 K in 20 K steps and I/O power curves were investigated for five cold-finger temperatures between 293 and 83 K.

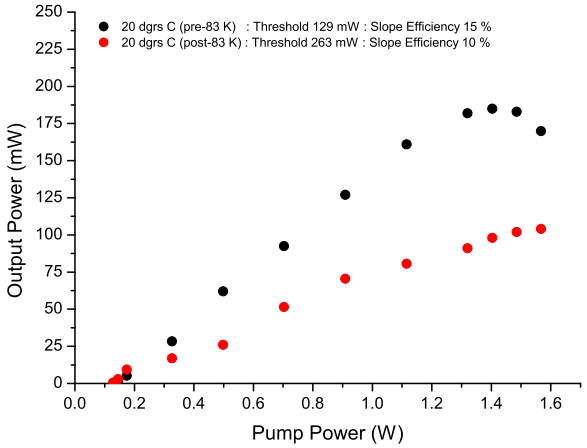

Figure 3.23: The room temperature I/O curves obtained before and after the gain chip was cooled to 83 K and illuminated with up to 5.9 W. The plot clearly shows that this temperature cycle has deteriorated the laser performance.

3.4.4 Characterisation Of The VECSEL Threshold

The experimentally measured incident pump power required to reach lasing threshold is plotted against cold-finger temperature in figure 3.24. Multiple investigations were made at each cold-finger temperature, each time with a fresh piece of gain chip. The data points plotted are therefore the mean values of incident pump power: the error bars are the calculated standard deviations. An exponential decay with a decay constant of 0.0166 ± 0.004 K^{-1} has been fitted to the data.

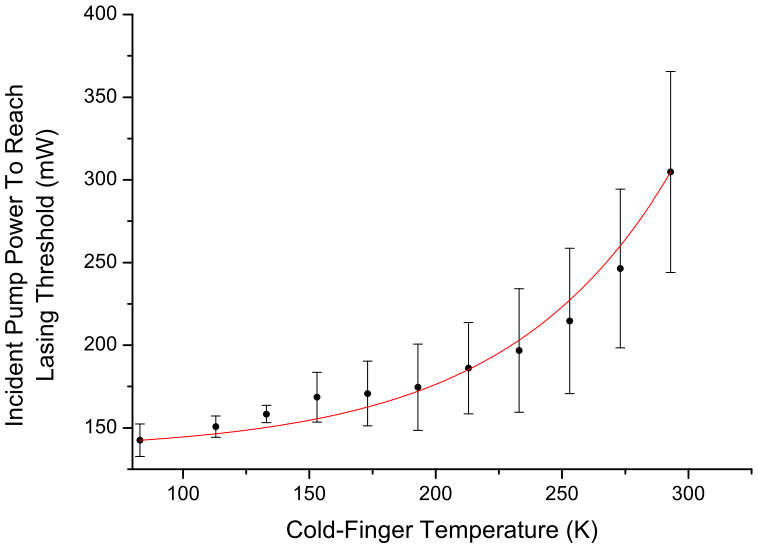

Figure 3.24: The measured incident pump power required to reach lasing threshold plotted against cold-finger temperature. An exponential decay, with a decay constant of 0.0166 ± 0.004 K^{-1} has been fitted to the data.

The data presented in figure 3.24 show that, for a cold-finger temperature of 83 K, the amount of incident pump power required to reach the VECSEL laser-threshold is 53 % ± 10 % less than that required for a cold-finger temperature of 293 K. Correspondingly, the gain model presented in section 2.2.1, calculates that over the same temperature range a 72 % reduction should occur in the quantum well carrier density. The gain model also calculates that the reduction in quantum well carrier density will reduce linearly with temperature: the experimentally observed reduction in incident pump power takes the form of an exponential variation. It was thought that this discrepancy could be due to the gain model failing to take into account the carrier trapping efficiency of the quantum well.

In order to test this idea the Fermi-Dirac probability functions describing the quantum well electron and hole populations were integrated with respect to energy for quantum well temperatures between 320 and 80 K in steps of 20 K. The Fermi energy used in each calculation assumed an 8 nm-thick, $In_{0.2}Ga_{0.8}As$ quantum well emitting at 1020 nm and a carrier density equal to the threshold carrier density as calculated by the gain model. For each temperature step the Fermi-Dirac function was first integrated between 0 and ∞ and then between the escape energy of the quantum well (0.125 eV above the conduction band for electrons and 0.084 eV below the valence band for holes) and ∞. The proportion of each distribution existing outside of the quantum well confinement energy could therefore be deduced with respect to temperature and this is plotted in figure 3.25.

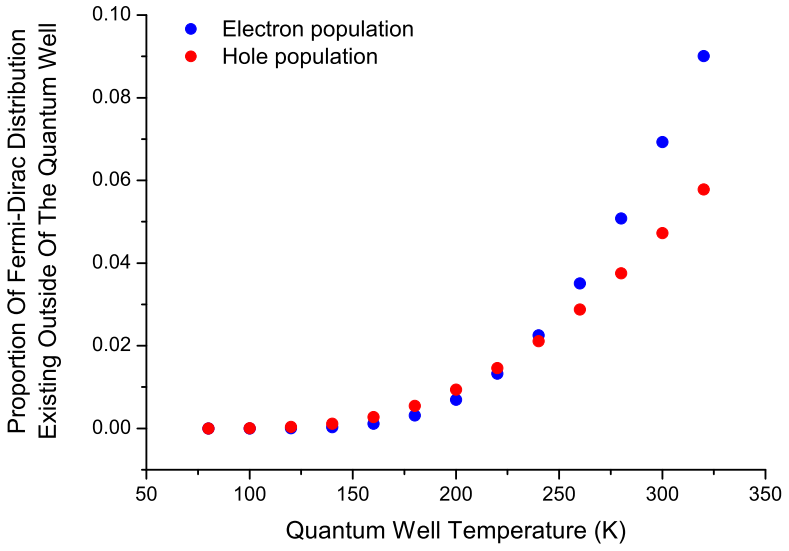

Figure 3.25: The proportion of the electron and hole Fermi-Dirac distributions existing outside of the quantum well confinement energy and plotted with respect to quantum well temperature: the Fermi energy assumed an 8 nm thick, $In_{0.2}Ga_{0.8}As$ quantum well emitting at 1020 nm and a carrier density equal to the threshold carrier density as calculated by the gain model in section 2.2.1

Figure 3.25 shows that by cooling the quantum well from 320 to 80 K, a non-linear reduction occurs in the proportion of the electron and hole Fermi-Dirac distributions that exist outside of the quantum well barrier energy. An exponential fit with a decay constant of 0.0155 ± 0.001 K^{-1} best approximates the data set corresponding to the electron Fermi-Dirac distribution and an exponential fit with a decay constant of 0.011 ± 0.001 K^{-1} best approximates the data set corresponding to the hole Fermi-Dirac distribution. Figure 3.25 also shows that the trapping efficiency of the quantum well will be dominated by the confinement of the electron population.

The calculated decay constant describing the temperature dependent confinement of the electron Fermi-Dirac distribution agrees with the experimentally obtained decay constant describing the reduction in incident pump power required to reach laser-threshold to within the tolerance of the error: 0.0155 ± 0.001 K^{-1} and 0.0166 ± 0.004 K^{-1} respectively. Consequently the temperature dependent confinement of the electron population is likely to be partly responsible for the observed reduction in threshold pump power.

A plot of the laser threshold optical spectrum for different cold-finger temperatures is given below in figure 3.26. It can be seen that over the 210 K temperature range the lasing wavelength shifted by 65 nm: a rate of 0.3 nm K^{-1}. This tuning rate was initally incorporated as an assumption into the theoretical models and so, by confirming this rate experimentally, the theoretical work is placed on a firmer footing. This observation also helped to inform the choice of gain and SESAM structure used in the cryogenic modelocked VECSEL presented in the following section.

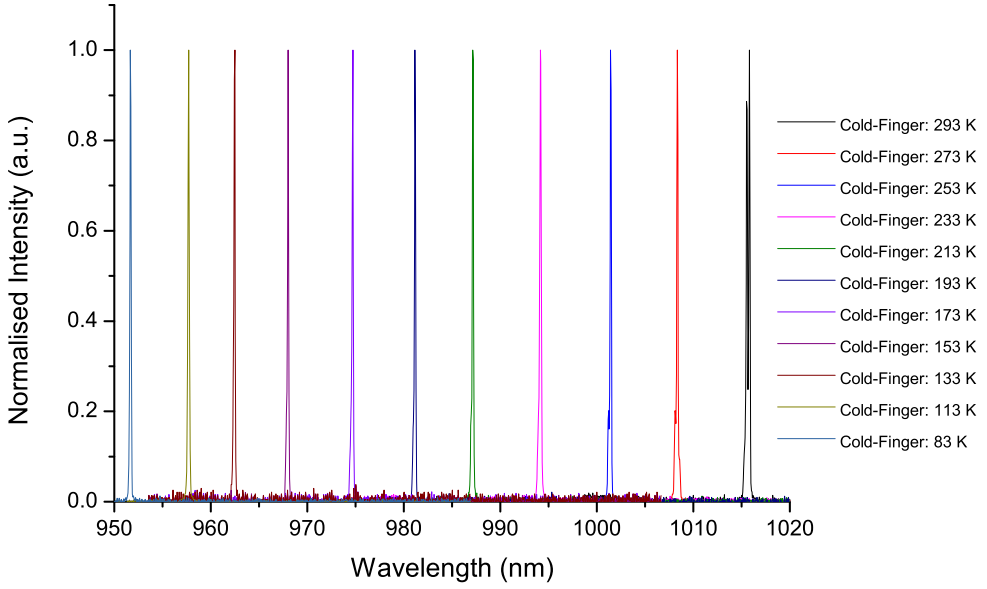

Figure 3.26: The optical spectrum of the VECSEL at the point of laser threshold and for cold-finger temperatures between 293 and 83 K. A shift in the optical spectrum of 0.3 nmK^{-1} is extracted.

3.4.5 Characterisation Of The VECSEL Output Power

The decision to replace the gain chip after each temperature cycle does not affect the comparison between the initial operation of the gain chip at room temperature and the subsequent cryogenic operation of the same gain chip. Consequently the relative increase in output power with respect to cold-finger temperature can be obtained and compared across cold-finger temperatures.

An example pair of I/O curves is given below in figure 3.27. This plot shows both the I/O curve obtained for the VECSEL when it was operated with a gain chip maintained at a cold-finger temperature of 83 K and the corresponding room temperature measurement. It can be seen that by reducing the cold-finger temperature from 293 to 83 K the gain chip is able to tolerate a 4-fold increase in incident pump power prior to the onset of thermal rollover. Consequently the output power of the VECSEL increased from 143 mW to 1540 mW: an increase of more than an order of magnitude. The optical spectrum of the VECSEL is shown for various incident pump powers in figure 3.28 on the following page.

The VECSEL stopped lasing for incident pump powers greater than 5.9 W. Lasing could be recovered by warming the cold-finger back to room temperature and wiping the front surface of the gain chip with isoproponal however this recovered performance was greatly diminished when compared with previous room temperature performance (figure 3.23).

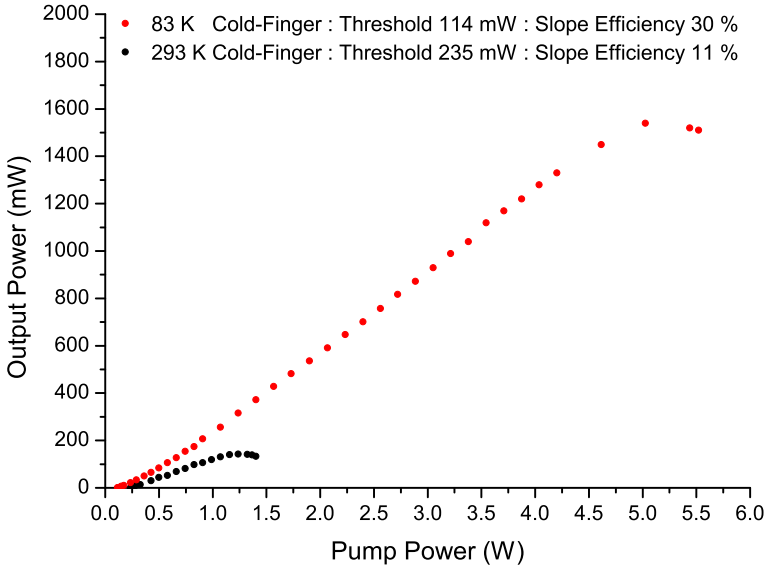

Figure 3.27: The I/O curve measured for the VECSEL when it was operated with a gain chip maintained at a cold-finger temperature of 83 K and the corresponding room temperature measurement. A 4-fold increase in incident pump power prior to the onset of thermal rollover and a corresponding 10-fold increase in output power is measured as a result of cooling the gain chip.

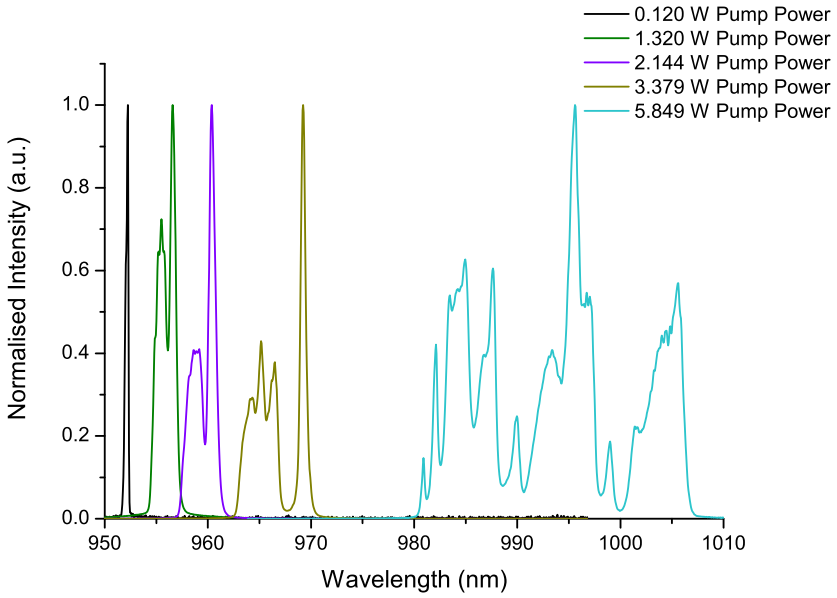

Figure 3.28: The optical spectrum of the VECSEL plotted for five values of incident pump power. The cold-finger temperature and laser threshold pump power were 83 K and 120 mW respectively.

By characterising the VECSEL output power the slope efficiency can be calculated. This is plotted against cold-finger temperature in figure 3.29. Also plotted is the measured incident pump power required to reach lasing threshold reported in the previous section. Whilst it would have been preferable to record I/O curves (and consequently slope efficiencies) at cold-finger temperatures other than the five visited, due to time constraints and shortages in the supply of gain chip wafers it was not possible to do this.

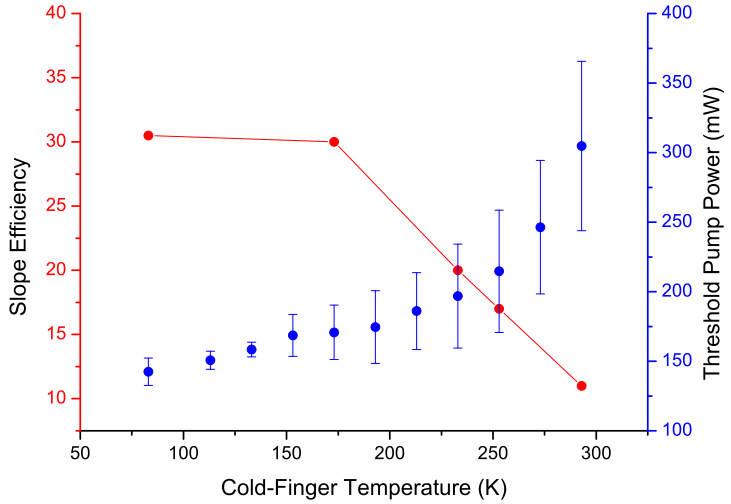

Figure 3.29: The measured slope efficiency and the separately measured incident pump power at laser threshold plotted against cold-finger temperature. Both data sets saturate at approximately 150 K. The line connecting the slope efficiency data points has no theoretical significance and is included to help guide the eyes of the reader.

Figure 3.29 shows that the slope efficiency of the VECSEL increases 3-fold, from 10 % to 30 %, for a 210 K reduction in cold-finger temperature. The slope efficiency of the VECSEL is seen to saturate for temperatures below 150 K: this temperature also coincides with a saturation in the threshold incident pump power. The observed increase and saturation in slope efficiency is therefore expected to be due to, at least in part, the increased trapping efficiency of the quantum wells occuring due to the reduction in the temperature dependent Fermi energy. Again it is extremely difficult to link the absolute values of the slope efficiency, incident pump power at laser-threshold, system temperature and output power without deriving a full microscopic model of the gain chip and, due the complexity of this task and that others are already undertaking this work [24], this approach is deemed beyond the scope of this work.

Analysis of figure 3.28 shows that between laser-threshold (0.120 W) and thermal rollover (5.849 W) the optical spectrum broadens and shifts to longer wavelengths: at threshold the optical spectrum is 0.3 nm wide and centred at 952 nm and at thermal rollover the optical spectrum is approximately 25 nm wide and centred at approximately 995 nm.

Assuming a spectral tuning rate of 0.3 nmK^{-1} the observed 56 nm shift in wavelength (from 952 nm to 1008 nm) corresponds to an increase in temperature of 187 K. The temperature map of the gain chip given in figure 2.4 shows that the temperature of both the active region and DBR is approximately equal and therefore by using the result obtained from the DBR-shift method this temperature rise is calculated to correspond to an active region temperature of 270 K. This value is approximately 100 K less than the expected value at thermal rollover suggesting that the laser did not roll-over due to Auger-induced non-radiative recombination.

The laser may instead have succumbed to mechanical failure. As shown in figure 2.4, a large thermal gradient is expected to exist between the substrate and front surface of the gain chip. This thermal gradient will most probably cause differential thermal contraction to occur resulting in the gain chip succumbing to mechanical failure. This suggestion is further substantiated by the observation that lasing was not recovered when the incident pump power was reduced back to levels at which lasing was previously observed. This idea could be further explored by investigating a FEA thermal-stress model of the gain chip and it is left to the interested reader to attempt this.

The increased width of the optical spectrum with increasing incident pump power is thought to be due to two mechanisms. Firstly the increasing incident pump power corresponds to an increasing active region temperature and this will broaden each quantum well's Fermi-Dirac function (see section 3.4.2). Secondly, assuming that the FEA model used to construct figure 2.4 is not exact, a thermal gradient that increases with increasing pump power could exist between the top and bottom surfaces of the active region.

This in turn could cause the set of quantum wells to exhibit a graded trapping efficiency that becomes more pronounced with increasing pump power. The corresponding spectral emission would therefore broaden with increased pump power.

The data plotted in figure 3.28 tentatively supports this second mechanism. At laser threshold little heat is being generated within the gain chip and so all quantum wells will be trapping with equal efficiency. Correspondingly the optical spectrum is a single narrow peak. For 1.3 W of incident pump power the optical spectrum is shown to have two peaks corresponding, perhaps, to the increased thermal gradient decreasing the trapping efficiency of the top-most quantum well, altering the carrier population within this well and consequently splitting it's emission away from the emission of the second, third and fourth quantum wells. For 3.3 W of incident pump power the optical spectrum is seen to have three clear peaks with a fourth peak developing: this suggests, perhaps, that the thermal gradient is now steep enough to have a pronounced effect on the trapping efficiencies of all quantum wells. The resultant inhomogeneous carrier population would consequently spread the emission wavelength of the four quantum wells far enough apart to allow each quantum well emission to be individually resolved.

Figure 3.30 compares the experimentally measured maximum incident pump power tolerated by the gain chip prior to the onset of thermal rollover to the value predicted by the FEA model: these quantities are plotted in multiples of the room temperature (1.3 W at 293 K) value and against cold-finger temperature.

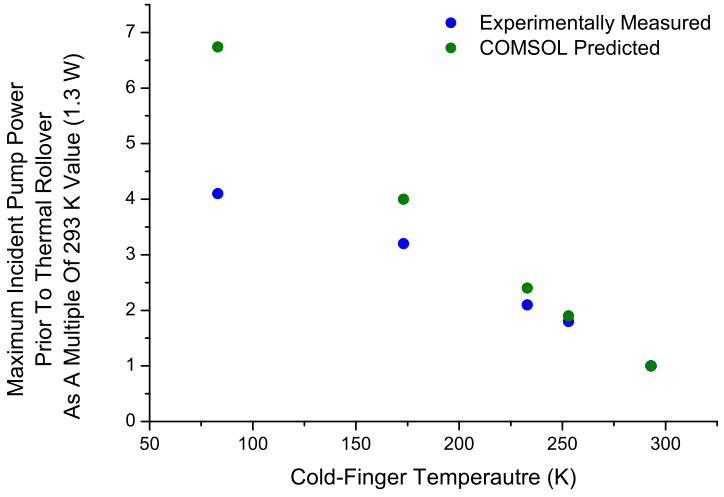

Figure 3.30: A comparison between the experimentally measured maximum incident pump power tolerated by the gain chip prior to the onset of thermal rollover and the value predicted by the FEA model: these quantities are plotted in multiples of the room temperature value (1.3 W at 293 K) and against cold-finger temperature.

Figure 3.30 shows that the FEA model over-predicts the amount of pump power that the gain chip is able to tolerate and that the disagreement between the experimental and calculated data increases with reducing cold-finger temperature. For temperatures above 150 K the FEA model agrees with the experimental data to within a tolerance of 25 %. Below this temperature the calculated and measured data quickly diverge. This disagreement is thought to be due in part to the FEA model's inability to account for both the heat-load generated by the non-radiative Auger recombination mechanism and the temperature dependent trapping efficiency of the quantum wells. By taking into account the data extracted from figure 3.28 this disagreement could also be due to the model neglecting the heat-rise brought about by the increase in non-radiative defect recombinations occuring as the gain chip succumbs to mechanical failure. A FEA thermally-induced-stress model of the gain chip could be constructed in order to test this idea.

3.4.6 Cryogenic CW-VECSEL Performance Summary

In this section a VECSEL has been reported and characterised that utilised a gain chip cooled to cryogenic temperatures. The VECSEL gain chip used a $4.5\lambda/2$, antiresonant design containing 4, 8 nm thick, $In_{0.2}Ga_{0.8}As$ quantum wells. The gain chip was cooled using a liquid nitrogen cold-finger cryostat; the vacuum space of which housed the entire VECSEL cavity.

By reducing the temperature of the cold-finger from 293 to 83 K the VECSEL exhibited a 53 % $\pm$ 10 % reduction in the incident pump power required to reach laser-threshold, a 4-fold increase in incident pump power tolerated prior to the onset of thermal rollover, and an increase in output power from 143 mW to 1540 mW: an increase of more than an order of magnitude. Over this temperature range the slope efficiency of the VECSEL increased 3-fold, from 10 % to 30.5 %.

The output power of the cryogenically cooled VECSEL is suspected to be limited by the onset of mechanical failure due to differential contraction brought about by the thermal gradient between the pumped front surface and cooled back surface of the gain chip. This suggestion is supported by the experimental data and the construction of thermally-induced-stress FEA model would help confirm this. The performance of a VECSEL utilising a cryogenically cooled gain chip could therefore be extended further by using a gain chip that is stressed by an appropriate amount in the opposite drection at room temperature: this would ensure that the net-stress placed on the gain chip would be 0 when operated at cryogenic temperatures and pumped with intense optical fields.

3.5 A Cryogenic Modelocked VECSEL

In this section a modelocked VECSEL utilising a cryogenically cooled gain chip is reported. The gain chip was cooled using the liquid nitrogen cold-finger cryostat presented in section 3.2. Section 3.5.1 details the selection of the gain and SESAM structures and the VECSEL design. Section 3.5.2 then reports the measured VECSEL performance.

3.5.1 Laser Design

Due to both the financial and time costs that are associated with designing, growing, and refining new structures it was decided that the cryogenic modelocked VECSEL should be constructed using pre-existing gain and SESAM structures. The choice of gain and SESAM structures with which to build this cryogenically cooled, modelocked VECSEL was further limited because, whilst the absorption profile of the SESAM would remain constant, the emission of the gain chip would be affected by the cold-finger temperature: a 66 nm shift in the emission wavelength of the gain chip was expected when cooling the gain chip from room temperature to 80 K. The SESAM structure with the shortest wavelength absorption operated at a wavelength of 1000 nm and therefore, in order to ensure that the gain chip emission was coincident in wavelength with the SESAM absorbtion, a gain chip with a room temperature emission wavelength of 1066 nm was required.

The longest wavelength gain structure available was A4250: a $7\lambda/2$, antiresonant structure containing 6, 8 nm thick $In_{0.25}Ga_{0.75}As$ quantum wells. At room temperature this gain structure operates at a wavelength around 1050 nm. A schematic of the gain structure is provided below in figure 3.31.

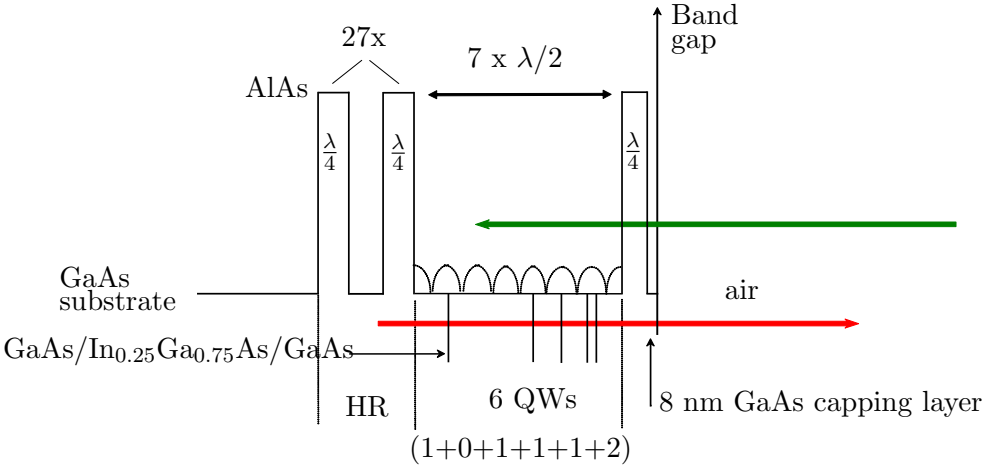

Figure 3.31: Schematic of A4250: the gain structure used in the cryogenic modelocked VECSEL

This gain structure was paired with V628: a surface recombination SESAM structure containing a single 8 nm thick $In_{0.2}Ga_{0.8}As$ quantum well, set at a depth of 2 nm from the surface. The SESAM has a design wavelength of 1000 nm. A schematic of the SESAM structure is provided below in figure 3.32.

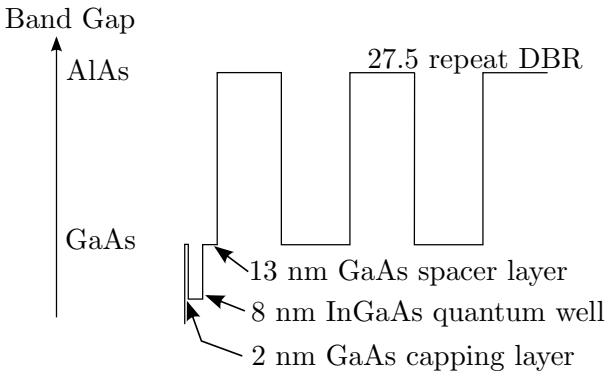

Figure 3.32: Schematic of V628: the SESAM structure used in the cryogenic modelocked VECSEL

A 0.97 GHz, 'z'-cavity geometry was assembled in the vacuum chamber using the gain and SESAM structures, a 0.3 % transmission, 75 mm radius of curvature output coupler and a 25 mm radius of curvature fold mirror. The output coupler was ≈ 73 mm from the gain chip and the SESAM was ≈ 15 mm from the fold mirror. A diagram of the cavity is given below in figure 3.33. The gain structure was bonded with silver paint to the cold-finger and pumped with an 808 nm fibre-coupled diode laser emitting up to 4 W of light focused to a 60 μm radius spot (the 40 W diode laser previously used was unavailable due to it being used in another experiment elsewhere in the research group).

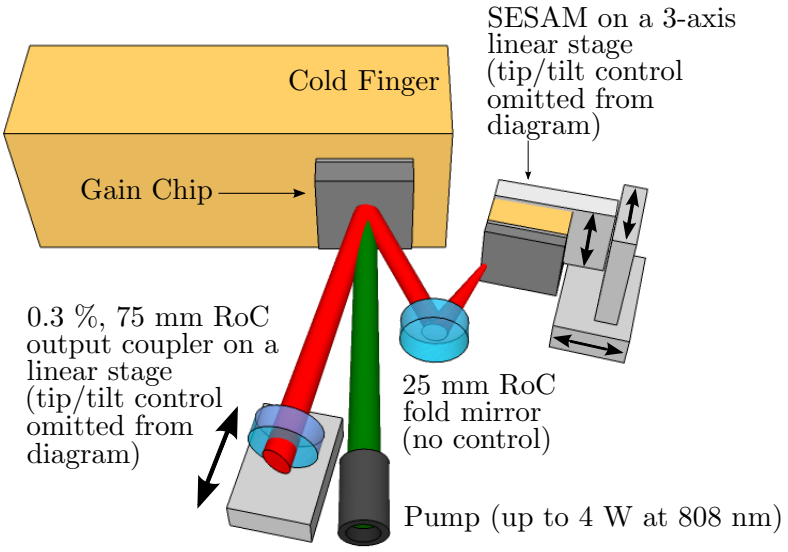

Figure 3.33: Schematic of the cryogenic modelocked VECSEL. The o/c was ≈ 73 mm from the gain chip and the SESAM was ≈ 15 mm from the fold mirror.

Due to the wavelength offset of the gain and SESAM structures it was not possible to align a working VECSEL at room temperature. The VECSEL was therefore sealed into the cryostat, the vacuum chamber evacuated and the remaining moisture drawn onto the dewar. The cold-finger was then cooled to a temperature of 150 K corresponding to a calculated wavelength shift of 45 nm. Consequently a gain emission wavelength of approximately 1005 nm was achieved. At this temperature the z-cavity was aligned using the motorised stages and mirror mounts. The temperature of the cold-finger was then further reduced and the cavity optimised until modelocked operation was observed.

3.5.2 Laser Performance

The VECSEL beam was collimated within the vacuum space, guided out of the cryostat and split between a Femtochrome FR-103XL autocorrelator, a Perkin-Elmer 0.275 m grating spectrometer and a Newport 1434, 25 GHz fast photodiode connected to an Advantest R3267 RF analyser. Modelocking was observed for a cold-finger temperature of 143 K and an incident pump power of 3.6 W: an autocorrelation, optical spectrum and RF spectrum are given in figure 3.34. The third harmonic was recorded as the first harmonic was obscured by a noise signal arising due to photodiode damage and, in a moment of madness, the second temporarily forgotten about by the author.

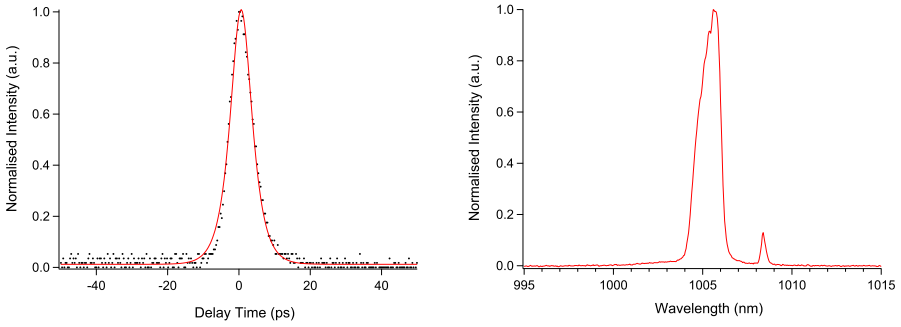

(a) Autocorrelation

(b) Optical Spectrum

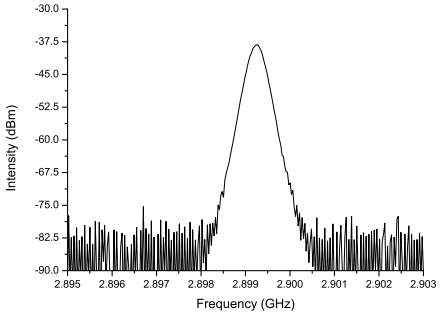

(c) RF Spectrum: 3^{rd} Harmonic

Figure 3.34: Summarised performance of a modelocked VECSEL utilising a gain chip cooled by a cold-finger held at 143 K. The VECSEL exhibited a pulse duration of 4.7 ps (a), a wavelength of 1006 nm (b) and a fundamental pulse repetition rate of 0.966 GHz (c). The average output power of the VECSEL was 22.4 mW for an incident pump power of 3.6 W.

The modelocked VECSEL emitted 4.7 ps pulses at a pulse repetition rate of 0.966 GHz and in a $TEM_{0,0}$ diffraction limited beam. The VECSEL wavelength was around 1006 nm and the average power was 22.4 mW. The emitted pulses therefore had a peak power of 4.6 W and were approximately 6-times the transform limit for a $sech^2$ pulse.

The observed modelocked behaviour was stable for no more than 10 seconds. This was most probably due to the alignment of the VECSEL components being disturbed by the mechanical vibrations originating at the vacuum pump and being transmitted to the cryostat structure through the connectors and tubing. Because the cryostat was not able to hold a static vacuum it was not possible to shut-down or disconnect the turbo-molecular pump and so the stability of the modelocked behaviour could not be improved. By reoptimsing the cavity geometry using the computer controlled stages modelocked operation could be recovered.

The low average output power and slope efficiency are expected to be due, at least in part, to the high indium concentration in the gain structure: previous work undertaken using this gain structure has shown that the high indium concentration causes dark-line defects to form more rapidly in this crystal structure when compared to gain structures with a lower indium concentration. In addition to this, because the structure was grown through MBE, no strain compensation is included within the gain chip and again, this causes dark-line defects to form more rapidly. It is assumed that these two structural decay mechanisms will be exacerbated by simultaneously cooling the gain chip to cryogenic temperatures and pumping it with intense optical fields.

In order to counter this mechanism a gain chip could be designed that is stressed by an appropriate amount in the opposite direction at room temperature. This would ensure that the net-stress placed on the gain chip would be 0 when operated at cryogenic temperatures and pumped with intense optical fields.

3.6 Chapter Conclusions

Prior to this work being undertaken the coldest temperature at which a VECSEL gain chip had been operated was approximately 248 K. This chapter has shown that it is possible to operate a VECSEL with a gain chip held at cryogenic temperatures. By doing this the predicted improvements in VECSEL performance, as set out in chapter 2, are all qualitatively observed.

This chapter began by presenting the design of a cryostat with a vacuum space large enough to house an entire VECSEL cavity. The cryostat used a liquid nitrogen cold-finger design and was built in the Mechanical Workshop by Mr Damon Grimsey. I am indebted to his skill and hard work.

In section 3.3 the DBR-shift method, introduced in chapter 2, was applied to a gain chip cooled using the liquid nitrogen cold-finger cryostat. For a cold-finger temperature of 80 K the rise in active region temperature, measured with respect to the incident pump power, was calculated to be 22.6 x $10^{-3}\pm$ 0.2 x 10^{-3} K/mW. Qualitative agreement between this experimental data and the FEA model was achieved by modifying the FEA model to include both a variable that accounted for the change in DBR reflectivity, at the pump wavelength, and as a function of temperature and an expression that accounted for the absorption of the pump light reflected by the DBR as it passed through the active region for a second time. This modified FEA model agreed quantitatively with the experimentally measured data to within a calculated mean error of 19 K (17 %): the standard deviation on the error is calculated to be 13 K (8 %).

By combining the modified FEA model with the data obtained using the DBR-shift method, it was calculated that a gain chip, bonded to a cold-finger maintained at 83 K, would tolerate between 10 and 12 W of incident pump power prior to thermal rollover. Due to the limitations of the model (discussed on page 47) this value was expected to be an over-estimate and this was shown to be the case in figure 3.30. Whilst the accuracy of the model could be improved through further modification of macroscopic parameters (a gaussian pump profile for example) the model's failure to include non-radiative recombination will probably always dominate the innacuracy. To include this mechanism a full microscopic model of the gain chip would be needed and therefore, because the FEA model was created in order to give an approximate insight into the benefits of operating a VECSEL gain chip at cryogenic temperatures, and because microscopic modelling of the gain chip is beyond the scope of this reseach, the FEA model in its current form is to be considered complete.

Section 3.4 reported a CW-VECSEL utilising a cryogenically cooled gain chip: the gain chip used a $4.5\lambda/2$, antiresonant active region contianing 4, 8 nm thick, $In_{0.2}Ga_{0.8}As$ quantum wells. By reducing the temperature of the cold-finger from 293 to 83 K the VECSEL exhibited a 53 % $\pm$ 10 % reduction in the incident pump power required to reach laser-threshold, a 4-fold increase in incident pump power tolerated prior to the onset of thermal rollover, and an increase in output power from 143 mW to 1540 mW: an increase of more than an order of magnitude. Over this temperature range the slope efficiency of the VECSEL increased 3-fold, from 10 % to 30.5 %. The output power of the VECSEL is suspected to be limited by the gain chip undergoing thermal-stress-induced mechanical failure. This failure probably results from the differential contraction associated with the temperature gradient that arises from the pumped front surface, and the cooled back surface, of the gain chip. This suggestion is supported by the experimental data.

The chapter concluded by reporting a modelocked VECSEL utilising a cryogenically cooled gain chip. Modelocked behaviour was observed for a cold-finger temperature of 143 K and an incident pump power of 3.6 W. The temperature was constrained by

the need to align the emission wavelength of the gain chip to the absorption profile of the SESAM. Under these conditions the VECSEL emitted 4.7 ps pulses at a pulse repetition rate of 0.966 GHz and in a diffraction-limited $TEM_{0,0}$ beam around 1006 nm. The average power of the VECSEL was 22.4 mW corresponding to a peak power of 4.6 W. The pulses were approximately 6-times the transform limit for a $sech^2$ pulse.

3.6.1 Future Research

Having shown that cryogenic-cooling of the gain chip reduces laser threshold, increases pump power tolerance and improves slope efficiency it is the author's hope that this body of work will inspire further research and development in the field of cryogenically cooled VECSELs. This future work could include the following ideas.

Firstly a FEA thermal-stress model of the gain chip could be developed. This would help to inform the design of future gain chips and could, for example, lead to structures that are stressed by an appropriate amount in the opposite direction at room temperature and so operate with a net-stress of zero when cryogenically cooled. Doing this would most probably extend the life of the gain chip.

Secondly an investigation should be undertaken into the thermal properties of the bond between the gain chip and the cold finger. All the gain chips used in this work were bonded to the cold finger using a silver paint that had unknown thermal properties when operated within the cryogenic regime. By studying the effect of cryogenic temperatures on both silver paint and other bonding materials (indium for example) a bond between the gain chip and cold-figner with lower thermal impedence may be obtained. This would help transport heat out of the gain chip more efficiently leading to lower active region temperatures and the use of higher pump powers.

Finally a measurement of the gain profile as a function of cold-finger temperature would both give insight into the temperature dependent carrier dynamics of the active region and help to inform the design of future gain chips. For example if cryogenic temperatures are seen to narrow the gain spectrum this would help in the design of cryogenic modelocked lasers. This measurement would involve illuminating the gain chip with a wavelength tuneable, modelocked laser and measuring the single pass gain as a function of probe wavelength and gain temperature.

Whilst the application of cryogenic cooling to solid-state lasers has resulted in significant improvements in solid-state laser performance (section 2.1) this method of thermal regulation has, due to its relative complexity, been largely confined to the laboratory environment. This chapter has shown that VECSEL performance can also be greatly improved through cryogenic cooling and, with the on-going development of micro cryogenic coolers [75], this could make compact, cryogenically cooled VECSELs a very real and attractive prospect.

Chapter 4

A Wavelength-Tuneable Modelocked-VECSEL For Bright, Heralded Single-Photon Generation

4.1 Introduction

With the invention of the personal computer came the 'Age of Information'. Fifty years later the average person can now afford to create, control, receive and transmit an apparently limitless amount of data. The advances in technology that are facilitating this brave new world are underpinned by physics rooted in the classical domain and with the demand for greater processing powers and faster computation continuing unabated, this approach is now being stretched to breaking point. A second information age, underpinned by quantum mechanics, could provide the solution. This new framework would be underpinned not by the 'bit' but by the quantum-bit or 'qubit': some two-level quantum system that exists in a linear superposition of its two eigenstates. Mathematically a qubit is represented as:

$$|\psi\rangle = \alpha|0\rangle + \beta|1\rangle. \tag{4.1}$$

For a two-level quantum system to be considered as a qubit candidate it must fulfill four requirements: the initial state of the qubit must be easily set, subsequent operations after initialisation must be able to alter the state without completely destroying it, the qubit must interact strongly with other qubits to permit entanglement and the qubit must interact weakly with the environment to preserve its coherence. Suggested candidates

that meet these criteria include electron and nuclear spins in solid-state crystals [82], quantised loops of magnetic fields in superconducting materials, and electrodynamically trapped ions [83]. The implementation of these qubit schemes is difficult as they typically need temperatures on the order of mK to 10s of Kelvin, and / or magnetic fields on the order of 0.5 to 10 T.

The single photon is another qubit candidate and is considered by many to be close to ideal [84]. At room temperature and pressure it can be readily encoded and controlled through the use of already commonplace polarisation-controlling optical components, it can be confined within an optical fibre thus making the transmission and distribution of single photon qubits through a data network possible and, due to the wave-like nature of the single photon, those quantum computing algorithms that rely on inteference effects can be readily implemented. The single photon cubit therefore increases the convenience and reduces both the complexity and the financial cost of the system.

A common technique for obtaining single photons is to use a high-intensity laser pulse in a non-linear medium to generate a photon pair onto which a heralding measurement can be performed. The highest-performance sources are usually pumped by Ti:Sapphire oscillators [52, 53, 54, 85, 86, 87] however this places them orders of magnitude higher in both complexity and cost than the attenuated laser sources typically used in commercially available quantum technologies. Furthermore, the repetition rate of these lasers, typically in the region of 80 MHz, places a limit on the rate at which high-quality photon pairs can be delivered by a single source [88]. These factors present significant obstacles to implementing real-world photonic quantum-enhanced technologies.

A wavelength-tuneable, modelocked VECSEL exhibits a number of properties that make it an attractive choice as a pair generation source. The GHz pulse repetition rate should give a higher pair generation rate than a typical 80 MHz laser system, the wavelength flexibility should allow phase-matching to occur between the VECSEL and the non-linear medium for a reduced manufacuring tolerance of the non-linear medium, and the excellent beam quality should increase the coupling efficiency between the VECSEL and the non-linear medium.

This chapter reports on the development of a wavelength-tuneable, modelocked VECSEL suitable for bright, heralded single photon generation. Section 4.2 gives a theoretical overview of the four-wave mixing process and then details a typical experiment and the experimental considerations that are commonly taken into account. The development of a VECSEL source is then reported. A proof of concept, low power, wavelength tuneable, modelocked VECSEL, a proof of concept, high power, wavelength tuneable, modelocked VECSEL and a high power, thermally managed, wavelength tuneable, modelocked VECSEL are reported in sections 4.3.1, 4.3.2 and 4.3.3 respectively. The chapter concludes by reporting on the implementation of the third VECSEL as a pump laser in a heralded single-photon experiment: this is done in section 4.4.

4.2 Generating Single Photons With Four Wave Mixing

This section will explain how four-wave mixing can be utilised to achieve single photon generation. Subsection 4.2.1 will provide a brief theoretical guide to single photon generation using four-wave mixing. An overview of the single photon source built and operated by Dr Peter Mosley and Mr Jamie Francis-Jones at the University of Bath will then be given: it is this system into which the VECSEL will be integrated. Finally subsection 4.2.3 will discuss the considerations one needs to make when choosing a pump laser and why the VECSEL makes an excellent choice. Figures 4.2.3 and 4.4 were computed by Jamie.

4.2.1 Single Photons Through Four Wave Mixing (Theoretical)

Four Wave Mixing (FWM) is a parametric process that arises through the third-order non-linearity χ^3 [89]. The process couples two degenerate pump fields ($\omega_1 = \omega_2 = \omega_\mathrm{p}$) to a pair of daughter fields termed the signal ($\omega_3 = \omega_\mathrm{s}$) and idler ($\omega_4 = \omega_\mathrm{i}$). The signal and idler fields are detuned either side of the pump by an equal amount in accordance with energy conservation:

$$\omega_\mathrm{p} - \omega_\mathrm{s} = \omega_\mathrm{i} - \omega_\mathrm{p} = \Omega. \tag{4.2}$$

A short-pulse of electromagnetic field, propagating along the z-axis of a fused-silica optical fibre, will have a nonlinear polarisation component given by

$$P(\underline{\mathrm{r}}, t)^{(i)}_{NL} = \epsilon_0 \sum_{j,k,l} \sum_{m,n,q} \chi^{(3)}_{i,j,k,l} \underline{E}^{(j)}(\omega_m : \underline{\mathrm{r}}, t) \underline{E}^{(k)}(\omega_n : \underline{\mathrm{r}}, t) \underline{E}^{(l)}(\omega_q : \underline{\mathrm{r}}, t) \tag{4.3}$$

where the susceptibility is treated as a tensor and the indices i, j, k and l each run over the two transverse cartesian axes x and y and m, n and q each run over the frequencies ω_1, ω_2 and ω_3. Due to the symmetrical crystal structure of the optical fibre, the third order susceptibility will be the same along all directions

$$\chi^{(3)}_{x,x,x,x} = \chi^{(3)}_{y,y,y,y} = \chi^{(3)}_{z,z,z,z} = \chi^{(3)} \tag{4.4}$$

and so the susceptibility can be treated as a scalar. By expanding equation 4.3 a term responsible for FWM is obtained:

$$E_4(\omega_4 : \omega_1 + \omega_2 - \omega_3) = \frac{P_4(\omega_4)}{\epsilon_0 \chi^{(3)}} = 6 E_1 E_2 E_3^* e^{i(\delta\kappa z - \delta\omega t)} \tag{4.5}$$

where

$$\delta\kappa = k(\omega_1) + k(\omega_2) - k(\omega_3) - k(\omega_4) - 2\gamma P \tag{4.6}$$

and

$$\delta\omega = \omega_1 + \omega_2 - \omega_3 - \omega_4. \tag{4.7}$$

$\delta\kappa$ is the phase-mismatch, $2\gamma P$ is the self-phase modulation (SPM) due to the pump power and $\delta\omega$ is the frequency mismatch between the daughter frequencies ω_3 and ω_4. A result similar to equation 4.5 can be obtained by deriving the evolution of a field for ω_3 and through these two coupled equations the evolution of two new daughter fields can be described. The long wavelength daughter field is termed the idler field and the short wavelength field is termed the signal field.

At each point in the FWM medium there will be a localised fixed phase relationship between the pump field and the daughter fields. Careful control of the medium's dispersion profile is therefore essential to ensure that these local fields add together constructively as this will allow the daughter fields to experience appreciable growth [90, 91]. When this occurs $\delta\kappa$ in equation 4.6 will equal 0 and the fields involved are said to be phase-matched.

Due to the probabilistic nature of the emission process the resultant signal and idler fields will propagate as some number of coincident photons. This daughter field emission can be written as a linear superposition of photon pair number occupations

$$|\Psi\rangle = |0,0\rangle + p|1,1\rangle + p^2|2,2\rangle + p^3|3,3\rangle + ..., \tag{4.8}$$

where p is the probability of producing a photon pair. A single photon source is consequently achieved by spectrally splitting the $|1,1\rangle$ coincident pairs as they are emitted from the medium and then, by detecting one photon in the pair, the presence of the companion will be *heralded* [92].

4.2.2 Experimental Generation Of Single Photons Through FWM

A schematic of the single photon source built and operated by Dr Peter Mosley and Mr Jamie Francis-Jones at the University of Bath is shown on the following page in figure 4.1. The system comprises three constituent parts: a laser source is used to provide the degenerate pump field, a length of Photonic Crystal Fibre (PCF) is used as the non-linear medium and finally a detection system is used to collect and measure the arrival of coincident photon pairs.

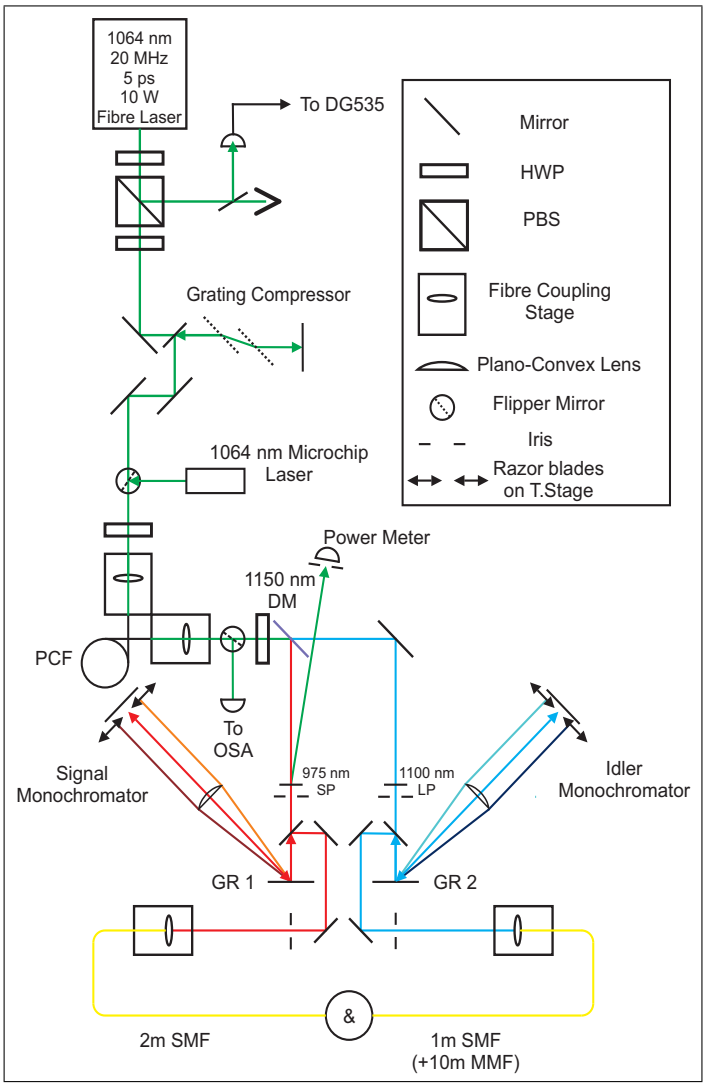

Figure 4.1: A schematic of the single photon source built and operated by Dr Peter Mosley and Mr Jamie Francis-Jones at the University of Bath. A 10-W, 5 ps, 20-MHz fibre laser emitting at 1064 nm is used to pump a length of PCF. The resultant signal and idler fields are spectrally split and each is passed through a monochromator and then coupled into an avalanche photodiode. Figure reproduced from [93]

4.2.2.1 The Laser Source

Many different types of laser can be used to achieve FWM in PCF however a high-power pulsed laser is a typical choice. The high power allows access to the χ^3 regime and ensures a high photon-pair generation rate. The pulsed operation ensures that the daughter photons are produced in well defined time bins. A perfect source would generate one photon-pair per pump pulse and therefore care must be taken to limit the value of p in equation 4.8 to $<< 1$. The pump wavelength must match the precisely required PCF dispersion values in order to ensure that constructive propagation of the signal and idler fields occur.

4.2.2.2 The Photonic Crystal Fibre (PCF)

Photonic Crystal Fibres (PCF) are a class of optical fibre that use a periodic array of air holes in a silica background as a cladding structure [94]. It exhibits χ^3 nonlinearity and has a refractive index composed of two parts: an inherent material contribution and a waveguide contribution. By varying the diameter (d) and the separation (Λ) of the air holes, the waveguide contribution to the refractive index can be controlled. This in turn allows some control over the frequency dependence of the phase- and group-velocities and therefore control over the frequencies that are phasematched in the FWM interaction. The laser source is coupled into the PCF using a focussing microscope objective.

4.2.2.3 The Detection System

The PCF emission is collimated and then spectrally filtered in order to remove any remaining pump laser light. The daughter fields are then spectrally separated and each is passed through a grating monochromator in order to both determine the wavelength of the light and to remove any unwanted spectral noise. Finally each daughter field is guided through a focussing microscope objective and coupled into a length of single-mode fibre that terminates with a connection to a single photon detector.

The lengths of the single-mode fibres are not equal and are chosen to ensure that one photon in the pair will be detected first. This detection event will then be used to gate the second single photon detector whose corresponding photon will have been delayed using the longer length of fibre. Upon detection of a photon, each single photon detector will output an electrical signal. These signals are carried through coaxial cable to a coincidence detector. The lengths of coaxial cable are chosen in order to undo the delay imposed by the unequal lengths of single-mode fibre. A coincident pair is recorded by observing when the two single photon detector signals arrive simultaneously and this coincidence rate yields the pair generation rate. The *heralding* measurement is undertaken in order to remove the zero photon occupation eigenstate from the state-vector and to distinguish coincident pairs from random, uncorrelated photon noise.

An 'accidental coincidence' may be detected when an uncorrelated photon pair, for example photons produced on different laser pulses, arrive at the detectors together. The rate of accidental coincidences is determined by delaying the photon in one arm so that it coincides with the emission from the subsequent laser pulse. The true rate of coincidences (and therefore of heralded single photons) is then determined by subtracting the accidentals rate from the coincidence rate. Observing a coincidence to accidentals ratio (CAR) of greater than 1 implies that the coincidences observed occur at a rate greater than that of random chance and are therefore due to photons correlated between the two arms.

4.2.3 Laser Source Considerations

An ideal single photon system would emit a photon in a pure quantum state and at a wavelength of 1550 nm as often as possible. Although many different types of laser can generate FWM in PCF, the signal and idler spectral properties, state purity and generation rate are all influenced by the source laser so it is essential to choose carefully. As an example a PCF dispersion profile and the corresponding phasematched wavelengths are plotted against pump wavelength in figure 4.2(a) and 4.2(b) respectively.

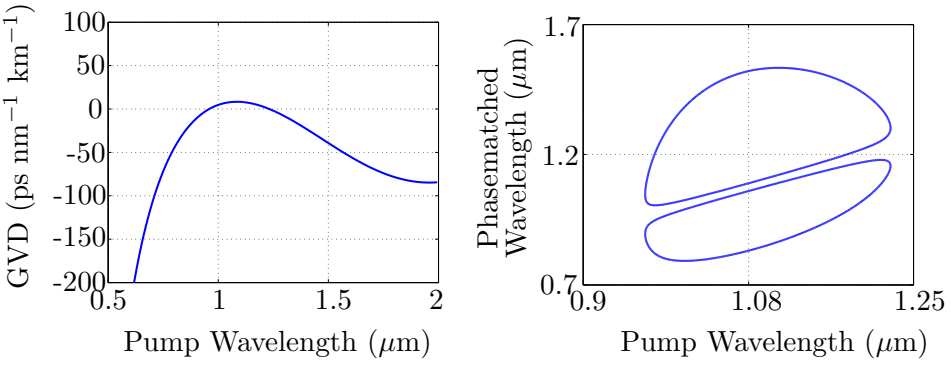

(a) (b)

Figure 4.2: The group-velocity dispersion (GVD) (a) and the phasematched wavelengths (b) plotted as a function of pump wavelength for a PCF with an air hole spacing of 1.6 μm and an air hole diameter to hole spacing ratio of 0.4.

Historically single photon systems have utilised a Ti:Sapphire oscillator laser source: the high power produces a high photon-pair generation rate and the ability to tune the wavelength of the source results in excellent phasematching [52, 95, 96]. There are however disadvantages to this approach. The large financial cost, the high level of mechanical complexity and the relatively large footprint of the laser result in a single photon system that would be unfeasable for any real-world, commercial application.

Another unwanted consequence of using a high power source is the resultant increase in the rate of double and higher-order pair emission. This occurs due to p in equation 4.8 scaling quadratically with pump power and can be mitigated by temporal multiplexing: dividing the power of the pump laser into a larger number of pulses per second [97]. As the average power is kept constant the same total number of photon pairs will be generated per second, but with a reduced probability of finding more than one pair in the same pulse. A GHz repetition rate laser therefore has a significant advantage per mW average power in terms of the ratio of multiple-to-single pair emission events when compared to a typical 80-MHz, Ti:Sapphire pump laser.

In order to reduce the cost and complexity imposed by a Ti:Sapphire laser source, fixed wavelength, neodymium based lasers have been used in single photon systems [98]. This is a simpler and lower-cost solution however the fixed wavelength requires the PCF manufacturing tolerances to become more stringent in order to match particular energy and momentum phase-matching conditions.

4.2.4 The Advantages Of A VECSEL Source

A wavelength-tuneable, modelocked VECSEL, shown schematically in figure 4.3, would be highly suited for the generation of heralded single photons. In comparison to a Ti:Sapphire oscillator it is a more compact, inexpensive and mechanically simpler source.

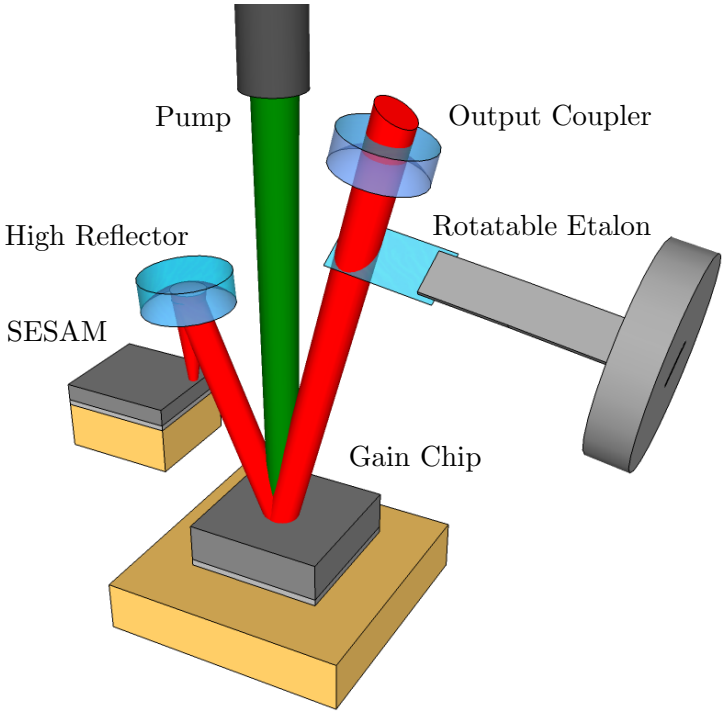

Figure 4.3: A schematic of a wavelength-tuneable, modelocked VECSEL. By rotating the etalon, the etalon transmission function will be shifted in wavelength therefore selecting the laser emission wavelength.

As discussed in section 1.1.3, the freestanding output coupler ensures excellent beam quality ($M^2 \approx 1.0$). Consequently a high coupling efficiency between the VECSEL and the PCF is expected and this will help maximise the efficiency of the system.

The short carrier lifetime, low gain saturation fluence and relatively short cavity length result in a pulse frequency that is typically on the order of GHz. Using the argument given in the previous section, this high repetition rate should result in a reduction of the higher-order pair generation probability and consequently this will lead to a greater number of qubits generated per second for a given level of acceptable error.

A final benefit is that the VECSEL wavelength can be selected by the choice of the semiconductor gain material, the operating temperature and by incorporating an intracavity etalon in to the external cavity [99]. This wavelength selectivity allows particular values of the fibre dispersion profile to be accessed and consequently the properties of both the photon pairs and heralded single photons can be controlled through this quantum state engineering [100].

The one-pair component of the state that results from FWM can be written

$$|1_s, 1_i\rangle = |\psi(\omega_s, \omega_i)\rangle = \int_{-\infty}^{\infty} d\omega_s d\omega_i f(\omega_s, \omega_i)|\omega_s, \omega_i\rangle, \tag{4.9}$$

where $f(\omega_s, \omega_i)$ is the two-photon amplitude or joint spectrum. As the photons are created together in a parametric process subject to energy and momentum conservation, this amplitude contains correlation between the signal and idler in both the frequency and time domains. Detecting each photon consequently yields distinguishing information about its twin, projecting the remaining heralded single photons into mixed quantum states that are largely useless for information-processing tasks.

In order to herald single photons in pure quantum states the photon-pair amplitude must be uncorrelated [101]. Producing an uncorrelated two-photon state is not trivial, and there are two critical requirements: sufficient pump bandwidth to ensure that energy conservation does not dominate the joint state [102, 95, 103, 104, 105] and control of the material dispersion.

Figure 4.4 shows how, for the PCF dispersion profile given in figure 4.2(a), the probability density of the two photon state can be altered from a postively-correlated state to an uncorrelated state by using a pump wavelength of 1.064 μm and 1.1 μm respectively (this is equivalent to using a fixed pump wavelength and increasing the GVD of the PCF by 1.2 % from 8.1 ps nm^{-1}Km^{-1} to 8.2 ps nm^{-1}Km^{-1}).

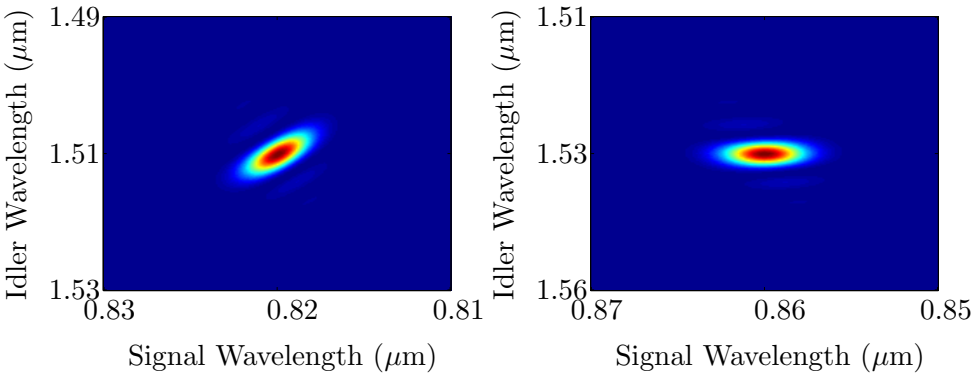

Figure 4.4: A positively correlated (a) and an uncorrelated (b) two-photon probability density calculated using the PCF dispersion profile given in figure 4.2(a) and for a pump wavelength of 1.064 μm and 1.1 μm respectively.

A heralded single photon system that uses a fixed wavelength pump laser requires the dispersion profile of the fibre to be precisely matched to this pump wavelength. This in turn requires fine control of the fibre manufacturing process and is a major challenge. A wavelength tuneable VECSEL source is beneficial as changes in the dispersion profile that result from small fabrication errors in the PCF structure can be compensated for by altering the pump wavelength.

4.3 The Development of A Wavelength-Tuneable, Modelocked VECSEL

This section will detail the development of a wavelength-tuneable, modelocked VECSEL suitable for generating heralded single photons through FWM in PCF. A proof of concept, low power, wavelength-tuneable, modelocked VECSEL will be reported in subsection 4.3.1 and a high power, wavelength-tuneable, modelocked VECSEL will be reported in subsection 4.3.2. The section will conclude by reporting a stable, high power, wavelength-tuneable, modelocked VECSEL.

4.3.1 A Proof Of Concept, Low Power, Wavelength-Tuneable, Modelocked VECSEL Source

4.3.1.1 Laser Design

In order to determine whether an intracavity etalon could be used to select the emission wavelength of a VECSEL without disturbing the modelocked operation, a low power, modelocked VECSEL source was built and characterised.

The VECSEL used an antiresonant gain chip with a design wavelength of 1040 nm. The gain chip was grown by MOCVD and comprises a 500 μm thick GaAs substrate, a 27.5 pair AlAs/GaAs distributed Bragg reflector (DBR), a $7\lambda/2$ thick GaAs active region containing 6 $GaAsP_{0.06}$/InGaAs/$GaAsP_{0.06}$ quantum wells, a $1.45\lambda/4$ thick AlAs window layer and an 8 nm GaAs capping layer.

The gain chip was mounted using silver paint onto the surface of a temperature controlled copper heat-sink and held at -8 °C. A stream of nitrogen gas was blown over the face of the gain chip to ensure that the surface was kept free of condensation. The gain chip was pumped with a fibre-coupled diode laser emitting 1.1 W of 830 nm light focussed into a 60 μm radius spot.

The gain chip was paired with a SESAM structure consisting of a 500 μm thick GaAs substrate, a 27.5 pair GaAs/AlAs DBR, a 13.5 nm GaAs spacer layer, a single InGaAs/-GaAs quantum well optimised for absorption at 1025 nm and a 2 nm GaAs capping layer. The SESAM schematic given in figure 3.32 is also representative of this structure. A second flow of nitrogen gas was placed over the face of the SESAM as previous work indicated that this improves the long term stability of the SESAM.

A 0.3 % partially transmitting mirror with a radius of curvature (ROC) of 50 mm was used as an output coupler and the laser mode was focused onto the SESAM by a high reflector with a ROC of 25 mm. This resulted in a 20 μm radius spot on the SESAM. The VECSEL used a 'Z' cavity geometry and a schematic is shown in figure 4.3.

An intracavity etalon acts as a spectral filter. It passes those wavelengths that are coincident with the etalon resonance and, by rotating the etalon, this transmission function, and consequently the laser emission, will be shifted in wavelength (appendix A).

This work uses an uncoated, 25 μm etalon constructed from fused-silica. The etalon's free spectral range (FSR) and finesse were calculated to be 14 nm and 1.75 respectively at normal incidence. The calculated dependency between the resonant wavelength of the etalon and the etalon's angle from normal incidence is given in figure 4.5. The x-axis range was chosen as Brewster's angle for this etalon is $\approx 53\ ^\circ$ from normal incidence.

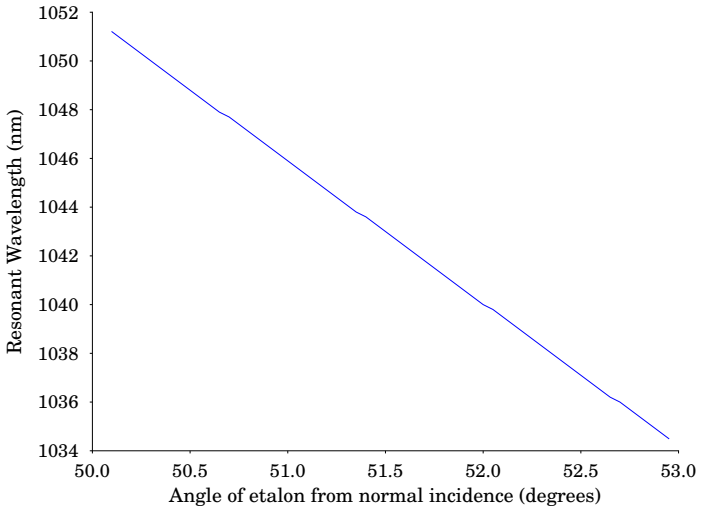

Figure 4.5: The calculated dependency between the resonant wavelength of an uncoated, 25 m thick, fused silica etalon and the angle that it makes to normal incidence. The calculation assumes an infinite plane wave approximation, a perfectly parallel sided etalon and that the etalon is illuminated exclusively by light that is polarised in the etalon's plane of rotation

The etalon was mounted to the end of a metal rod which was in turn clamped to a motorised rotation stage. The etalon was then placed into the VECSEL cavity between the output coupler and the gain chip and oriented at Brewster's angle with respect to the s-polarised laser mode. This was done in order to minimise the insertion loss.

4.3.1.2 Laser Results

As the intracavity etalon was rotated, the VECSEL tuned continuously over a wavelength range of 14.5 nm around a centre wavelength of 1040.3 nm. Over this tuning range a stable modelocked pulse train was maintained with pulse durations between 2.3 and 3.4 ps. The RF spectrum of the laser exhibited a fundamental repetition rate of 0.95 GHz. Figure 4.6(a) shows the optical spectrum and figure 4.6(b) shows the corresponding intensity autocorrelation of the laser for six orientations of the etalon. These measurements were made using a Perkin-Elmer 0.275 m grating spectrometer and a Femtochrome FR-103XL autocorrelator respectively.

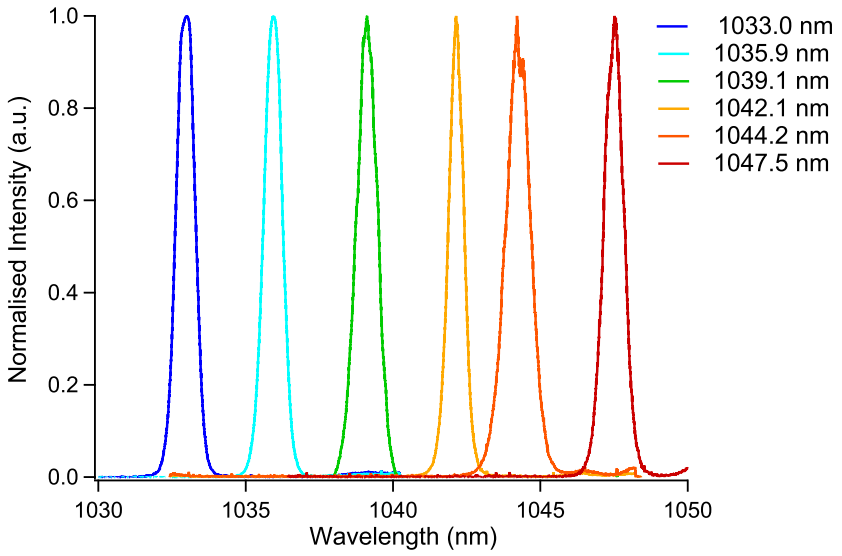

(a)

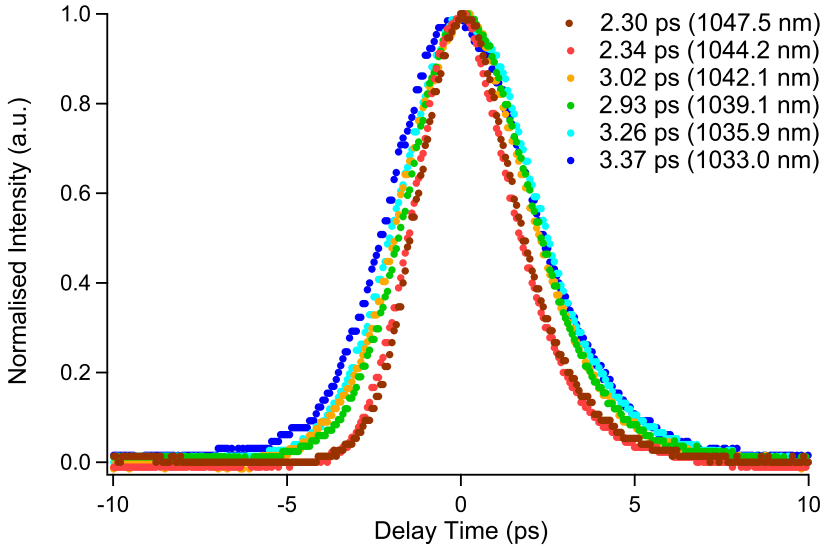

(b)

Figure 4.6: Optical spectra (a) and corresponding autocorrelations (b) for six orientations of the etalon demonstrating the wavelength tuning capabilities of the laser. A maximum peak power of 4.3 W was obtained.

Over the full tuning range the optical spectrum FWHM bandwidth of the laser varied from 0.66 to 1.3 nm and the emitted pulses varied between 1.2 and 1.9 times the transform limit for a Gaussian pulse. Due to misalignment of the autocorrelator a slight asymmetry can be seen in the intensity autocorrelations. This causes the reported pulse duration (that corresponding to the experimentally measured FWHM of the intensity autocorrelation) to be overestimated by approximately 10 %.

The VECSEL exhibited a maximum average output power of 8 mW at 1032 nm and this rose, as shown in figure 4.7, to 10 mW at 1048 nm. This average output power was achieved for a constant pump power of 1.1 W and was limited by the onset of thermal rollover for higher pump powers. The increase in power at longer wavelength is attributed to the reduction in insertion loss that occured due to the etalon becoming oriented closer to Brewster's angle. A decrease in the output power of the laser with time was also observed and this is attributed to the laser mode causing localised heating of the SESAM. For this reason the modelocking performance at each new wavelength was characterised after translating the SESAM, so that the mode was incident on a fresh region, and the previous power level therefore restored.

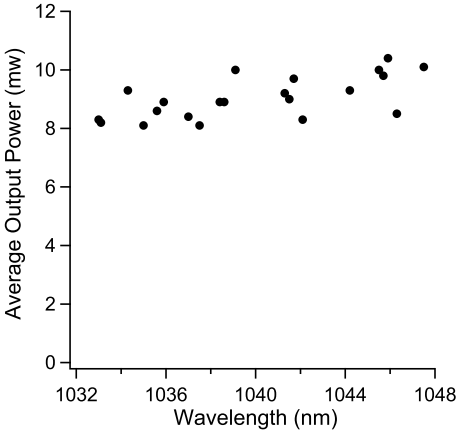

Figure 4.7: Average output power of the laser in mW as it is tuned across the wavelength range

A secondary consequence of orientating the etalon towards Brewster's angle is that the resultant reduction in insertion loss will increase the intracavity power leading to a greater fluence on the SESAM. This in turn will generate a stronger laser mode/SESAM interaction and consequently shorter pulses. This is shown in figure 4.8.

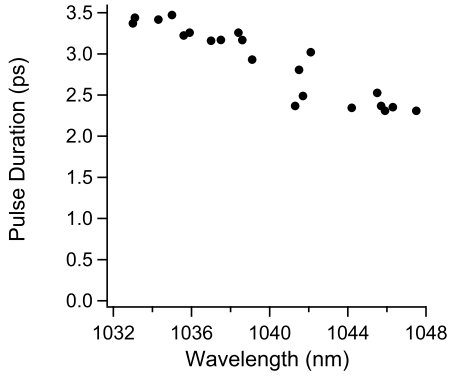

Figure 4.8: Pulse duration in ps emitted by the laser as it is tuned across the wavelength range

4.3.1.3 Performance Summary

This low power, wavelength-tuneable, modelocked VECSEL has demonstrated that it is possible to use an intracavity etalon in order to select the emitted wavelength without disturbing the modelocked operation. The VECSEL displayed a continuous spectral tuning range of 14.5 nm around a central wavelength of 1040.3 nm. The pulse duration was between 2.3 and 3.4 ps and the pulse repetition frequency was 0.95 GHz. The average output power of the VECSEL exceeded 8 mW over the spectral tuning range and consequently the peak power of the VECSEL was between 2.3 and 4.3 W.

The minimum peak power required to generate FWM in PCF is approximately 100 W and therefore this particular VECSEL is not a suitable laser source for a heralded single photon system. The peak power of this VECSEL was limited by the onset of thermal rollover and so, with improved thermal management of the gain, significantly higher peak powers could be achieved.

4.3.2 A High Power, Wavelength-Tuneable, Modelocked VECSEL

In order to produce a VECSEL source with an increased peak power, a thermally managed gain chip, fabricated by NAsP III/V GmbH (Marburg, Germany), was incorporated into the VECSEL design.

As stated previously in section 1.1.4, high power VECSEL operation is in part limited by the temperature of the active region. The GaAs substrate upon which the VECSEL structure is grown acts as a region of high thermal impedance between the active region and the copper heat sink and therefore, by removing this layer, the active region temperature can be reduced. The substrate is removed from the active region by growing the gain chip in reverse: the capping layer is grown on top of the substrate and the wafer is finished with the deposition of the DBR. Solid-liquid inter-diffusion bonding is then used to place a diamond heat spreader in direct thermal contact with the DBR and a chemical etch applied to remove the substrate. A schematic diagram of this process is shown on the following page in figure 4.9.

The processed gain chip used in this second source was epitaxially grown on top of a 500-μm thick GaAs substrate and consists of an InGaP cap layer, a $12\lambda/2$ thick GaAsP active region containing 11 InGaAs quantum wells and a 22 pair AlGaAs/AlAs DBR, in this order. The gain chip was designed to be antiresonant at a wavelength of 1040 nm when operated with an active-region temperature of approximately 100 °C.

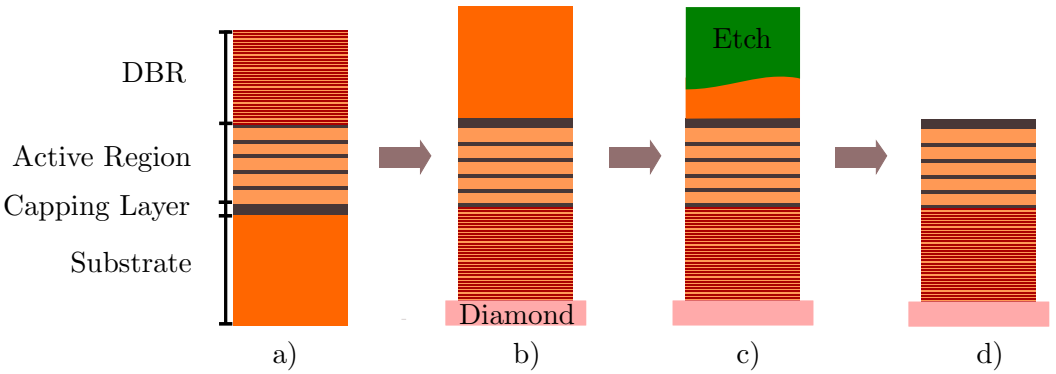

Figure 4.9: The substrate removal process. a) The gain structure is grown in reverse on top of a GaAs substrate b) Solid-liquid inter-diffusion bonding is used to place a diamond heat spreader in direct thermal contact with the DBR c) A chemical etch is used to remove the substrate d) The finished product.

The effectiveness of this thermal management technique can be seen in figure 4.10 which plots the CW output power as a function of pump power for both the processed gain chip used in this second source and the gain chip used in the previous section. The processed gain chip was pump power limited and is able to tolerate at least 30 x more pump power than the unprocessed gain chip. Whilst it is acknowledged that the two gain chips differ by more than just the thermal processing technique these other differences are expected to make relatively little difference to the gain chip performance.

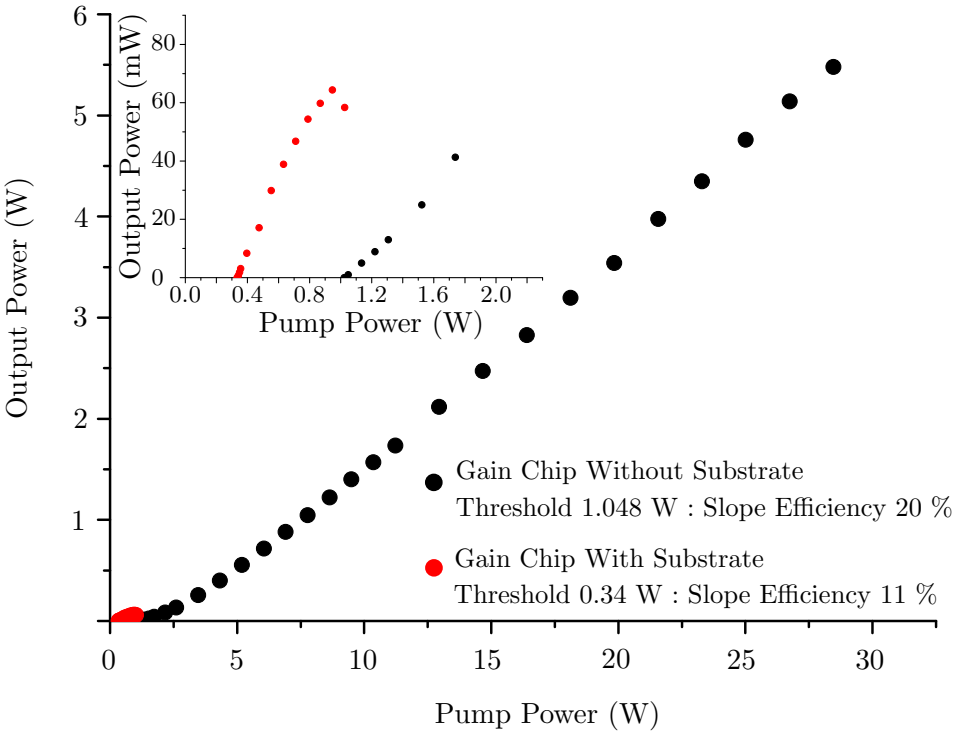

Figure 4.10: The measured CW output power plotted against incident pump power for both the processed gain chip used in the second source and a similar, unprocessed gain chip. The processed gain chip was pump power limited and is able to tolerate at least 30 x more pump power than the unprocessed gain chip.

4.3.2.1 Laser Design

The processed gain chip was bonded to a copper heat-sink maintained at 18 °C using a supply of refridgerated water. A 'V-cavity' geometry was implemented using the same SESAM design as in the previous low-power VECSEL and a 100 mm radius of curvature, 1.45 % transmission output coupler. The etalon, when incorporated into the cavity, was inserted between the gain chip and the output coupler at Brewster's angle.

The gain chip was pumped with a fibre-coupled diode laser delivering 24 W of 808-nm light focused to a 125 μm radius spot. The cavity was 92.5 mm long and the distance between the output coupler and the gain chip was 65 mm. This gave a spot-size area ratio between the gain and the SESAM of approximately 2:1. A schematic diagram of the VECSEL cavity is shown below in figure 4.11.

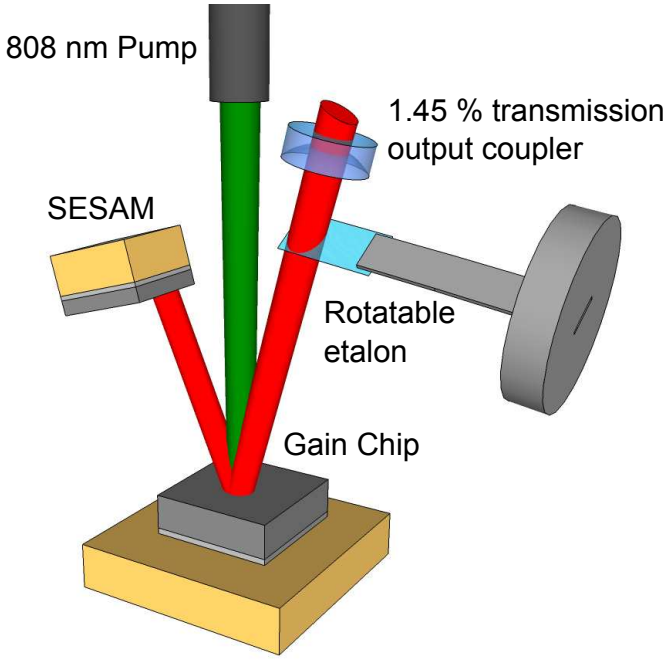

Figure 4.11: Schematic of the laser cavity. Cavity length is 92.5 mm. Distance between the 100 mm RoC, 1.45 % transmission output coupler and gain chip is 65 mm. The pump laser emitted up to 30 W at 808-nm focussed to a 125 μm radius spot. The gain to SESAM spot-size area ratio was $\approx$ 2:1. The fused-silica etalon is uncoated, and 25 μm thick (FSR at normal incidence of 14 nm). The SESAM was cooled to -10°C and the gain chip was maintained at 18 °C.

The diode driver used in this work was limited to 40 W and so the output power of the 40 W pump laser was limited to $\approx$ 30 W. The 125 μm radius pump spot resulted in a pump density that was insufficient to operate the gain chip at an emission wavelength of 1040 nm (it is discussed in the following section why a smaller pump spot could not be used). The SESAM absorption was therefore matched to the gain chip emission by using a Peltier-controlled heatsink to cool the SESAM to -10°C. Nitrogen gas was blown over the face of the SESAM to ensure that the surface was kept free of condensation.

4.3.2.2 Laser Results

Without the etalon in the cavity the VECSEL was able to produce 460 fs pulses around a wavelength of 1039 nm and at a repetition frequency of 1.6 GHz. An average output power of 1.1 W was recorded. The corresponding autocorrelation, optical spectrum and RF spectrum are shown below in fig 4.12 (this data was taken using the equipment described in section 3.5.2).

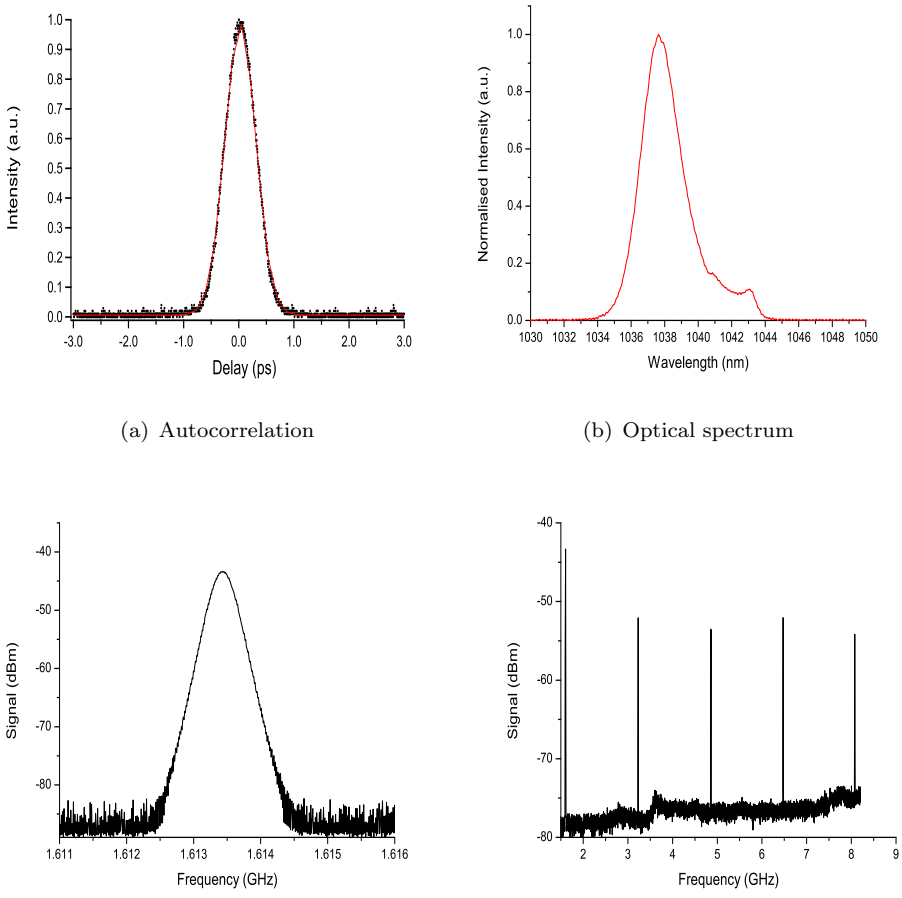

(a) Autocorrelation

(b) Optical spectrum

(c) RF Spectrum: 1^{st} harmonic

(d) RF Spectrum: first 5 harmonicss

Figure 4.12: Characterisation of 460 fs modelocked VECSEL emitting 1.1 W of average power around 1039 nm: 4.12(a) Autocorrelation corresponding to a pulse duration of 460 fs. 4.12(b) Optical spectrum corresponding to a centre wavelength of 1039 nm. 4.12(c) RF spectrum of the 1^{st} harmonic corresponding to a repetition rate of 1.6 GHz. 4.12(d) Truncated RF spectrum showing first 5 harmonics (not equipment limited).

The insertion of the etalon into the laser cavity caused the average power to drop, the wavelength to shorten and the pulse duration to lengthen. The wavelength shortened because the etalon increased the cavity loss and, as the gain bandwidth is broad, this extra loss could be partially avoided by the VECSEL lasing at a shorter wavelength.

The pulse duration most probably increased due to two mechanisms. Firstly the etalon reduced the intracavity power and the consequent reduction in the SESAM fluence would cause a weaker interaction between the laser mode and SESAM. Secondly the etalon will increase the cavity dispersion. Calculating the etalon dispersion profile is possible however, due to time constraints, it would not have been possible to use this result to improve the VECSEL design. Therefore it was decided that the author's time was better spent elsewhere and it is left to the reader to both calculate the dispersion profile of the etalon and to use this information to design a VECSEL that is able to compensate for this additional dispersion.

By rotating the etalon continuous wavelength tuning from 1032 nm to 1026 nm was obtained without disrupting the modelocking. At 1032 nm the laser gave 530 mW of average output power and a pulse duration of 1.3 ps. At 1026 nm the average output power was 400 mW and the pulse duration was 1.7 ps. This performance corresponds to a minimum peak power of 138 W: approximately 30 x the value obtained using an unprocessed gain chip. A summary of the performance is given below in figure 4.13.

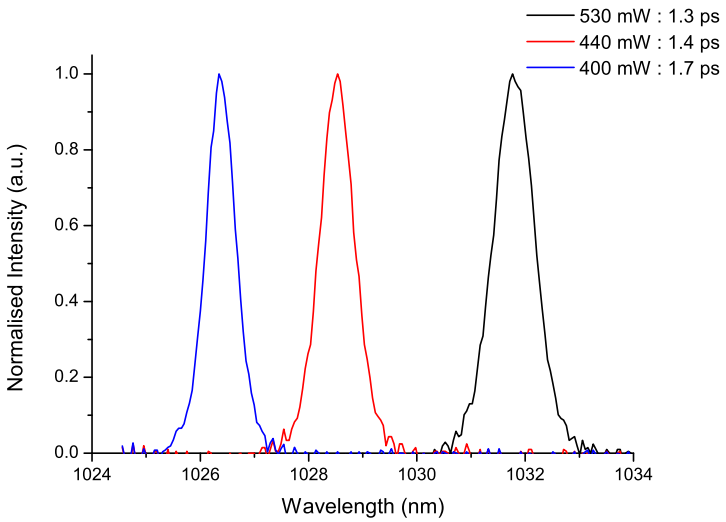

Figure 4.13: Summarised performance of the VECSEL utilising both the processed gain chip and the intracavity etalon. The VECSEL exhibited a modelocked tuning range of 6 nm, a minimum average output power of 400 mW, a maximum pulse length of 1.7 ps and a maximum peak power of 138 W.

As the wavelength is shortened both the decrease in average output power and increase in pulse duration are attributed, as previously discussed in section 4.3.1.2, to the insertion loss of the etalon increasing as it is rotates away from Brewster's angle. The etalon could be used to tune the laser emission to wavelengths shorter than 1026 nm however the laser then exhibited CW operation. This 6 nm tuning range is shorter than the 14 nm tuning range observed in the low power source. A likely explanation for this discrepancy is that for some etalon orientations, the laser emission was forced to a wavelength shorter than the absorption profile of the SESAM.

The VECSEL was able to sustain these operating parameters for 10s of seconds. The laser would then revert to CW operation. Modelocked operation could be recovered by translating the SESAM and letting the laser mode illuminate a fresh spot on the SESAM surface. This suggests that the pulse fluence of ≈ 0.1 mJ/cm^2 was damaging the surface (and most probably the quantum well) of the SESAM structure. To further investigate this idea an optical microscope was used to image the SESAM surface after it had been used in the VECSEL cavity. One such image is shown in figure 4.14: areas of damage, including furrows caused by translating the SESAM, can easily be seen.

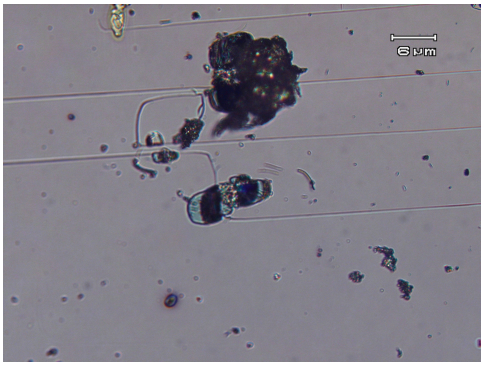

Figure 4.14: An image of the SESAM surface after it had been used in the VECSEL cavity. Damage to the surface can be seen as can furrows leading away to the left and right as a result of translating the SESAM.

To characterise the single photon system the VECSEL must give stable operation over 10s of minutes. It was hoped that this could be achieved by reducing the intracavity power through the inclusion of a higher transmission output coupler and by reducing the amount of pump power used. It was found that for any output coupler greater than 1.45 %, modelocked behaviour was not observed due to the total cavity loss becoming too large for the SESAM to modulate. Reducing the pump power also failed to produce modelocked behaviour as the consequent reduction in pump density was not large enough to drive the gain chip towards the antiresonant, 1040 nm operation that was needed to match the SESAM absorption profile. A decrease in both the pump power and the pump spot size was also tried in the hope that this would maintain the pump density at the required value however, in order to maintain modelocked operation the pump spot to SESAM spot size ratio needed to be conserved, and therefore the SESAM spot size was also reduced meaning that damage to the SESAM surface still occured.

4.3.2.3 Performance Summary

This VECSEL has shown that by using a thermally managed gain chip and an intracavity etalon, a high power, wavelength-tuneable, modelocked VECSEL can be demonstrated. Although this laser would be suitable for the generation of FWM in PCF, due to the stability of the laser being on the order of 10s of seconds, it would not be suitable as a source laser for a single photon system. A SESAM with a higher damage threshold is needed in order to improve the laser stability.

4.3.3 A Stable, High-Power, Wavelength-Tuneable, Modelocked VECSEL

In order to improve the stability of the high power VECSEL a more robust SESAM was needed. A SESAM structure, provided by BATOP optoelectronics (SAM-1064-0.7-1ps), was chosen as it had a protective, antireflection coating applied to the front surface. The quoted damage threshold of this SESAM is 3 mJ/cm^2: well above the pulse fluence of $\approx$ 0.1 mJ/cm^2 observed in the previous laser.

4.3.3.1 Laser Design

A 1.6 GHz, 'V' cavity VECSEL, with dimensions approximate to that as shown in figure 4.11, was assembled using the processed gain chip used in the previous high power VECSEL, the BATOP SESAM and a 1.45 % transmission, 100 mm radius of curvature (ROC) output coupler. The data sheet that accompanied the SESAM stated a damage threshold of 3 mJ/cm^2, a modulation depth of 0.4 %, a non-saturable loss of 0.3 % and a saturation fluence of 130 μJ/cm^2.

The gain structure was maintained at 18 °C and an 808 nm fibre-coupled diode laser was used to pump the gain chip with 23 W of light focused to a 125 μm radius spot. This spot size was chosen to ensure that the fluence on the SESAM was below the quoted damage threshold. This pump density was not high enough to drive the gain chip to 1040 nm operation and so, in order to match the absorption of the SESAM to the emission of the gain chip, the SESAM was cooled to -10°C using a Peltier-cooled heatsink.

4.3.3.2 Laser Results

Modelocked behaviour was not observed until the uncoated 25 μm-thick fused silica etalon was incorporated into the VECSEL cavity. As before the etalon was placed between the output coupler and the gain chip and held close to the Brewster angle of the s-polarised laser mode. By rotating the etalon around Brewster's angle continuous modelocking was observed between 1022.5 nm and 1031.5 nm. Over this spectral range the average output power of the VECSEL always exceeded 1 W and the pulse duration varied between 6 and 20 ps. This performance corresponds to a peak power of between 30 and 137 W and a maximum pulse fluence on the SESAM of $\approx$ 0.25 mJ/cm^2 . The incorporation of the etalon and the use of the BATOP SESAM stabilised the modelocked operation for tens of minutes. The laser performance is summarised in figure 4.15.

Despite the pulse duration being longer in this laser than the previous VECSEL source, due to the increase in the average output power the peak power was comparable at certain etalon orientations. Subsequent exploration of the cavity alignment showed that, by rotating the etalon to select the desired wavelength and then optimising the laser cavity alignment at this wavelength, it was possible to obtain this comparable peak power for any wavelength within the tuning range. The need to reoptimise the cavity geometry was probably due to the laser mode striking dirt on the surface of the etalon.

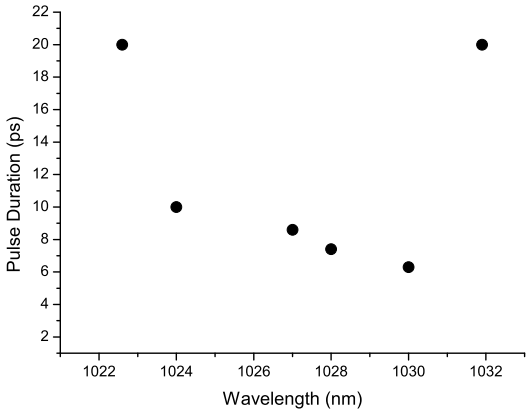

(a)

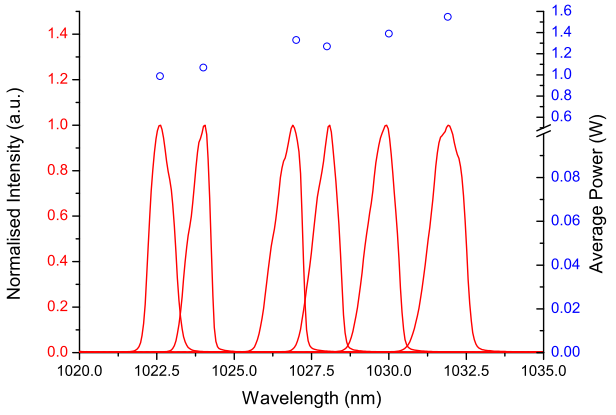

(b)

Figure 4.15: Summarised performance of the VECSEL using the processed gain chip, the BATOP SESAM and the intracavity etalon. The VECSEL exhibited a modelocked tuning range of 10 nm, a maximum pulse length of 20 ps (a) and a minimum average output power of 1 W (b). The maximum peak power obtained was 137 W.

4.3.3.3 Performance Summary

A stable, high-power, wavelength-tuneable, modelocked VECSEL has been demonstrated. The VECSEL displayed a continuous spectral tuning range of 9 nm around a central wavelength of 1027 nm. The pulse duration was between 6 and 20 ps and the pulse repetition frequency was 1.6 GHz. Over the tuning range the average output power of the VECSEL exceeded 1 W and consequently the peak power of the VECSEL was at least 38 W. By optimising the cavity geometry the peak power could be set as high as 137 W. The incorporation of the etalon and the use of the BATOP SESAM stabilised the modelocked operation to 10s of minutes. This laser is suitable for the generation of

FWM in PCF and is stable enough to be used as a source laser for a laboratory-based single photon system.

4.4 Photon-Pair Generation In Photonic Crystal Fibre With A 1.5 GHz Modelocked VECSEL

The stable, high power, wavelength-tuneable, modelocked VECSEL described in the previous section was transported to the University of Bath. This section details how the VECSEL was incorporated into the single photon system operated by Dr Peter Mosley and Mr Jamie Francis-Jones and used to generate coincident photon pairs. It should be noted that each detector used in this work cannot differentiate between one photon and multiple photons that arrive simultaneously. Consequently it was possible to record the coincident pair generation rate and not the single pair generation rate. The work presented in this section is published in Optics Communications [106].

4.4.1 The Implementation Of The VECSEL Source

The VECSEL source was integrated into the single photon system as shown below in figure 4.16.

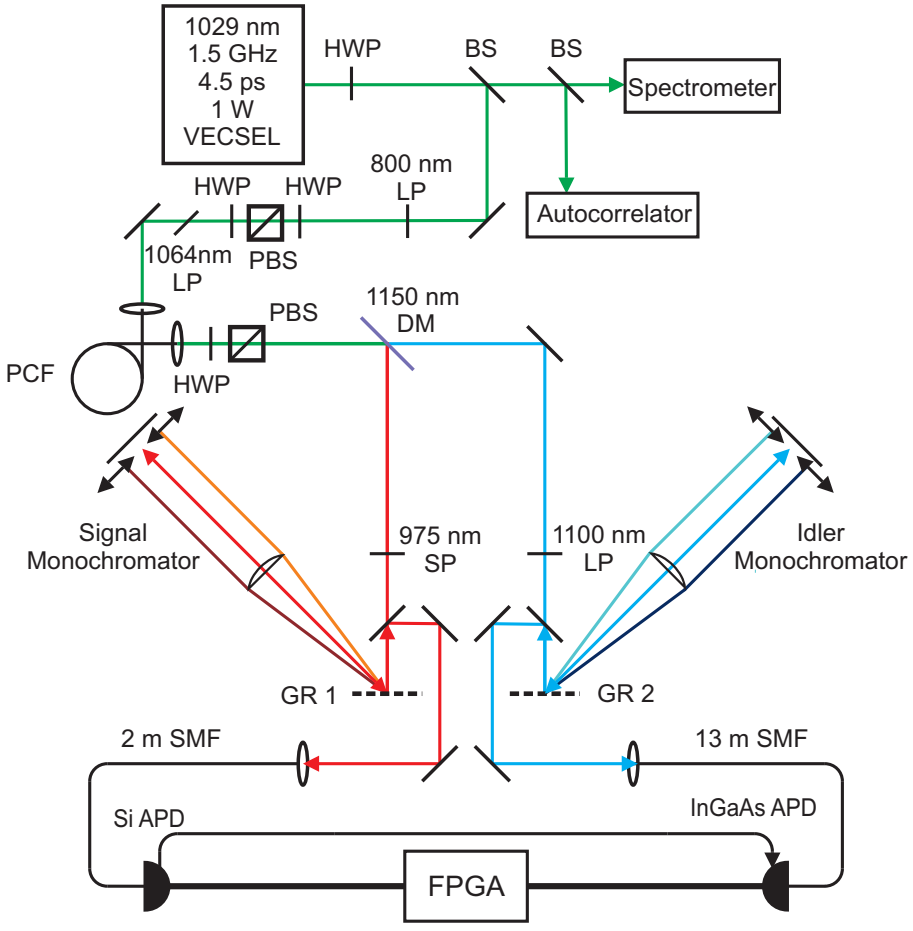

Figure 4.16: The VECSEL-pumped photon-pair source

The choice of PCF was informed by both the VECSEL performance benchmarks obtained in Southampton and the wish to generate a coincident photon pair with a signal photon around 800 nm (the wavelength at which the silicon detector is most efficient) and a corresponding idler photon around 1550 nm (within the low-loss window of conventional telecoms fibre). The PCF comprises a solid silica glass core surrounded by a cladding region formed by a triangular array of air holes in a silica glass matrix. The hole spacing (pitch) was approximately 3 μm and the ratio of hole diameter to pitch was approximately 0.4. The PCF characteristics based on these parameters were calculated by Jamie and are shown below in figure 4.17. The zero-dispersion wavelength of the PCF was measured using white-light interferometry to be 1058 nm. The PCF was fabricated in Bath by the stack-and-draw technique.

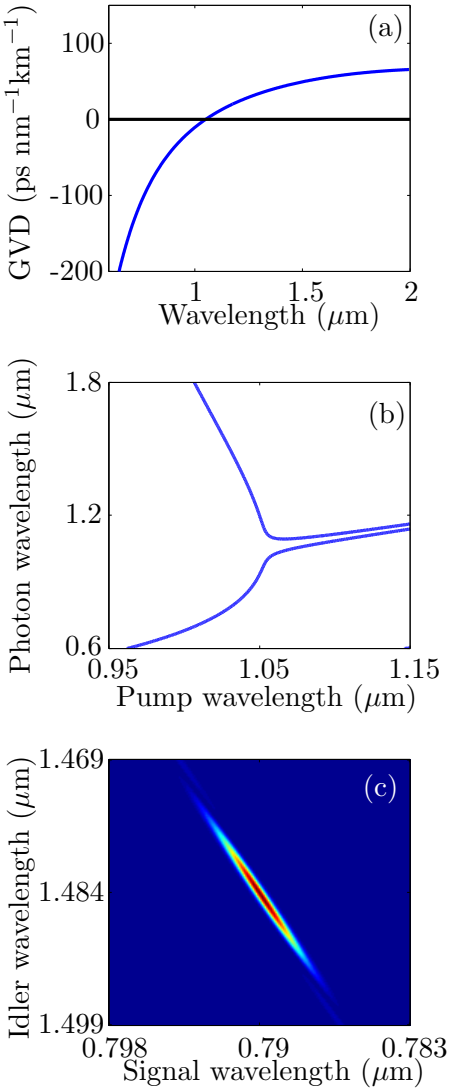

Figure 4.17: The expected characteristics of the PCF: (a) Modelled PCF group-velocity dispersion (GVD) and (b) corresponding FWM phasematching. (c) shows a calculated probability density plot for the resulting two-photon state when pumped at 1029 nm.

The wavelength of the VECSEL emission was set to 1029 nm by rotating the intracavity etalon. The cavity alignment was then optimised to give 4.5 ps pulses at a repetition frequency of 1.5 GHz. The average output power was 1 W corresponding to a peak power of 140 W. An autocorrelation, optical spectrum and RF measurement is shown below in figure 4.18.

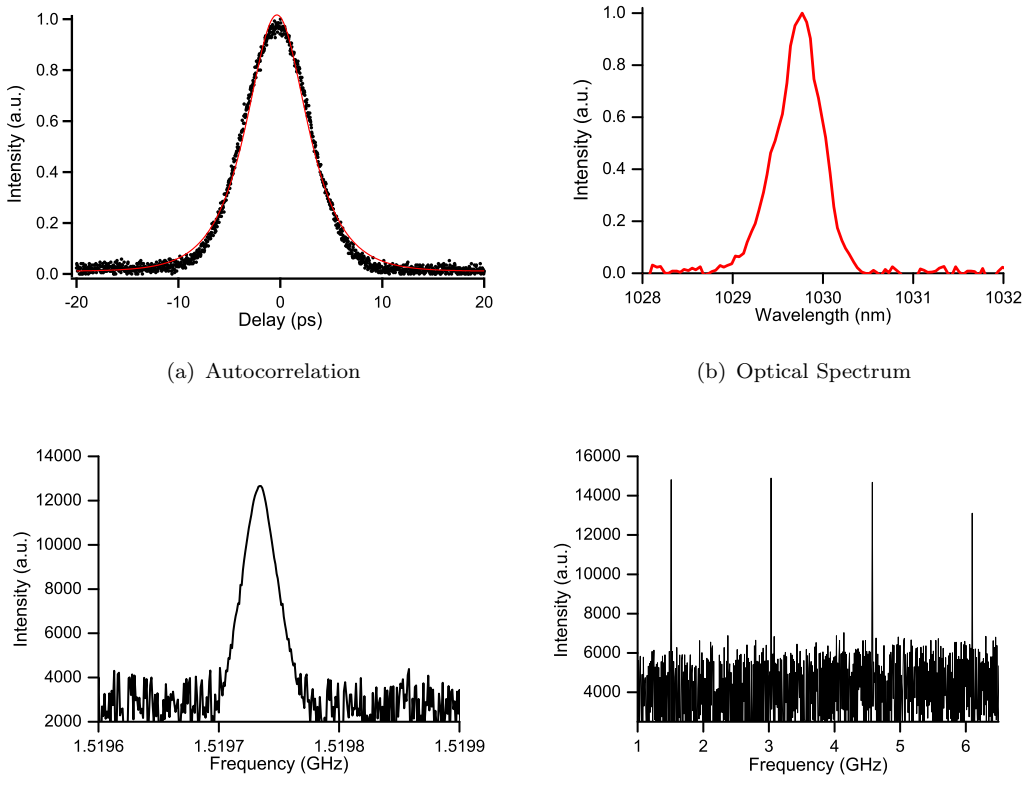

(a) Autocorrelation

(b) Optical Spectrum

(c) RF Spectrum (1^{st} Harmonic)

(d) RF Spectrum (1^{st} – 4^{th} harmonics)

Figure 4.18: Characterisation of 4.5 ps modelocked VECSEL source emitting 1 W of average power at 1030 nm: 4.18(a) Autocorrelation corresponding to a pulse duration of 4.5 ps. 4.18(b) Optical spectrum corresponding to a centre wavelength of 1029.8 nm. 4.18(c) RF spectrum of the 1^{st} harmonic corresponding to a repetition rate of 1.5 GHz. 4.18(d) RF spectrum of the first four harmonics.

The beam from the VECSEL was passed through two long-wave-pass filters in order to remove any residual 808 nm light originating from the pump diode. A pellicle was used to pick off approximately 8 % of the beam and this was guided to a spectrometer and an autocorrelator in order to provide constant monitoring of the VECSEL output. The remaining 92 % was directed through two half-wave plates separated by a polarising beamsplitter as this gave control over both the power and polarisation of the beam prior to it being coupled into the PCF through an aspheric lens. A coupling efficiency of approximately 70 % was achieved.

The PCF emission was collimated using a second aspheric lens and then passed through a half-wave plate and polariser in order to select only the light that was co-polarised with the pump. The signal and idler beams were obtained by spectrally splitting the PCF emission using a dichroic mirror. Any residual 1029 nm pump was removed from both arms with additional interference filters. Both signal and idler beams were passed through home-built grating monochromators in order to both reduce the background noise further and to give a measurement of the signal and idler wavelengths.

Finally the beams were guided into the single photon detectors through conventional single-mode fibre: the 800 nm photons were routed through 2 m of SM800 to a free-running silicon avalanche photodiode (Perkin-Elmer SPCM) and the 1550 nm photons were routed through 13 m of SMF-28 connected to an InGaAs detector (idQuantique id201). The difference in fibre length ensured that the 800 nm photon could be detected and a consequent gating signal sent from the Si APD to the InGaAs detector before the 1550 nm photon arrived. The count rates from both detectors were monitored by a field-programmable gate array (FPGA) coincidence counting unit built by Mr Jamie Francis-Jones.

The gate width of the InGaAs APD was set to its minimum value of 2.5 ns. It can be seen from figure 4.19 that the resulting effective coincidence window is less than 2 ns, or approximately three times the laser repetition period. Therefore for each detection event at the Si APD there were three possible pump pulses within which any corresponding photons counted by the InGaAs APD could have originated. Nevertheless, the high-contrast coincidence signal at 7.5 ns and constant background at all other delays is strong evidence of a correlated generation process from a single pump pulse as one would expect from FWM. Within the limitations of the detectors available, there was no possibility of reducing the coincidence window to a single pump pulse.

4.4.2 Results

Figure 4.19 shows a typical plot of the InGaAs detector count rate as a function of the internal delay between the arrival of the trigger pulse and the detection window opening. With the delay set to 7.5 ns, the detection window of the InGaAs detector encompassed the arrival times of photons generated by the same pump pulse as those that triggered the Si detector. The height of this peak shows the number of coincidence counts per second between the signal and idler arms. Away from this peak is a constant background level of accidental coincidence events arising from uncorrelated generation and detection processes. By using a 6 m length of PCF and an average pump power of 50 mW, the central wavelengths and bandwidths of the monochromators were adjusted to maximise the CAR. This resulted in a measured central wavelength of the signal and idler of 780 nm and 1515 nm respectively and a CAR value of 13.

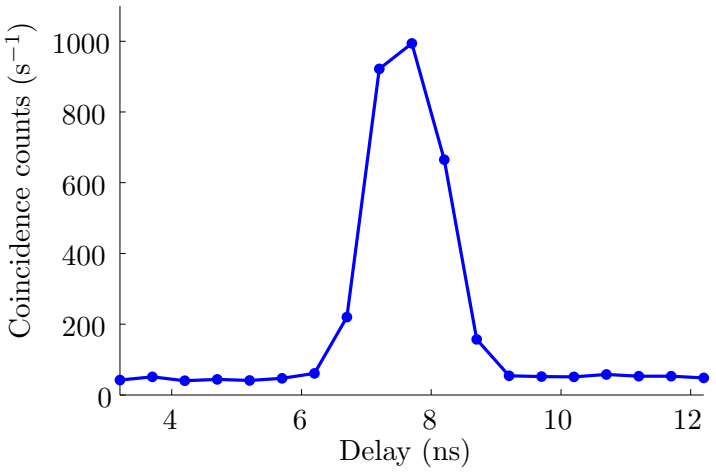

Figure 4.19: A typical plot of the the InGaAs APD count rate (equal to the coincidence count rate) against internal detector delay for a 6 m length of PCF and an average pump power of 50 mW.

In order to further optimise the CAR the PCF was cut back in stages from an initial length of 6 m. The results for three different power levels are shown in figure 4.20. It can be seen that the CAR never dropped below 7 and rose rapidly as the PCF length was reduced below 1 m indicating a significant improvement in system performance. The highest measured value of the CAR was over 80, using 50 mW of pump power and a PCF length of 210 mm. The absolute coincidence count under these conditions was approximately 1000 pairs/s. This fibre length corresponded to approximately half the calculated walk-off length between the signal and idler and the 4.5 ps pump pulses (450 mm and 340 mm respectively).

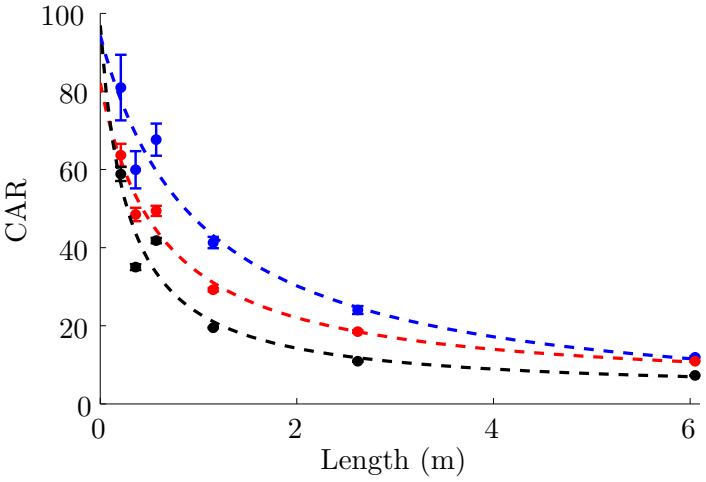

Figure 4.20: Measured coincidence-to-accidental ratio as a function of PCF length for average pump powers of 50 mW (blue),100 mW (red), and 150mW (black). Dotted lines are fits proportional to 1/L

The absolute count rates were limited by the high level of loss following the PCF, particularly in the idler arm. Nevertheless the highest recorded coincidence count rate was 9600 pairs/s with a CAR of over 20 from 150 mW of pump power in a fibre length of 1.15 m. This work has shown that a wavelength-tuneable, modelocked VECSEL can be used as a laser source in a FWM, single photon system.

4.4.3 Future Work

The work reported in this chapter has shown that a wavelength-tuneable, modelocked VECSEL can be used as a laser source in a FWM, single photon system. It was not possible to further improve or characterise the system due to financial, time and equipment constraints. It is hoped that this work will inspire future investigations to be made into the suitability of the VECSEL as a heralded single-photon source pump laser.

A measurement of the single pair to multiple pair emission ratio would be of particular interest as this would further advance the argument that a VECSEL has a significant advantage per mW average power in terms of the ratio of multiple-to-single pair emission events when compared to a typical 80 MHz, Ti:Sapphire pump laser. This measurement would be undertaken by placing a 50/50 beam splitter into the signal arm and then, by directing the resultant third beam into a third detector, a single pair emission could be distinguished from a multiple pair emission by registering a two-detector or three-detector coincidence respectively.

It is also hoped that by moving to an all-fibre spliced system the loss that results from the freespace transmission of photons between the PCF and the single-mode collection fibres will be reduced. This should lead to an increase in the absolute count rates. This work is currently being undertaken by Mr Jamie Francis-Jones.

4.5 Chapter Conclusions

This chapter has reported the development of a VECSEL source capable of generating coincident photon pairs through four wave mixing in photonic crystal fibre. FWM in PCF is an attractive method for producing photon pairs for quantum-information applications, as it combines the simplicity of nonlinear wave-mixing techniques with guided-wave architecture to allow high-efficiency pair generation. Single photon systems traditionally use either expensive, complex and large Ti:Sapphire oscillators or fixed wavelength, neodymium based lasers laser sources which in turn place stringent manufacturing tolerances on the PCF.

A wavelength-tuneable, modelocked VECSEL is highly suited for the generation of heralded single photons. It is compact, inexpensive and mechanically simple. It exhibits

excellent beam quality resulting in a high coupling efficiency between the VECSEL and the PCF. The short carrier lifetime, low gain saturation fluence and relatively short cavity length result in a pulse frequency that is typically on the order of GHz leading to a greater number of qubits generated per second for a given level of acceptable error. The wavelength selectivity is beneficial as it allows changes in the PCF dispersion profile that result from small fabrication errors to be compensated for.

It has been shown that the wavelength of a modelocked VECSEL can be selected by incorporating an intracavity etalon in to the external cavity. This low power, wavelength-tuneable, modelocked VECSEL exhibited a tuning range of 14.5 nm around a central wavelength of 1040 nm. The pulse duration was between 2.3 and 3.4 ps and the pulse repetition frequency was 0.95 GHz. The average output power of the VECSEL exceeded 8 mW over the spectral tuning range and consequently the peak power of the VECSEL was between 2.3 and 4.3 W.

A second VECSEL using a thermally managed gain chip displayed a continuous spectral tuning range of 6 nm around a central wavelength of 1029 nm. The pulse duration was between 1.7 and 1.3 ps and the pulse repetition frequency was 1.6 GHz. The average output power of the VECSEL exceeded 400 mW over the tuning range and consequently the peak power of the VECSEL was at least 138 W.

A stable, high power, wavelength-tuneable, modelocked VECSEL was demonstrated that used a commerically grown SESAM. This VECSEL displayed a continuous spectral tuning range of 9 nm around a central wavelength of 1027 nm. The pulse duration was between 6 and 20 ps and the pulse repetition frequency was 1.6 GHz. Over the tuning range the average output power of the VECSEL exceeded 1 W and consequently the peak power of the VECSEL was at least 38 W. By optimising the cavity geometry the peak power could be set as high as 137 W.

This stable, high power, wavelength-tuneable, modelocked VECSEL was implemented as the source laser in the single photon system operated by Dr Peter Mosley and Mr Jamie Franics-Jones at the University of Bath. The highest measured value of the coincidence to accidental ratio was over 80, using 50 mW of pump power and a PCF length of 210 mm, and at an absolute coincidence count rate of almost 1000 pairs/s. This result was published under the title of 'Photon-Pair Generation In Photonic Crystal Fibre With A 1.5 GHz Modelocked VECSEL' in Optics Communications [106].

It is hoped that this work will inspire future investigations to be made into the suitability of the VECSEL as a heralded single-photon source pump laser.

Chapter 5

Conclusions

5.1 Major Results Presented In This Work

Cryogenic cooling has been used to achieve efficient high-power operation of ytterbium-doped solid-state lasers [69, 70, 71]. The VECSEL's semiconductor gain region is also highly temperature sensitive and, by reducing the active region temperature, improvements can be made to the device performance: enhanced gain per carrier, reduced carrier density at the point of quantum well transparency and a delayed onset of Auger-recombination induced thermal rollover are all observed when the active region temperature is lowered [24]. Prior to this research the coldest temperature at which a VECSEL gain chip had been operated was 248 K. These results show that cryogenic temperatures significantly improve VECSEL performance and begin a new direction in VECSEL research.

This thesis began by theoretically quantifying the benefits of operating a VECSEL gain chip at cryogenic temperatures. A model based upon Fermi's Golden Rule was used to quantify the effect of quantum well temperature on the percentage gain per quantum well and the carrier density required to reach quantum well transparency. This model calculated that, by cooling a gain chip from 300 to 80 K, a 140 % increase in percentage gain for a carrier density of 0.5 x 10^{18} cm^{-3} and a 70 % reduction in the carrier density required for quantum well transparency should be observed. A steady-state thermal FEA model was then presetned that calculated the effect of heat-sink temperature and pump power on the active region temperature. By using this model it was calculated that a gain chip cooled from 300 to 80 K would be able to tolerate a 6.2-fold increase in pump power prior to the onset of thermal rollover (the short-comings of this model are discussed in the following section). A VECSEL utilising a cryogenically cooled gain chip was therefore expected to exhibit a reduced laser threshold, an increased slope efficiency and a tolerance to greater pump powers when compared to a VECSEL operating at room temperature.

In order to both verify the accuracy of the FEA model and to allow the active region temperature of the VECSEL gain chip to be obtained when sealed inside a cryostat, a method for remotely obtaining the active region temperature of a pumped VECSEL gain chip was presented. The method used a fixed wavelength VECSEL to probe the reflectivity profile of a DBR as it shifted in wavelength due to changes in the temperature of the gain chip. The method was tested at room temperature and for an incident pump power of up to 1 W. Under these conditions the temperature of the active region was determind to within an accuracy of ±2 K. By comparing the results of this method to the the FEA model it was possible to show that, for these operating conditions, the FEA model is accurate to within 18 K (6 %) of the experimentally measured value. The method shall be applied to a cryogenically cooled VECSEL chip in the following chapter.

Chapter 2 concluded by reporting a preliminary attempt to demonstrate a cryogenically cooled VECSEL. A helium flow-cryostat was used to cool a VECSEL gain chip from 293 to 20 K. This resulted in a 4.5-fold increase in the pump power required to achieve lasing, an 80 % decrease in maximum output power and a delayed onset of thermal rollover. This last observation suggested that a higher carrier density, and therefore an increase in the maximum gain available, could be supported at cryogenic temperatures. This statement was further supported by observing that the VECSEL was unable to lase at 293 K due to the loss imposed by the intracavity cryostat window however, when cooled 20 K, the VECSEL overcame this additional loss and lased. The observed increase in gain per quantum well at cryogenic temperatures is predicted by the model set out in section 2.2.1 however the observed increase in threshold carrier density for 20 K operation is not. This disagreement was most likely due to the performance of the cryogenically cooled VECSEL being dominated by the cryostat window acting as an unwanted, high-loss, intracavity element.

Chapter 3 began by detailing the construction of a cryostat with a vacuum space large enough to house an entire VECSEL cavity. The cryostat used a liquid nitrogen cold-finger design and was built in the Mechanical Workshop by Mr Damon Grimsey. I am indebted to his skill and hard work. Four investigations into cryogenic VECSEL operation were then presented.

An investigation into the effect of heat-sink temperature and incident pump power on the active region temperature was conducted. For a cold-finger temperature of 80 K, and a maximum incident pump power of 2.5 W, the measured rise in active region temperature, extracted with respect to incident pump power, was found to be 22.6 x 10^{-3}± 0.2 x 10^{-3} K/mW.

An investigation into the effect of temperature on the incident pump power required to reach laser-threshold was conducted. This investigation found that by reducing the temperature of the cryostat cold-finger from 293 to 83 K, the amount of incident pump power required to reach laser-threshold reduced by 53 % ± 10 %.

An investigation into the effect of temperature on the amount of incident pump power tolerated prior to the onset of thermal rollover was conducted. This investigation showed that by reducing the temperature of the cryostat cold-finger from 293 to 83 K the VECSEL gain chip was able to tolerate a 4-fold increase in incident pump power prior to the VECSEL switching off. This increase in pump power corresponded to an increase in output power from 143 mW to 1540 mW: an increase of more than an order of magnitude.

Finally a modelocked VECSEL utilising a cryogenically cooled gain chip was reported. Modelocked behaviour was observed for a cold-finger temperature of 143 K and an incident pump power of 3.6 W. The temperature was constrained by the need to align the emission wavelength of the gain chip to the absorption profile of the SESAM. Under these conditions the VECSEL emitted 4.7 ps pulses at a pulse repetition rate of 0.966 GHz. The $TEM_{0,0}$, diffraction limited beam had a wavelength around 1006 nm and an average power of 22.4 mW. The emitted pulses therefore had a peak power of 4.6 W and were approximately 6-times the transform limit for a $sech^2$ pulse

This thesis concluded by reporting on the development and implementation of a VECSEL source capable of generating coincidental photon pairs through four wave mixing in photonic crystal fibre. A wavelength-tuneable, modelocked VECSEL is highly suited to this application as it is compact, inexpensive and mechanically simple. It also exhibits excellent beam quality resulting in a high coupling efficiency between the VECSEL and the PCF. The short carrier lifetime, low gain saturation fluence and relatively short cavity length result in a pulse frequency that is typically on the order of GHz leading to a greater number of qubits generated per second for a given level of acceptable error. The wavelength selectivity is beneficial as it allows changes in the PCF dispersion profile that result from small fabrication errors to be compensated for.

A stable, high power, wavelength-tuneable, modelocked VECSEL was demonstrated that, when optimised using an intracavity etalon, emitted 4.5 ps pulses at a repetition frequency of 1.5 GHz, a wavelength of 1029 nm and an average output power of 1 W. This corresponded to a peak power of 140 W. The high power was obtained by using a VECSEL gain chip that had been chemically processed in order to remove the high thermal impedence GaAs substrate. This gain chip was paired with a commercially grown SESAM structure provided by BATOP optoelectronics (SAM-1064-0.7-1ps).

This VECSEL was then implemented as the source laser in the single photon system operated by Dr Peter Mosley and Mr Jamie Franics-Jones at the University of Bath. The highest measured value of the coincidence to accidental ratio was over 80, using 50 mW of pump power and a PCF length of 210 mm, and at an absolute coincidence count rate of almost 1000 pairs/s. This result was published under the title of 'Photon-Pair Generation In Photonic Crystal Fibre With A 1.5 GHz Modelocked VECSEL' in Optics Communications [106].

Power scaling of the VECSEL links the two areas of research presented in this thesis. Cryogenic cooling was tested as a route to high power VECSEL operation and this approach resulted in an order of magnitude increase in the output power. The heralded single photon work implemented a chemically etched VECSEL gain chip in order to increase the VECSEL output power and this technique was shown, in a CW configuration, to increase the VECSEL output power by a factor of 50. Due to the inconvenience of working with a cryostat the 'processed chip' approach may appear to be the better thermal management method. Both techniques are however complimentary and, through pre-stressing the gain chip to ensure that it is unaffected by differential contraction, it is conceivable that the two approaches could be used together to both further improve the thermal mangement and further increase the output power of the VECSEL.

It is the author's hope that these first results will inspire further research and development in the field of cryogenically cooled VECSELs. It is also hoped that this work will inspire future investigations to be made into the suitability of the VECSEL as a heralded single-photon source pump laser.

5.2 Future Research

5.2.1 Cryogenic VECSEL Operation

The work presented in this thesis is the first successful demonstration of a VECSEL using a cryonically cooled gain chip. For this reason there is a wealth of further research that could be conducted.

Firstly a FEA thermal-stress model of the gain chip could be developed. The investigations reported in this thesis made best use of pre-existing gain chip designs and therefore it is expected that the performance of a cryogenically cooled VECSEL could be further extended by using a gain chip that is specifically designed for cryogenic operation. For instance a gain chip could be designed that is stressed by an appropriate amount in the opposite direction at room temperature and this would ensure that the net-stress placed on the gain chip would be 0 when operated at cryogenic temperatures and pumped with intense optical fields. A FEA thermal-stress model of the gain chip would therefore help to inform the design of this kind of gain chip.

Secondly the FEA model used in this work assumed that the active region heat-load is generated by the quantum defect alone and heating through non-radiative recombination is neglected. This is inaccurate and so it is suggested that an updated FEA thermal model is constructed by building on the results stated in [24]. To incorporate this microscopic, many-body modelling into the FEA model would be a complex process however, once done, it would give a more accurate insight into the gain chip's tolerance of pump power and therefore be useful as a tool to inform future gain chip design.

Thirdly an investigation should be undertaken into the thermal properties of the bond between the gain chip and the cold finger. All the gain chips used in this work were bonded to the cold finger using a silver paint that had unknown thermal properties when operated within the cryogenic regime. By studying the effect of cryogenic temperatures on both silver paint and other bonding materials (indium for example) a bond between the gain chip and cold-figner with lower thermal impedence may be obtained. This would help transport heat out of the gain chip more efficiently leading to lower active region temperatures and the use of higher pump powers.

Finally a measurement of the gain profile as a function of cold-finger temperature would both give insight into the temperature dependent carrier dynamics of the active region and help to inform the design of future gain chips. For example if cryogenic temperatures are seen to narrow the gain spectrum this would help in the design of cryogenic modelocked lasers. This measurement would involve illuminating the gain chip with a wavelength tuneable, modelocked laser and measuring the single pass gain as a function of probe wavelength and gain temperature.

Whilst the application of cryogenic cooling to solid-state lasers has resulted in significant improvements in solid-state laser performance (section 2.1) this method of thermal regulation has, due to its relative complexity, been largely confined to the laboratory environment. This chapter has shown that VECSEL performance can also be greatly improved through cryogenic cooling and, with the on-going development of micro cryogenic coolers [75], this could make compact, cryogenically cooled VECSELs a very real and attractive prospect.

5.2.2 The VECSEL As A Pump Source For Heralded Single-Photon Generation

The implementation of the modelocked VECSEL as a source laser for a single-photon system demonstrates that the modelocked VECSEL is now a mature technology that can be relied upon as a component in a larger experiment. Due to financial, time and equipment constraints it was only possible to measure the number of coincidental photon pairs being generated and not the number of coincidental single pairs being generated. A measurement of the single pair to multiple pair emission ratio is therefore the next experiment to be undertaken using this developed source. This measurement would be undertaken by placing a 50/50 beam splitter into the signal arm and then, by directing the resultant third beam into a third detector, a single pair emission could be distinguished from a multiple pair emission by registering a two-detector or three-detector coincidence respectively.

This experiment would be of particular interest as it would further advance the argument that a VECSEL has a significant advantage, per mW average power, in terms of the ratio of multiple-to-single pair emission events when compared to a typical 80-MHz, Ti:Sapphire pump laser.

Appendix A

Derivation of the phase difference caused when light passes through an etalon at some angle

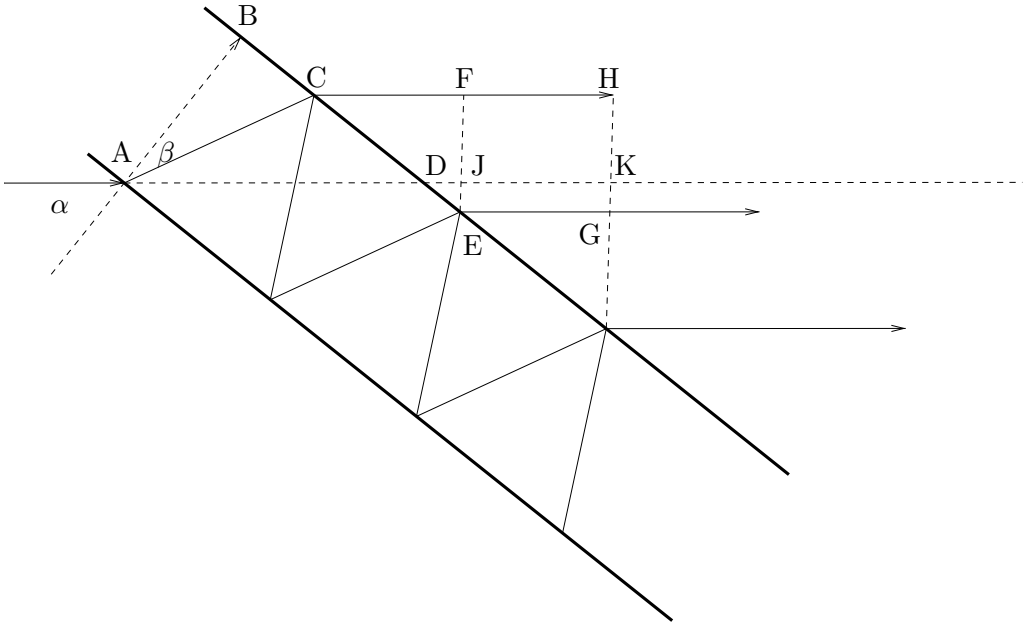

$$\begin{aligned}
\phi_F &= \phi_C + kn_0(CF) \\
&= \phi_C + kn_0 \sin\alpha(CE) \\
&= \phi_C + kn_0 \sin\alpha(2D\tan\beta) \\
&= \phi_A + \frac{kDn_1}{\cos\beta} + 2kDn_0 \sin\alpha \tan\beta
\end{aligned}$$

$$\begin{aligned}
\phi_J &= \phi_D + kn_0(DJ) \\
&= \phi_D + kn_0 \sin\alpha(DE) \\
&= \phi_D + kn_0 \sin\alpha(BE - BD) \\
&= \phi_D + kn_0 \sin\alpha(3D\tan\beta - D\tan\alpha) \\
&= \phi_A + \frac{kn_0 D}{\cos\alpha} + kDn_0 \sin\alpha(3\tan\beta - \tan\alpha)
\end{aligned}$$

$$\begin{aligned}
\phi_F - \phi_J &= \frac{kDn_1}{\cos\beta} + 2kDn_0 \sin\alpha\tan\beta - \frac{kn_0 D}{\cos\alpha} - kDn_0 \sin\alpha(3\tan\beta - \tan\alpha) \\
&= \frac{kDn_1}{\cos\beta} - kDn_0 \sin\alpha\tan\beta - \frac{kn_0 D}{\cos\alpha} + kDn_0 \sin\alpha\tan\alpha
\end{aligned}$$

From Snell's Law $n_0 \sin\alpha = n_1 \sin\beta$ leading to

$$\begin{aligned}
\phi_F - \phi_J &= \frac{kDn_1}{\cos\beta} - \frac{kDn_1 \sin^2\beta}{\cos\beta} - \frac{kn_0 D}{\cos\alpha} + \frac{kDn_0 \sin^2\alpha}{\cos\alpha} \\
&= kDn_1 \cos\beta - kDn_0 \cos\alpha
\end{aligned}$$

$$\begin{aligned}
\phi_E - \phi_J &= \phi_A + \frac{3kDn_1}{\cos\beta} - \phi_A - \frac{kDn_0}{\cos\alpha} - kDn_0 \sin\alpha(3\tan\beta - \tan\alpha) \\
&= \frac{3kDn_1}{\cos\beta} - \frac{kn_0 D}{\cos\alpha} - 3kDn_0 \sin\alpha\tan\beta + kDn_0 \sin\alpha\tan\alpha \\
&= \frac{3kDn_1}{\cos\beta} - \frac{kn_0 D}{\cos\alpha} - \frac{3kDn_1 \sin^2\beta}{\cos\beta} + \frac{kDn_0 \sin^2\alpha}{\cos\alpha} \\
&= 3kDn_1 \cos\beta - kDn_0 \cos\alpha \\
&= \phi_F - \phi_J - 2kDn_1 \cos\beta
\end{aligned}$$

[107]

Appendix B

Selected Publications

Oliver J Morris, Robert JA Francis-Jones, Keith G Wilcox, Anne C Tropper, and Peter J Mosley. Photon-pair generation in photonic crystal fibre with a 1.5 GHz modelocked VECSEL. *Optics Communications*, 327:39–44, 2014

Oliver J Morris, Keith G Wilcox, CR Head, Andrew P Turnbull, Ian Farrer, Harvey E Beere, David A Ritchie, and Anne C Tropper. Effects of cryogenic temperatures on the performance of CW VECSELs. In *SPIE LASE*, pages 86060L–86060L. International Society for Optics and Photonics, 2013

Oliver J Morris, Keith G Wilcox, C Robin Head, Andrew P Turnbull, Peter J Mosley, Adrian H Quarterman, Hani J Kbashi, Ian Farrer, Harvey E Beere, David A Ritchie, et al. A wavelength tunable 2-ps pulse VECSEL. In *SPIE LASE*, pages 824212–824212. International Society for Optics and Photonics, 2012

C Robin Head, Keith G Wilcox, Andrew P Turnbull, Oliver J Morris, Edward A Shaw, and Anne C Tropper. Saturated gain spectrum of VECSELs determined by transient measurement of lasing onset. *Optics express*, 22(6):6919–6924, 2014

Keith G Wilcox, Hani J Kbashi, Adrian H Quarterman, Oliver J Morris, Vasilis Apostolopoulos, Mohamed Henini, and Anne C Tropper. Wetting-layer-pumped continuous-wave surface-emitting quantum-dot laser. *Photonics Technology Letters, IEEE*, 24(1):37–39, 2012

Andrew P Turnbull, Keith G Wilcox, C Robin Head, Oliver J Morris, Ian Farrer, David A Ritchie, and Anne C Tropper. Generation of 200 fs pulses with a short microcavity VECSEL. In *SPIE LASE*, pages 86060O–86060O. International Society for Optics and Photonics, 2013

References

[1] Tso Yee Fan and Robert L Byer. Diode laser-pumped solid-state lasers. *Quantum Electronics, IEEE Journal of*, 24(6):895–912, 1988.

[2] Guenter Huber, Christian Kränkel, and Klaus Petermann. Solid-state lasers: status and future [invited]. *JOSA B*, 27(11):B93–B105, 2010.

[3] Stuart J McNaught, Hiroshi Komine, S Benjamin Weiss, Randy Simpson, Adam M Johnson, Jason Machan, Charles P Asman, Mark Weber, Gina C Jones, Marcy M Valley, et al. 100 kW coherently combined slab MOPAs. In *Conference on Lasers and Electro-Optics*, page CThA1. Optical Society of America, 2009.

[4] Adolf Giesen and Jochen Speiser. Fifteen years of work on thin-disk lasers: results and scaling laws. *Selected Topics in Quantum Electronics, IEEE Journal of*, 13(3):598–609, 2007.

[5] Jens Limpert, Fabian Roser, Sandro Klingebiel, Thomas Schreiber, Christian Wirth, Thomas Peschel, Ramona Eberhardt, and Andreas Tunnermann. The rising power of fiber lasers and amplifiers. *Selected Topics in Quantum Electronics, IEEE Journal of*, 13(3):537–545, 2007.

[6] M Kuznetsov, F Hakimi, R Sprague, and A Mooradian. High-power (> 0.5-W CW) diode-pumped vertical-external-cavity surface-emitting semiconductor lasers with circular TEM_{00} beams. *Photonics Technology Letters, IEEE*, 9(8):1063–1065, 1997.

[7] Oleg G Okhotnikov. *Semiconductor Disk Lasers: Physics and Technology*. John Wiley & Sons, 2010.

[8] AC Tropper and S Hoogland. Extended cavity surface-emitting semiconductor lasers. *Progress in Quantum Electronics*, 30(1):1–43, 2006.

[9] C. Brecher, N. Pyschny, S. Haag, and T. Mueller. Automated assembly of vecsel components. *Vertical External Cavity Surface Emitting Lasers (VECSELs) III*, Feb 2013.

[10] Coherent obis laser range. http://www.coherent.com/products/?1884/OBIS-Lasers. Accessed: 2014-03-24.

[11] H Lindberg, S Illek, I Pietzonka, M Furitsch, A Plößl, S Haupt, M Kühnelt, R Schulz, U Steegmüller, T Höfer, et al. Recent advances in VECSELs for laser projection applications. In *SPIE LASE*, pages 79190D–79190D. International Society for Optics and Photonics, 2011.

[12] M Rahim, F Felder, M Fill, and H Zogg. Optically pumped 5 μm IV-VI VECSEL with Al-heat spreader. *Optics letters*, 33(24):3010–3012, 2008.

[13] J-M Hopkins, N Hempler, B Rösener, N Schulz, M Rattunde, C Manz, K Köhler, J Wagner, and David Burns. High-power, AlGaIn AsSb semiconductor disk laser at 2.0 μm. *Optics letters*, 33(2):201–203, 2008.

[14] Hans Lindberg, Martin Strassner, E Gerster, and Anders Larsson. 0.8 W optically pumped vertical external cavity surface emitting laser operating CW at 1550 nm. *Electronics Letters*, 40(10):601–602, 2004.

[15] Hans Lindberg, Martin Strassner, and Anders Larsson. Improved spectral properties of an optically pumped semiconductor disk laser using a thin diamond heat spreader as an intracavity filter. *Photonics Technology Letters, IEEE*, 17(7):1363–1365, 2005.

[16] V-M Korpijärvi, M Guina, J Puustinen, P Tuomisto, J Rautiainen, A Härkönen, A Tukiainen, O Okhotnikov, and M Pessa. MBE grown GaInNAs-based multi-Watt disk lasers. *Journal of Crystal Growth*, 311(7):1868–1871, 2009.

[17] Li Fan, Chris Hessenius, Mahmoud Fallahi, Jörg Hader, Hongbo Li, Jerome V Moloney, Wolfgang Stolz, Stephan W Koch, James T Murray, and Robert Bedford. Highly strained InGaAs/GaAs multiwatt vertical-external-cavity surface-emitting laser emitting around 1170 nm. *Applied Physics Letters*, 91(13):1114, 2007.

[18] Jennifer E Hastie, Stephane Calvez, Martin D Dawson, Tomi Leinonen, Antti Laakso, Jari Lyytikäinen, and Markus Pessa. High power CW red vecsel with linearly polarized $TEM_{0,0}$ output beam. *Optics Express*, 13(1):77–81, 2005.

[19] Li Fan, Mahmoud Fallahi, Aramais R Zakharian, Jorg Hader, Jerome V Moloney, Robert Bedford, James T Murray, Wolfgang Stolz, and Stephan W Koch. Extended tunability in a two-chip VECSEL. *Photonics Technology Letters, IEEE*, 19(8):544–546, 2007.

[20] Jonna Paajaste, Soile Suomalainen, Riku Koskinen, Antti Härkönen, Mircea Guina, and Markus Pessa. High-power and broadly tunable GaSb-based optically pumped VECSELs emitting near 2μm. *Journal of Crystal Growth*, 311(7):1917–1919, 2009.

[21] Antti Harkonen. Antimonide disk lasers achieve multiwatt power and a wide tuning range. *SPIE Newsroom*, 2009.

[22] Jennifer E Hastie, Lynne G Morton, Alan J Kemp, Martin D Dawson, Andrey B Krysa, and John S Roberts. Tunable ultraviolet output from an intracavity frequency-doubled red vertical-external-cavity surface-emitting laser. *Applied physics letters*, 89(6):061114–061114, 2006.

[23] JunHo Lee, SangMoon Lee, Taek Kim, and YongJo Park. 7 W high-efficiency continuous-wave green light generation by intracavity frequency doubling of an end-pumped vertical external-cavity surface emitting semiconductor laser. *Applied physics letters*, 89(24):241107–241107, 2006.

[24] Jörg Hader, Tsuei-Lian Wang, J Michael Yarborough, Colm A Dineen, Yushi Kaneda, Jerome V Moloney, Bernardette Kunert, Wolfgang Stolz, and Stephan W Koch. VECSEL optimization using microscopic many-body physics. *Selected Topics in Quantum Electronics, IEEE Journal of*, 17(6):1753–1762, 2011.

[25] S Lutgen, T Albrecht, P Brick, W Reill, J Luft, and W Spath. 8-W high-efficiency continuous-wave semiconductor disk laser at 1000 nm. *Applied Physics Letters*, 82(21):3620–3622, 2003.

[26] J Hader, T-L Wang, JV Moloney, B Heinen, M Koch, SW Koch, B Kunert, and W Stolz. On the measurement of the thermal impedance in vertical-external-cavity surface-emitting lasers. *Journal of Applied Physics*, 113(15):153102, 2013.

[27] William J Alford, Thomas D Raymond, and Andrew A Allerman. High power and good beam quality at 980 nm from a vertical external-cavity surface-emitting laser. *JOSA B*, 19(4):663–666, 2002.

[28] ZL Liau. Semiconductor wafer bonding via liquid capillarity. *Applied Physics Letters*, 77(5):651–653, 2000.

[29] J-M Hopkins, SA Smith, CW Jeon, HD Sun, D Burns, S Calvez, MD Dawson, T Jouhti, and M Pessa. 0.6 w cw GaInNAs vertical external-cavity surface emitting laser operating at 1.32 μm. *Electronics Letters*, 40(1):30–31, 2004.

[30] K-S Kim, JR Yoo, SH Cho, SM Lee, SJ Lim, J-Y Kim, JH Lee, T Kim, and YJ Park. 1060 nm vertical-external-cavity surface-emitting lasers with an optical-to-optical efficiency of 44% at room temperature. *Applied physics letters*, 88(9):091107–091107, 2006.

[31] A. Harkonen, S. Suomalainen, E. Saarinen, L. Orsila, R. Koskinen, O. Okhotnikov, S. Calvez, and M. Dawson. 4 W single-transverse mode VECSEL utilising intracavity diamond heat spreader. *Electronics Letters*, 42(12):693, 2006.

[32] Emmi Kantola, Tomi Leinonen, Sanna Ranta, Miki Tavast, and Mircea Guina. High-efficiency 20 W yellow VECSEL. *Optics Express*, 22(6):6372–6380, 2014.

[33] Jennifer E Hastie, J-M Hopkins, Stephane Calvez, Chan Wook Jeon, David Burns, Richard Abram, Erling Riis, Allister I Ferguson, and Martin D Dawson. 0.5-W single transverse-mode operation of an 850-nm diode-pumped surface-emitting semiconductor laser. *Photonics Technology Letters, IEEE*, 15(7):894–896, 2003.

[34] B Heinen, T-L Wang, M Sparenberg, A Weber, B Kunert, J Hader, SW Koch, JV Moloney, M Koch, and W Stolz. 106 W continuous-wave output power from vertical-external-cavity surface-emitting laser. *Electronics letters*, 48(9):516–517, 2012.

[35] B Rudin, A Rutz, M Hoffmann, DJHC Maas, A-R Bellancourt, E Gini, T Südmeyer, and U Keller. Highly efficient optically pumped vertical-emitting semiconductor laser with more than 20 W average output power in a fundamental transverse mode. *Optics letters*, 33(22):2719–2721, 2008.

[36] Alexej Chernikov, Jens Herrmann, Martin Koch, Bernardette Kunert, Wolfgang Stolz, Sangam Chatterjee, Stephan W Koch, Tsuei-Lian Wang, Yushi Kaneda, J Michael Yarborough, et al. Heat management in high-power vertical-external-cavity surface-emitting lasers. *Selected Topics in Quantum Electronics, IEEE Journal of*, 17(6):1772–1778, 2011.

[37] Ursula Keller and Anne C Tropper. Passively modelocked surface-emitting semiconductor lasers. *Physics Reports*, 429(2):67–120, 2006.

[38] DJHC Maas, AR Bellancourt, M Hoffmann, B Rudin, Y Barbarin, M Golling, T Südmeyer, and U Keller. Growth parameter optimization for fast quantum dot SESAMs. *Optics express*, 16(23):18646–18656, 2008.

[39] Christian A Zaugg, Zhipei Sun, Daniel Popa, Silvia Milana, Tero Kulmala, Ravi S Sundaram, Valentin J Wittwer, Mario Mangold, Oliver D Sieber, Matthias Golling, et al. Wavelength tunable graphene modelocked VECSEL. In *CLEO: Science and Innovations*, pages CW1G–4. Optical Society of America, 2013.

[40] S Hoogland, S Dhanjal, AC Tropper, JS Roberts, R Haring, R Paschotta, F Morier-Genoud, and U Keller. Passively mode-locked diode-pumped surface-emitting semiconductor laser. *Photonics Technology Letters, IEEE*, 12(9):1135–1137, 2000.

[41] M Scheller, T-L Wang, B Kunert, W Stolz, SW Koch, and JV Moloney. Passively modelocked VECSEL emitting 682 fs pulses with 5.1 W of average output power. *Electronics letters*, 48(10):588–589, 2012.

[42] Alexandre Laurain, Maik Scheller, Tsuei-Lian Wang, Jorg Hader, Jerome V Moloney, Bernd Heinen, Bernardette Kunert, and Wolfgang Stolz. Recent advances in power scaling of high-power optically-pumped semiconductor lasers for ultrashort pulse generation and continuous wave single frequency operation. In

SPIE Defense, Security, and Sensing, pages 873303–873303. International Society for Optics and Photonics, 2013.

[43] Adrian H Quarterman, Keith G Wilcox, Vasilis Apostolopoulos, Zakaria Mihoubi, Stephen P Elsmere, Ian Farrer, David A Ritchie, and Anne Tropper. A passively mode-locked external-cavity semiconductor laser emitting 60-fs pulses. *Nature Photonics*, 3(12):729–731, 2009.

[44] P Klopp, U Griebner, M Zorn, and M Weyers. Pulse repetition rate up to 92 GHz or pulse duration shorter than 110 fs from a mode-locked semiconductor disk laser. *Applied Physics Letters*, 98(7):071103, 2011.

[45] M Guina, A Härkönen, J Paajaste, J-P Alanko, S Suomalainen, C Grebing, and G Steinmeyer. Passively mode-locked GaSb-based VECSELs emitting sub-400-fs pulses at 2 μm. In *SPIE LASE*, pages 824204–824204. International Society for Optics and Photonics, 2012.

[46] Sanna Ranta, Antti Härkönen, Tomi Leinonen, Lasse Orsila, Jari Lyytikäinen, Günter Steinmeyer, and Mircea Guina. Mode-locked vecsel emitting 5 ps pulses at 675 nm. *Optics letters*, 38(13):2289–2291, 2013.

[47] Christian A Zaugg, Alexander Klenner, Oliver D Sieber, Matthias Golling, Bauke W Tilma, and Ursula Keller. Sub-100 MHz passively modelocked VECSEL. In *CLEO: Science and Innovations*, pages CW1G–6. Optical Society of America, 2013.

[48] Keith G Wilcox, Adrian H Quarterman, Vasilis Apostolopoulos, Harvey E Beere, Ian Farrer, David A Ritchie, and Anne C Tropper. 175 GHz, 400-fs-pulse harmonically mode-locked surface emitting semiconductor laser. *Optics express*, 20(7):7040–7045, 2012.

[49] DJHC Maas, A-R Bellancourt, B Rudin, M Golling, HJ Unold, T Südmeyer, and U Keller. Vertical integration of ultrafast semiconductor lasers. *Applied Physics B*, 88(4):493–497, 2007.

[50] B Rudin, VJ Wittwer, DJHC Maas, M Hoffmann, OD Sieber, Y Barbarin, M Golling, T Südmeyer, and U Keller. High-power MIXSEL: an integrated ultrafast semiconductor laser with 6.4 W average power. *Optics express*, 18(26):27582–27588, 2010.

[51] Mario Mangold, Valentin J Wittwer, Christian A Zaugg, Sandro M Link, Matthias Golling, Bauke W Tilma, and Ursula Keller. Femtosecond pulses from a mode-locked integrated external-cavity surface emitting laser (MIXSEL). *Optics express*, 21(21):24904–24911, 2013.

[52] Peter J Mosley, Jeff S Lundeen, Brian J Smith, Piotr Wasylczyk, Alfred B URen, Christine Silberhorn, and Ian A Walmsley. Heralded generation of ultrafast single photons in pure quantum states. *Physical Review Letters*, 100(13):133601, 2008.

[53] Alexander Ling, Jun Chen, Jingyun Fan, and Alan Migdall. Mode expansion and bragg filtering for a high-fidelity fiber-based photon-pair source. *Optics express*, 17(23):21302–21312, 2009.

[54] Andreas Eckstein, Andreas Christ, Peter J Mosley, and Christine Silberhorn. Highly efficient single-pass source of pulsed single-mode twin beams of light. *Physical review letters*, 106(1):013603, 2011.

[55] HARUHISA Soda, YOSHIHIRO Motegi, and KENICHI Iga. GaInAsP/InP surface emitting injection lasers with short cavity length. *Quantum Electronics, IEEE Journal of*, 19(6):1035–1041, 1983.

[56] Fumio Koyama, Susumu KINOSHITA, and Iga Kenichi. Room temperature CW operation of GaAs vertical cavity surface emitting laser. *IEICE TRANSACTIONS (1976-1990)*, 71(11):1089–1090, 1988.

[57] FH Peters, MG Peters, DB Young, JW Scott, BJ Thibeault, SW Corzine, and LA Coldren. High-power vertical-cavity surface-emitting lasers. *Electronics Letters*, 29(2):200–201, 1993.

[58] RS Geels and LA Coldren. Low threshold, high power, vertical-cavity surface-emitting lasers. *Electronics Letters*, 27(21):1984–1985, 1991.

[59] JD Walker, DM Kuchta, and JS Smith. Vertical-cavity surface-emitting laser diodes fabricated by phase-locked epitaxy. *Applied physics letters*, 59(17):2079–2081, 1991.

[60] Alexander J Maclean, Alan J Kemp, John-Mark Hopkins, Jennifer E Hastie, Stephanie Giet, Stephane Calvez, Martin D Dawson, David Burns, Jun-Youn Kim, Ki-Sung Kim, et al. An analysis of power scaling and thermal management in a 1060nm VECSEL with a diamond heatspreader. In *Conference on Lasers and Electro-Optics*, page JWB21. Optical Society of America, 2006.

[61] Growth and characterization of compound semiconductors for optoelectronics. http://www.cat.ernet.in/newsletter/news/lasernews/ln992/ln992a01.html. Accessed: 2014-03-24.

[62] RD Dupuis and PD Dapkus. Room-temperature operation of distributed-bragg-confinement $Ga_{1-x}Al_xAs$-GaAs lasers grown by metalorganic chemical vapor deposition. *Applied Physics Letters*, 33(1):68–69, 2008.

[63] A. Garnache. Master's thesis, Institut National Polytechnique de Grenoble, 1996.

[64] KG Wilcox, AH Quarterman, HE Beere, DA Ritchie, and AC Tropper. Variable repetition frequency femtosecond-pulse surface emitting semiconductor laser. *Applied Physics Letters*, 99(13):131107, 2011.

[65] Oliver D Sieber, Valentin J Wittwer, Mario Mangold, Martin Hoffmann, Matthias Golling, Thomas Südmeyer, and Ursula Keller. Femtosecond VECSEL with tunable multi-gigahertz repetition rate. *Optics express*, 19(23):23538–23543, 2011.

[66] U Keller, DAB Miller, GD Boyd, TH Chiu, JF Ferguson, and MT Asom. Solid-state low-loss intracavity saturable absorber for Nd:YLF lasers: an antiresonant semiconductor Fabry-Perot saturable absorber. *Optics letters*, 17(7):505–507, 1992.

[67] Ursula Keller, Kurt J Weingarten, Franz X Kartner, Daniel Kopf, Bernd Braun, Isabella D Jung, Regula Fluck, Clements Honninger, Nicolai Matuschek, and J Aus der Au. Semiconductor saturable absorber mirrors (SESAM's) for femtosecond to nanosecond pulse generation in solid-state lasers. *Selected Topics in Quantum Electronics, IEEE Journal of*, 2(3):435–453, 1996.

[68] R Paschotta, R Häring, A Garnache, S Hoogland, AC Tropper, and U Keller. Soliton-like pulse-shaping mechanism in passively mode-locked surface-emitting semiconductor lasers. *Applied Physics B*, 75(4-5):445–451, 2002.

[69] David C Brown. The promise of cryogenic solid-state lasers. *Selected Topics in Quantum Electronics, IEEE Journal of*, 11(3):587–599, 2005.

[70] Tso Yee Fan, Daniel J Ripin, Roshan L Aggarwal, Juan R Ochoa, Bien Chann, Michael Tilleman, and Joshua Spitzberg. Cryogenic Yb 3+-doped solid-state lasers. *Selected Topics in Quantum Electronics, IEEE Journal of*, 13(3):448–459, 2007.

[71] David C Brown. Ultrahigh-average-power diode-pumped Nd:YAG and Yb:YAG lasers. *Quantum Electronics, IEEE Journal of*, 33(5):861–873, 1997.

[72] Glen A Slack and DW Oliver. Thermal conductivity of garnets and phonon scattering by rare-earth ions. *Physical Review B*, 4(2):592, 1971.

[73] Philipp H Klein and William J Croft. Thermal conductivity, diffusivity, and expansion of Y_2O_3, $Y_3Al_5O_{12}$, and LaF_3 in the range 77-300 k. *Journal of Applied Physics*, 38(4):1603–1607, 2004.

[74] Rosalind Wynne, John L Daneu, and Tso Yee Fan. Thermal coefficients of the expansion and refractive index in YAG. *Applied optics*, 38(15):3282–3284, 1999.

[75] PPPM Lerou, HJM Ter Brake, JF Burger, HJ Holland, and H Rogalla. Characterization of micromachined cryogenic coolers. *Journal of Micromechanics and Microengineering*, 17(10):1956, 2007.

[76] Larry A Coldren, Scott W Corzine, and Milan L Mashanovitch. *Diode lasers and photonic integrated circuits*, volume 218. John Wiley & Sons, 2012.

[77] Alan J Kemp, Gareth J Valentine, J-M Hopkins, Jennifer E Hastie, Scott A Smith, Stephane Calvez, Martin D Dawson, and David Burns. Thermal management in vertical-external-cavity surface-emitting lasers: Finite-element analysis of a heat-spreader approach. *Quantum Electronics, IEEE Journal of*, 41(2):148–155, 2005.

[78] MD Sturge. Optical absorption of gallium arsenide between 0.6 and 2.75 ev. *Physical Review*, 127(3):768, 1962.

[79] RO Carlson, GA Slack, and SJ Silverman. Thermal conductivity of GaAs and $GaAs_{1-x}P_x$ laser semiconductors. *Journal of Applied Physics*, 36(2):505–507, 1965.

[80] Brian K Ridley. *Electrons and phonons in semiconductor multilayers*, volume 5. Cambridge University Press, 2009.

[81] Gang Chen. Phonon heat conduction in nanostructures. *International journal of thermal sciences*, 39(4):471–480, 2000.

[82] Gavin W Morley, Petra Lueders, M Hamed Mohammady, Setrak J Balian, Gabriel Aeppli, Christopher WM Kay, Wayne M Witzel, Gunnar Jeschke, and Tania S Monteiro. Quantum control of hybrid nuclear–electronic qubits. *Nature materials*, 12(2):103–107, 2013.

[83] James D Siverns, Seb Weidt, Kim Lake, Bjoern Lekitsch, Marcus D Hughes, and Winfried K Hensinger. Optimization of two-dimensional ion trap arrays for quantum simulation. *New Journal of Physics*, 14(8):085009, 2012.

[84] Brahim Lounis and Michel Orrit. Single-photon sources. *Reports on Progress in Physics*, 68(5):1129, 2005.

[85] Alex Clark, Bryn Bell, Jérémie Fulconis, Matthäus M Halder, Ben Cemlyn, Olivier Alibart, Chunle Xiong, William J Wadsworth, and John G Rarity. Intrinsically narrowband pair photon generation in microstructured fibres. *New Journal of Physics*, 13(6):065009, 2011.

[86] Masato Tanida, Ryo Okamoto, and Shigeki Takeuchi. Highly indistinguishable heralded single-photon sources using parametric down conversion. *Optics express*, 20(14):15275–15285, 2012.

[87] Rui-Bo Jin, Ryosuke Shimizu, Kentaro Wakui, Hugo Benichi, and Masahide Sasaki. Widely tunable single photon source with high purity at telecom wavelength. *Optics express*, 21(9):10659–10666, 2013.

[88] Andreas Christ and Christine Silberhorn. Limits on the deterministic creation of pure single-photon states using parametric down-conversion. *Physical Review A*, 85(2):023829, 2012.

[89] Robert W Boyd. *Nonlinear optics*. Academic press, 2003.

[90] Govind P Agrawal. *Nonlinear fiber optics*. Springer, 2000.

[91] Kunimasa Saitoh and Masanori Koshiba. Empirical relations for simple design of photonic crystal fibers. *Optics express*, 13(1):267–274, 2005.

[92] CK Hong and Leonard Mandel. Experimental realization of a localized one-photon state. *Physical Review Letters*, 56:58–60, 1986.

[93] Jamie Francis-Jones. Towards an all-fibre multiplexed source of single photons. MPhil to PhD report, September 2013.

[94] Jonathan C Knight. Photonic crystal fibres. *Nature*, 424(6950):847–851, 2003.

[95] Offir Cohen, Jeff S Lundeen, Brian J Smith, Graciana Puentes, Peter J Mosley, and Ian A Walmsley. Tailored photon-pair generation in optical fibers. *Physical review letters*, 102(12):123603, 2009.

[96] Matthaeus Halder, Jeremie Fulconis, Ben Cemlyn, Alex Clark, Chunle Xiong, William J Wadsworth, and John G Rarity. Nonclassical 2-photon interference with separate intrinsically narrowband fibre sources. *Optics express*, 17(6):4670–4676, 2009.

[97] Matthew A Broome, Marcelo P Almeida, Alessandro Fedrizzi, and Andrew G White. Reducing multi-photon rates in pulsed down-conversion by temporal multiplexing. *Optics express*, 19(23):22698–22708, 2011.

[98] Alex R McMillan, J Fulconis, M Halder, C Xiong, JG Rarity, and William J Wadsworth. Narrowband high-fidelity all-fibre source of heralded single photons at 1570 nm. *Optics express*, 17(8):6156–6165, 2009.

[99] A Aschwanden, D Lorenser, HJ Unold, R Paschotta, E Gini, and U Keller. 2.1-W picosecond passively mode-locked external-cavity semiconductor laser. *Optics letters*, 30(3):272–274, 2005.

[100] K Garay-Palmett, HJ McGuinness, Offir Cohen, JS Lundeen, R Rangel-Rojo, AB U'ren, MG Raymer, CJ McKinstrie, S Radic, and IA Walmsley. Photon pair-state preparation with tailored spectral properties by spontaneous four-wave mixing in photonic-crystal fiber. *Optics express*, 15(22):14870–14886, 2007.

[101] WP Grice, AB Uren, and IA Walmsley. Eliminating frequency and space-time correlations in multiphoton states. *Physical Review A*, 64(6):063815, 2001.

[102] Peter J Mosley, Jeff S Lundeen, Brian J Smith, and Ian A Walmsley. Conditional preparation of single photons using parametric downconversion: a recipe for purity. *New Journal of Physics*, 10(9):093011, 2008.

[103] Christoph Söller, Offir Cohen, Brian J Smith, Ian A Walmsley, and Christine Silberhorn. High-performance single-photon generation with commercial-grade optical fiber. *Physical Review A*, 83(3):031806, 2011.

[104] Liang Cui, Xiaoying Li, and Ningbo Zhao. Minimizing the frequency correlation of photon pairs in photonic crystal fibers. *New Journal of Physics*, 14(12):123001, 2012.

[105] Masahiro Yabuno, Ryosuke Shimizu, Yasuyoshi Mitsumori, Hideo Kosaka, and Keiichi Edamatsu. Four-photon quantum interferometry at a telecom wavelength. *Physical Review A*, 86(1):010302, 2012.

[106] Oliver J Morris, Robert JA Francis-Jones, Keith G Wilcox, Anne C Tropper, and Peter J Mosley. Photon-pair generation in photonic crystal fibre with a 1.5 GHz modelocked VECSEL. *Optics Communications*, 327:39–44, 2014.

[107] Geoff Daniell. The phase difference occuring when an infinite plane wave passes through an etalon at some angle. April 2011.

[108] Oliver J Morris, Keith G Wilcox, CR Head, Andrew P Turnbull, Ian Farrer, Harvey E Beere, David A Ritchie, and Anne C Tropper. Effects of cryogenic temperatures on the performance of CW VECSELs. In *SPIE LASE*, pages 86060L–86060L. International Society for Optics and Photonics, 2013.

[109] Oliver J Morris, Keith G Wilcox, C Robin Head, Andrew P Turnbull, Peter J Mosley, Adrian H Quarterman, Hani J Kbashi, Ian Farrer, Harvey E Beere, David A Ritchie, et al. A wavelength tunable 2-ps pulse VECSEL. In *SPIE LASE*, pages 824212–824212. International Society for Optics and Photonics, 2012.

[110] C Robin Head, Keith G Wilcox, Andrew P Turnbull, Oliver J Morris, Edward A Shaw, and Anne C Tropper. Saturated gain spectrum of VECSELs determined by transient measurement of lasing onset. *Optics express*, 22(6):6919–6924, 2014.

[111] Keith G Wilcox, Hani J Kbashi, Adrian H Quarterman, Oliver J Morris, Vasilis Apostolopoulos, Mohamed Henini, and Anne C Tropper. Wetting-layer-pumped continuous-wave surface-emitting quantum-dot laser. *Photonics Technology Letters, IEEE*, 24(1):37–39, 2012.

[112] Andrew P Turnbull, Keith G Wilcox, C Robin Head, Oliver J Morris, Ian Farrer, David A Ritchie, and Anne C Tropper. Generation of 200 fs pulses with a short microcavity VECSEL. In *SPIE LASE*, pages 86060O–86060O. International Society for Optics and Photonics, 2013.